First-principles density-functional theory calculations of thermomagnetic properties

by

Seyed Emad Rezaei

A Dissertation submitted to the School of Engineering and
Applied Science University of Virginia
In Partial Fulfillment of the Requirements for the Degree of
Doctor of Philosophy in Electrical Engineering

University of Virginia, Electrical Engineering

December 2022

Declaration

This is to certify that the thesis work entitled *"First-principles density-functional theory calculations of thermomagnetic properties"* was done by *Seyed Emad Rezaei* in the Department of *Electrical Engineering*, University of Virginia. Neither this dissertation nor any part of this work were submitted elsewhere for the award of a degree.

Approval

This is to certify that the thesis work submitted by *Seyed Emad Rezaei* entitled *"First-principles density-functional theory calculations of thermomagnetic properties"* was approved by the the committee for the partial fulfillment of the requirements for the degree of PhD in the Department of *Electronic Engineering*, University of Virginia in December 2022.

Committee Members

1. _____
   Mona Zebarjadi, Advisor

2. _____
   Keivan Esfarjani, Co-advisor

3. _____
   Jon Ihlefeld, Chair

4. _____
   Nikhil Shukla

5. _____
   Despina Louca

6. _____
   Prasanna V Balachandran

To my family

Acknowledgments

I have spent more than four years at the University of Virginia and it is nearly impossible to state how much grateful I am for the mentors, collaborators, family, and friends who assisted me in this dissertation. Their support played a key role in my success and I would not have been able to earn my PhD without their helps.

First, I would like to thank my advisor, Prof. Mona Zebarjadi, and my co-advisor, Prof. Keivan Esfarjani. The first time we met in person dates back to the recruiting week of the spring 2018. After our meeting, I ensured that I would like to do my PhD under their supervision. Not only have their guidance and mentorship enhanced my skills as a researcher, but I have also been greatly motivated by them. They have been with me throughout the PhD trip and let me make errors to learn. Their outstanding background in the area of solid state devices, charge transport, and computational science aided my research and gave me the opportunity to improve my knowledge. More eminently, I appreciate them for being preeminently professional and patient that taught me in order to solve a problem I first have to understand it, then scrutinize it, and finally find the solution. I am more than happy to do my PhD in this field and under their supervision and I am absolutely thankful to have had them as my advisors.

I need to to express my gratitude to my PhD committee, Prof. Jon Ihlefeld, Prof. Despina Louca, Prof. Nikhil Shukla, and Prof. Prasanna Balachandran, for their continuous guidance and advice. The insight provided by them aided me preparing my dissertation, in addition to craft my research plans for the future.

I enjoyed studying at the University of Virginia and specifically at the electrical engineering department. I have lots of joyful and memorable moments at the University of Virginia and found it a super nice place. Faculty and staff of University of Virginia are very respectful and they help you as much as they can. I am more than proud to be an alumni of the the University of Virginia. It is also largely due to my colleagues in the E-Snail lab and the ELM group whom I need to thank. The friendly and collaborative relation between us allowed me to gain more knowledge in electrical engineering, physics, and materials science, and beyond. Both alumni and current members have been supportive and never hesitated to help.

I acknowledge the financial supports provided by the National Science Foundation (NSF),the Hobby fund, and the UVA endowed fellowship and the computing resources allocation by Rivanna cluster of UVA.

Last but not least, I want to thank my family members including my parents, my wife, and my siblings. Words fall short when I want to describe their support and help. I adamantly say this PhD dissertation would have been impossible without their understanding and unwavering support.

December 2022 ***Seyed Emad Rezaei***

Abstract

Conventional active coolers including water heat pumps and air conditioning have moving components that can cause mechanical failure and fatigue over time. They cannot be down-scaled to micron sizes and cannot be integrated into on-chip small-scale designs. Thermomagnetic and thermoelectric cooling systems emerged as an alternative to conventional active cooling systems. Thermomagnetic cooling systems are based on the Nernst-Ettingshausen effect that was observed in Bismuth for the first time. In the presence of an electric current and a perpendicular magnetic field, electrons and holes are pushed to opposite sides due to the Lorentz force. The migration of charge carriers develops a temperature gradient across the material, perpendicular to both electric current and magnetic field. Hence, heat can be pumped across the sample, this is the basis of Ettingshausen coolers. Similarly, applying a magnetic field perpendicular to a temperature gradient generates a transverse voltage difference, the so-called Nernst Voltage.

The primary objective of this dissertation is to develop a code to calculate the response of a system to the simultaneous presence of a magnetic field and a temperature gradient using first-principles density functional theory. First, I obtained the Nernst coefficient within constant relaxation time approximation to establish an insight into the Nernst effect and how it is related to the details of the band-structure. The aforementioned method is, however, unable to reconstruct the experimentally measured values as the Nernst coefficient is sensitive to the details of the relaxation times and in particular, it is proportional to the carrier mobility. Therefore, I implement the charge carrier relaxation time due to various scattering mechanisms including electron-phonon and electron-ionized impurity scattering in our theory. Experimental data of germanium, silicon, indium antimonide, and bismuth in a wide range of temperatures and doping concentrations were successfully reproduced. Furthermore, with the help of analytical models, I obtained a simplified model for the Nernst coefficient in order to find the material descriptors to predict the Nernst coefficient which turned out to be effective mass.

Lastly, I propose an approach to evaluate anomalous Nernst transport within the density functional theory framework. The semi-classical Boltzmann transport was modified by adding the effect of Berry curvature. Once the formalism was completed, the approach was imple-

mented on the basis set of maximally localized Wannier functions and applied to Fe_3Sn to replicate the experimental data.

Contents

LIST OF TABLES

LIST OF FIGURES

LIST OF SYMBOLS

ε	Electron energy
k	Wave vector
n	band index/carrier concentration
m	Effective mass
ν	Group velocity
ϵ	Dielectric constant
ω	Angular frequency
ph	phonon
e	electron
T	Temperature
E	Electric field
σ	Electrical conductivity
ρ	Electrical resistivity
S	Seebeck coefficient
N	Nernst coefficient
η	Ettingshausen coefficient
R	Hall coefficient
zT	Figure of merit
k_B	Boltzmann constant
$\hbar$	Reduced planck constant
κ	Thermal conductivity
Ω^B	Berry curvature
Ω	Ω operator
μ	chemical potential/ mobility
Ξ	Transport distribution function
$g(\varepsilon)$	Density of states
ε_g	Band gap
ε_v	Top of valence band
ε_c	Bottom of conduction band
$\mathcal{D}_A$	Acoustic phonon deformation potential

$\mathcal{D}_{op}$	Optical phonon deformation potential
$\mathcal{C}$	Elastic constant
ρ	Electrical resistivity/ mass density
N_{op}	Number of optical phonons
q_0	Inverse of screening length
d_{pz}	Piezoelectric stress constant
q	elementary charge/ wave vector
z	impurity charge
n_i	impurity concentration
V	unit cell volume

CHAPTER I

Introduction

1.1 Background

Waste heat is an inevitable by-product of power generation systems and electric circuits. According to the laws of thermodynamics, the maximum output power in any heat engine is limited and a fraction of heat is released to the surrounding ambient. Especially, waste heat flow becomes more significant in high-temperature industrial processes. Thermoelectric (TE) and thermomagnetic (TM) generators have emerged as promising ways to convert waste heat into electricity via the Seebeck and Nernst effects, respectively. In 1821, one year after Oersted's famous experiment, Thomas Johann Seebeck discovered the diffusive voltage response of electrons to an applied temperature gradient, a phenomenon that is named after him. The Seebeck effect is the basis of heat to electricity in thermoelectric power generators and temperature sensing in thermocouples. In 1886, Nernst and Ettingshausen discovered that applying a temperature gradient ∇T orthogonal to a magnetic field H in bismuth leads to a transverse electric field perpendicular to both H and ∇T [1] (Fig. 1.1).

This discovery opened a new path to convert wasted heat to electrical power and is the basis of thermomagnetic power generators. In addition, any heat engine can be operated in reverse mode and as a refrigerator. Hence, both thermoelectrics and thermomagnetics also have potential applications in cooling systems. Unlike conventional refrigerators, TE and TM refrigerators are CFC(Chlorofluorocarbons)-free and, consequently, environmentally friendly. The remarkable advantage of TE and TM generators is the direct energy conversion without any intermediate cycles. Additionally, there are no moving parts due to a lack of mechanical involvement which can lead to a longer life-span and a lower maintenance cost.

One of the first niches of TE generators was the aerospace section where safety and life-span are of great importance. TE generators based on spontaneous radioactive decay have

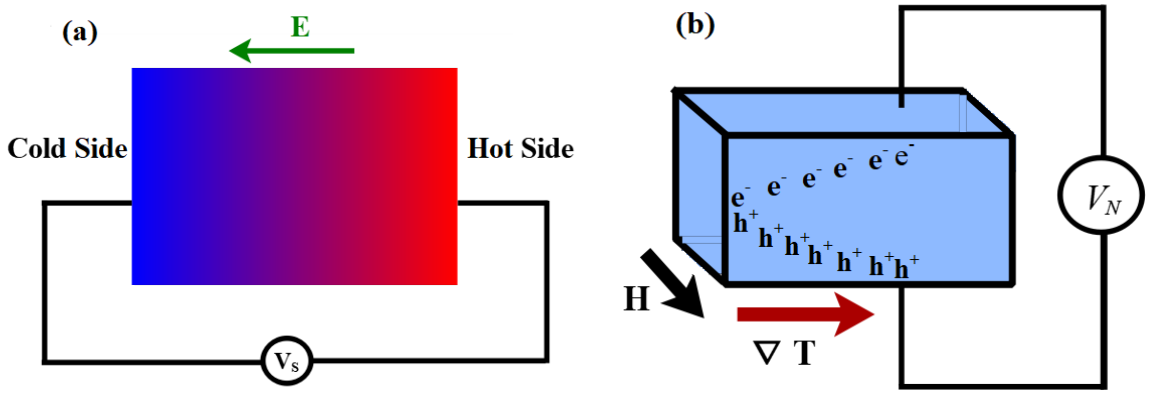

Figure 1.1: Schematic comparison of the Seebeck effect versus Nernst effects. An n-type Seebeck module in which the temperature gradient and the electric field are in the same direction(a). In a Nernst module electrons and holes move in opposite directions by the external magnetic field (H) (b).

been used to provide electricity for spacecrafts [2]. Energy Harvesting from the human body is desirable as an uninterrupted and consistent source of energy for wearable devices. The routine activities of a 150 lb [3] adult may develop over 100 Watts of power, through walking, breathing, and blood circulation. Recently, flexible TE generators have caught attention and various categories of structures such as bulk materials [4], thin films [5], fibers [6], organic compounds [7], and printable TE inks [8] have been studied. Flexible TE generators could be planted on the human body, however, plasticity is crucial for flexible TE generators to tolerate the deformation regarding the unusual geometries of the human body. Inspired by the self-healing feature of the human skin, self-healing electronic materials were expected to be efficient wearable thermoelectrics. Ren et.al. [9] fabricated a flexible TE generator by assembling modular thermoelectric chips, dynamic covalent polyimine, and flowable liquid-metal electrical wiring in a mechanical architecture design of soft motherboard-rigid plugin modules. They recorded an open-circuit voltage of 1 V/cm^2 at a temperature difference of 95 ^{0}C.

Years after Nernst-Ettingshausen's discovery, Smith started significant experiments on the thermomagnetic effect in metals. He reported the Nernst signal in nickel, cobalt [10], several rare metals, and alloys such as bismuth-tin, antimony, lead, and cadmium [11]. Furthermore, He managed to enhance the Nernst coefficient of nickel tenfold by alloying with copper and iron. [12].

Semiconductors were the next candidates. The Nernst coefficient of germanium at room temperature was measured to be as high as 350 $\mu V/KT$. [13] Indium antimonide is another semiconductor that showed relatively large values of the Nernst coefficient ($\sim$100 $\mu V/KT$) at 300 ^{0}K [14, 15].

On the theory side, several models have been developed for the thermomagnetic effect and in particular the Nernst effect. Moreau [16] stated that the Nernst coefficient is linearly proportional to the Thompson coefficient, the Hall coefficient, and the electrical conductivity. His relation was inspired by experimental observation and physical approximations and was shown to work for several samples. [16–19] Sommerfeld and Frank made the first attempt to model thermomagnetic effects using the electron theory of metals. [20] They obtained a distribution function in the presence of a magnetic field by solving the Boltzmann transport equation (BTE) and used linear response theory to obtain an equation for the Nernst coefficient. Sondheimer developed an equation for the Nernst coefficient in metals with the assumption of two partially filled spherical bands of s and d orbitals that are overlapping [21]. Callen [22] used the Onsager's reciprocity relations and expressed the thermomagnetic and galvanometric responses, and considered them as steady-state reversible thermodynamic processes. Putley [23] applied the Lorentz-Sommerfeld theory [24–26] to extract thermomagnetic and galvanomagnetic coefficients and obtained a close agreement between the theory and experiments for lead selenide and lead telluride. Price generated a phenomenological model for the Nernst coefficient in a two-band semiconductor using Boltzmann statistics [27]. In 1965, Delves [28] studied the symmetry of thermomagnetic properties of semiconductors and semimetals within the relaxation time approximation (RTA) and multivalley band structure. In the late 90's, Nakamura et.al. consistently studied the thermomagnetic effect in semiconductors for both parabolic [29] and non-parabolic [30] dispersion and compared the theory with experiments. They used a Maxwell-Boltzmann-like distribution function to analytically solve the BTE in the presence of a magnetic field. Table. 1.1 summarizes major equations of the Nernst coefficient developed in the past along with the physical quantities that determine the Nernst coefficient.

More recently, Liu et.al. [31] proposed that a magnetic field acts on the time evolution of wave vectors and accordingly alters the dc electrical conductivity. By using Wannier interpolation, the BTE under a magnetic field was numerically solved and electrical conductivity,

Table 1.1: Equations that have been proposed for the Nernst coefficient with quantities determining the Nearest coefficient. Parameters are described in the references [16, 20–23, 27, 28]

Author	Nernst coefficient	Quantities
Moreau	$\mathrm{TR}_H \sigma \frac{\partial S}{\partial T}$	Mobility and Thomson coefficient
Sommerfeld	$\frac{K_1 K_4' - K_2 K_3'}{\mu^2 K_1^2 + K_2^2}$	Mobility and Fermi level
Sondheimer	$\frac{K^2 T}{H\epsilon} \frac{(Q_s+Q_d)(V_s+V_d) - (P_s-P_d)(W_s-W_d)}{V}$	Effective mass and Fermi level
Callen	$\frac{L_{11}L_{14} - L_{12}L_{13}}{eHT(L_{11}^2 + L_{13}^2)}$	Seebeck coefficient and electrical conductivity
Putley	$-\frac{3\pi k_B q}{16} \frac{(n^2\mu_e^3 + p^2\mu_h^3) - np\mu_e\mu_h\mu(7+2E')}{\sigma^2}$	Mobility, DOS, and electrical conductivity
Price	$\frac{k}{ec}\left[\frac{\beta_{12}\sigma_1\sigma_2}{\sigma^2} + \frac{\beta_1\sigma_1}{\sigma} + \frac{\beta_2\sigma_2}{\sigma}\right]$	Mobility and electrical conductivity
Delves	$\frac{\sigma_{yx}M_{xx} - \sigma_{xx}M_{yx}}{H_z\sigma_{xx}\sigma_{yy}}$	DOS, In-plane and cross-plane electrical conductivity

Hall conductivity, and Hall coefficient were obtained for the case of MgB_2.

Recently, density functional theory (DFT) has emerged as a powerful method to calculate the electronic properties of materials [32]. Various codes were developed to compute the band-dependent quantities such as thermoelectric properties based on Fourier expansion of bands [33, 34] or maximally-localized Wannier function basis [35]. There are however very few first-principles studies of thermomagnetic and galvanometric effects up to now.

Macheda and Bonini [36] made the first attempt to model magnetoresistance using first-principles calculations to solve the linearized BTE through an iterative conjugate gradient algorithm. Band energies, band velocities, and electron-phonon scattering rates were computed via first-principles methods. Zhang et.al [37] probed the magnetoresistance of copper, bismuth, and WP_2 by combining the Fermi surfaces from first-principles and the BTE using the approach described in Ref. [31]. Lastly, Desai et.al. [38] replaced the force on electrons due to the presence of a magnetic field by $q\nu \times H$, where ν and H are band velocity and magnetic field, respectively. Very recently, quantities that rely on energy dispersion, e.g. mobility and electrical resistivity, were calculated through first-principles DFT implemented in the Perturbo code [39].

The solution of BTE under a temperature gradient and an electric field yields thermoelectric transport coefficients such as the Seebeck coefficient, electrical conductivity, and electronic thermal conductivity. Recently, Several codes have been developed to compute thermoelectric transport coefficients using first-principles density functional theory, though, the science and engineering community lacks a similar code to calculate thermomagnetic transport coefficients. In this work, I solve the Boltzmann Transport Equation (BTE) under open voltage conditions and in the presence of simultaneously applied magnetic field and temperature gradient and obtain the thermomagnetic transport coefficients, namely the Nernst, Hall, and Ettingshausen coefficients. The calculations are implemented in the framework of DFT and with maximally-localized Wannier functions basis, [40] within the Jones-Zener expansion [41]. In order to accomplish an insight into the Nernst effect, first I analyzed BTE within the constant relaxation time approximation. In Contrast to the Seebeck coefficient which is not sensitive to the details of the relaxation times, the Nernst coefficient is proportional to the carrier mobility and hence is greatly affected by the relaxation times. Therefore, In order to reproduce and predict experimental data, I advanced beyond constant relaxation time approximation by the inclusion of the electron-phonon and the electron-impurity relaxation times.

1.2 Objectives and scopes

The overarching objective of this work is to develop an approach to evaluate the Nernst coefficient using first-principles density functional theory within relaxation time approximation. Our approach overcomes the limitations of phenomenological methods that work only for specific materials and are not transferable. Unlike the empirical models, Our theory does not require fitting parameters and is based on the maximally localized Wannier functions. Band-dependent quantities such as velocity and effective mass tensor along with scattering rates due to various mechanisms are computed in Fourier space. The aforementioned quantities are coupled to derive the total distribution function followed by thermomagnetic coefficient calculation. Matrix analysis and arithmetic operations are carried out by accurate algebra libraries (LAPACK and BLAS) for numerical methods. Not only does our approach enable scientists and engineers to predict the thermomagnetic properties of materials, but it also provides a fundamental insight into the Nernst effect for technological applications.

Chapters of this dissertation are intended to be fairly self-supporting, such that readers interested in a specific aspect of thermomagnetic can start reading directly that chapter with no major dependence on the other chapters. For those interested, though, a reasonably thorough theory and background are provided. The next chapters of this study are presented as follows:

i. Thermoelectric
ii. Nernst Coefficient within CRTA
iii. Nernst Coefficient beyond CRTA
iv. Charge carrier relaxation time for doped semiconductors
v. Anomalous Nernst effect
vi. Conclusion and future works

CHAPTER II

Thermoelectric Materials

The Thermoelectric (TE) effect is the conversion of a temperature gradient into a potential difference. Thermal energy is one of the excessively available energy forms which is inevitably wasted in numerous sectors specifically electronics such as computers, electric circuits, and power transfer. A Thermoelectric module is capable of converting that heat loss to electric energy. In order to increase the output power, a thermoelectric generator is often made of many p-n pair thermocouples connected thermally in parallel and electrically in series (Fig 2.1). Assume A and B legs in Fig. 2.1 are n-type and p-type, respectively, the voltage at the external terminal connected to the p-type leg is shown by V_1 and voltage at the outside terminal connected to the n-type leg is V_2. An electrical load with the resistance of R_L is connected in series with the TE device which is composed of n TE couples. The equivalent resistance of the TE device couples is the summation of all resistors as they are connected in series R=n[R_p+R_n]. Similarly, the equivalent thermal conductance (K) of the device is K=n[K_p+K_n] as they are thermally connected in parallel.

In practical, there is always a contact resistance (R_a) in the device which should be taken into account. For the sake of simplicity, I estimate the electrical resistivity of n and p legs are equal, hence, the equivalent internal resistance is R=2nR_p+R_a and the voltage difference in the terminal and input electrical current become:

$$\begin{aligned} V_{TE} &= V_2 - V_1 = n[IR - S \cdot \Delta T] = n.I.R - V_S \\ I &= \frac{V_S}{n.R + R_L} = \frac{n.S\Delta T}{n.R + R_L} \end{aligned} \tag{2.1}$$

In which S is the Seebeck coefficient and S=S_A-S_B. The electric output power delivered by TE device to the load becomes P=n.(S.I.Δ-R.I^2)and the output power absorbed by the load is P=-V_{TE}.I=n.[R.I^2-S.I.ΔT]. The maximum electric output power happens when the output

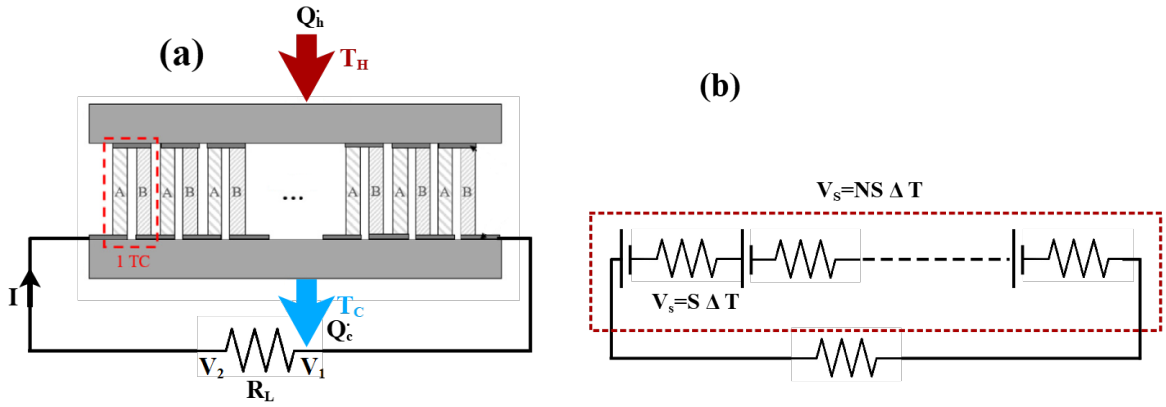

Figure 2.1: A schematic configuration of a thermoelectric generator containing thermocouples (TC) along with the temperature gradient (a). The equivalent electrical circuit of a thermoelectric generator with electrical resistors in series (b).

power is optimized with respect to the electric current.

$$P_{max} = \frac{n.(S.\Delta T)^2}{4R}$$
$$I_{max} = \frac{S.\Delta T}{2R} \tag{2.2}$$

The electrical output power becomes maximum if R=R_L. The heat flow absorbed at the hot junction of the TE device is assessed by $\dot{Q} = n.[S.T_H.I - \frac{R.I^2}{2} + K.\Delta T]$

The electrical efficiency of a TE generator is defined as the ration of the electric output power (P) to the heat input ($\dot{Q}$) absorbed at the hot side.

$$\eta = \frac{P}{\dot{Q}} = \frac{n.R_L.\Delta T.S^2}{K(n.R + R_L)^2 + n.(R_L.T_H + n.R.T).S^2} \tag{2.3}$$

Where T is the average temperature between hot and cold sides. Figure of merit for a TE device is defined as $zT = \frac{\sigma S^2 T}{\kappa}$, where σ and κ are electrical conductivity and thermal conductivity, respectively. TE efficiency (Eq. 2.3) could be simplified further.

$$\eta = \frac{\Delta T}{T_H} \frac{\sqrt{1+zT} - 1}{\sqrt{1+zT} + T_c/T_H} \tag{2.4}$$

2.1 Technological applications

Thermoelectric modules are of great interest in various applications such as electricity generation from waste heat [42–44], solid-state refrigeration [45, 46], active cooling [47, 48], small scale heat scavenging [49–51], spacecrafts [52, 53], health monitoring and tracking systems [54], and self-powered wireless platforms [55]. Thermoelectric modules' power generation efficiency and refrigeration coefficient of performance are assessed by the quality of the materials used as p and n legs.

Depending on desired power and dimensions, thermoelectric generations are categorized into bulk and micro thermoelectric generators. Bulk thermoelectric generators are widely used in industries and have dimensions as large as millimeters and develop large output power of as much as a few hundred watts. Micro thermoelectric generators operate with small values of the wasted heat and deliver output power in the order of milliwatts. I briefly introduce some thermoelectric applications in the next paragraphs.

Body heat is a form of waste heat that can be exploited to supply wearable and implanted medical devices for health monitoring and tracking systems as well as athletic wearable devices [54, 56]. Such wireless sensors monitor health and safety conditions. The rejected Heat from the human body is the driving force for these wearable devices. The application of wearable thermoelectric generators is not limited to patients, they are also employed in normal daily routines for calorie burning and sleep tracking. The average temperature difference between the human body and the atmosphere is around 13 ^{0}C which would be sufficient for wearable devices that need no more than 5 mW power to work [57]. More importantly, wearable thermoelectric generators excel the traditional implantable medical sensors in maintenance as they do not require batteries [58].

Wireless Sensor Networks have caught excessive attention recently. Wireless communication is used in the area of smart and advanced sensors network. Thermoelectric generators emerged as a complimentary part for wireless sensor networks in several ways such as Building Energy Management [59], electronic industry [60], and commercial and residential smart-buildings [61] where waste heat from water boilers, pipes, and air conditioners is ample. Moreover, thermoelectric-based self-powered wireless sensor networks have been recently exploited in aeronautical wireless sensors to control flight safety and security [62].

Due to dimensional restrictions of wireless sensor nodes, the thermocouple for this application needs to be minute and needs small temperature detection (heat source no more than 300 ^{0}K). Ideally, wireless sensor networks ought to be 10 to 100 mW of power consumption and 10 to 50 μW at sleep mode [58].Bi_2Te_3 was found to work efficiently for powering wireless sensor network nodes for building energy management [60].

Aerospace is another field that demands advances in thermoelectrics. Thermoelectric generators and radioisotope thermoelectric generators are commonly utilized in space crafts, satellites, and space probes. Radioisotope thermoelectric generators are heated through the enthalpy of the natural decay reaction of radioactive materials. Isotopes that are chosen as fuels must own certain physical and chemical features such as low radiation emission, specific half-life with the mission duration, stability at elevated temperatures, and high-power density. By far, only five radioactive isotopes have met the requirement posted by the Department Of Energy (DOE) and the US space missions: Plutonium-238 (Pu-238), Polonium-210 (Po-210), Strontium-90 (Sr-90), Cerium-144 (Ce-144), and Promethium-147 (Pm-147) [63]. Later on, NASA launched the first modulator general purpose heat source radioisotope thermoelectric generator on Galileo spacecraft [64]. Each modulator was fueled by Plutonium-238 and released 285 Watt energy at the beginning of the mission. The most recent version of the radioisotope thermoelectric generator for space missions is multi-mission radioisotope thermoelectric generator that is made of PbTe [65].

2.2 Boltzmann transport equation

The motion of an electron wave packet is often illustrated by wave vector (k) and location (r).

$$\begin{aligned} \dot{r} &= \frac{\partial \varepsilon_{n,k}}{\hbar \partial k} \\ \dot{k} &= \frac{q}{\hbar} E \end{aligned} \tag{2.5}$$

Boltzmann transport equation (BTE) details the behavior of a system that is thermodynamically not in the equilibrium state due to a driving force. Examples of driving forces that push a system out of equilibrium are gradients of temperature, chemical potential, and electric charge. BTE under a temperature difference and an electric field is commonly used to de-

scribe the Seebeck effect in solid-state devices. The probability of a carrier with wave vector k, being at position r at time t is assessed by the distribution function f which contains an equilibrium part (f_k^0) and a non-equilibrium counterpart (f_k). A crude approximation is BTE within constant relaxation time approximation (CRTA) that is regularly considered to find the distribution function and, consequently, evaluate the transport properties of materials.

$$(\dot{k} \cdot \nabla_k + \dot{r} \cdot \nabla_r) f_k = \frac{f_k^0 - f_k}{\tau} \tag{2.6}$$

Replacing the equations of motion 2.5 in BTE 2.6 results in an equation for the distribution function.

$$qE \cdot \nabla_k f_k + \frac{\partial \varepsilon_{n,k}}{\partial k} \cdot \nabla_k f_k = \frac{f_k^0 - f_k}{\tau} \tag{2.7}$$

$\frac{\partial \varepsilon(n,k)}{\partial k}$ is $\hbar\nu$ where ν is the band velocity. On the other hand, derivatives with respect to k can be turned into derivatives with respect to energy, and the deviation of the distribution function from the equilibrium is shown by $f_k^1 = f_k - f_k^0$.

$$\nu \cdot \left[qE + T\nabla(\frac{\varepsilon_{n,k} - \mu}{T}) \right] \frac{\partial f_k^0}{\partial \varepsilon} = -\frac{f_k^1}{\tau} \tag{2.8}$$

The electrical conductivity (σ), the Seebeck coefficient (S), and the electronic part of thermal conductivity (κ_e) tensors at a given temperature, T, can be obtained from:

$$\frac{\sigma_{ij}}{q^2} = \int (-\frac{\partial f(\varepsilon, \mu, T)}{\partial \varepsilon}) \, \Xi_{ij}(\varepsilon) \, d\varepsilon \tag{2.9}$$

$$\frac{(\sigma \cdot S)_{ij} T}{q} = \int (-\frac{\partial f(\varepsilon, \mu, T)}{\partial \varepsilon})(\varepsilon - \mu) \Xi_{ij}(\varepsilon) d\varepsilon \tag{2.10}$$

$$K_{ij} T = \int (-\frac{\partial f(\varepsilon, \mu, T)}{\partial \varepsilon})(\varepsilon - \mu)^2 \Xi_{ij}(\varepsilon) d\varepsilon \tag{2.11}$$

in which q is the electron charge, μ is the chemical potential, and $\Xi(\varepsilon)$ is the transport distribution function (differential conductivity) which is defined as:

$$\Xi_{ij}(\varepsilon) = \frac{1}{V N_k} \sum_{n,k} \nu_i(n,k) \nu_j(n,k) \tau \delta(\varepsilon - \varepsilon_{n,k}) \tag{2.12}$$

where V is the unit cell volume and $\nu_i(n,k)$ is the ith Cartesian component of the velocity of the nth band at wave vector k with N_k k-points. The electronic part of the thermal conductiv-

ity is given by $\kappa_{el} = K - \sigma S^2 T$. Finally, τ is electron relaxation time. Although a constant relaxation time might be a reasonable assumption for the evaluation of the Seebeck coefficient, for an accurate evaluation of the intrinsic electrical and electronic thermal conductivity, one needs to quantitatively calculate electron-phonon and ionized impurity scattering rates as a function of energy. Multiple post-processing codes have been developed to obtain thermoelectric coefficients within CRTA, namely, BoltzWann [35] and BoltzTraP [33]. BoltzWann code performs integration with a maximally-localized Wannier functions basis set, whilst, BoltzTraP is based on a smoothed Fourier interpolation of electronic structure.

2.3 BTE analytical solution

Occupation probability of a state with energy ε is given by the equilibrium Fermi- Dirac distribution function at a chemical potential (μ).

$$f^0(\varepsilon) = \frac{1}{1 + \exp\left(\frac{\varepsilon - \mu}{k_B T}\right)} \tag{2.13}$$

Having the distribution function along with the density of states ($g(\varepsilon)$), the electron (n_e) and hole concentrations(p_h) at a given chemical potential can be attained.

$$\begin{aligned} n_e &= \int_{\varepsilon_c}^{\infty} f(\mu, \varepsilon, T) g(\varepsilon) d\varepsilon \\ p_h &= \int_{-\infty}^{\varepsilon_v} \big[1 - f(\mu, \varepsilon, T)\big] g(\varepsilon) d\varepsilon \end{aligned} \tag{2.14}$$

Where ε_v and ε_c are the top of the valence band and the bottom of the conduction band, respectively. Boltzmann transport equation 2.8 within relaxation time approximation can be analytically solved. For the sake of simplicity, I reduce the BTE in 1-D, along the x-axis.

$$\nu \cdot \Big[\frac{\partial \mu}{\partial x} + (\frac{\varepsilon - \mu}{T})\frac{\partial T}{\partial x}\Big]\frac{\partial f_k^0}{\partial \varepsilon} = -\frac{f_k^1}{\tau} \tag{2.15}$$

Electric (J) and heat (Q) currents are defined as below:

$$\begin{aligned} J &= \int q\nu f(\varepsilon) g(\varepsilon) d\varepsilon \\ Q &= \int q\nu(\varepsilon - \mu) f(\varepsilon) g(\varepsilon) d\varepsilon \end{aligned} \tag{2.16}$$

From the BTE(Eq. 2.15) the electric current is expressed as a function of velocity.

$$J = \int q\nu_x^2 \tau g(\varepsilon)[\frac{\partial \mu}{\partial x} + (\frac{\varepsilon - \mu}{T})\frac{\partial T}{\partial x}]\frac{\partial f_k^0}{\partial \varepsilon}d\varepsilon \tag{2.17}$$

For a parabolic dispersion $g(\varepsilon) = \frac{m\sqrt{2m\varepsilon}}{4\pi^2\hbar^3}$ and $\nu_x^2 = \frac{2\varepsilon}{3m}$, so that the current equation 2.17 is simplified.

$$J = \frac{2q\sqrt{2m}}{3\pi^2\hbar^3}\int \varepsilon^{3/2}\tau\Big[\frac{\partial \mu}{\partial x} + (\frac{\varepsilon - \mu}{T})\frac{\partial T}{\partial x}\Big]\frac{\partial f_k^0}{\partial \varepsilon}d\varepsilon \tag{2.18}$$

Electrical conductivity (σ) is the ratio of the electric current to the electric field in the absence of the temperature gradient. Seebeck coefficient is determined by the ratio of the electric field to the temperature gradient in an open circuit condition (J=0).

$$\begin{aligned} \sigma &= \frac{J}{\partial \mu/q\partial x} = \frac{2q^2\sqrt{2m}}{3\pi^2\hbar^3}\int \varepsilon^{3/2}\tau\frac{\partial f_k^0}{\partial \varepsilon}d\varepsilon \\ S &= \frac{E}{\partial T/\partial x} \end{aligned} \tag{2.19}$$

I also introduce the Fermi-Dirac integral in order to summarize the mathematical equations.

$$\mathcal{F}_n(z) = \int_0^\infty z^n f^0(z)dz \tag{2.20}$$

2.3.1 Metals and degenerate semiconductors

In case of metals and degenerate semiconductors, Fermi-Dirac integral turns into the familiar Γ integral. Also, Sommerfeld expansion [20, 25] holds true for metals and heavily doped semiconductors. So that the Fermi-Dirac integral is reduced to $\mathcal{F}_n(z) = \frac{z^{n+1}}{n+1}$. After doing some algebra electrical conductivity for metals and degenerate semiconductors will be earned.

$$\sigma(\mu) = \frac{2\tau q^2\sqrt{2m}}{3\pi^2\hbar^3}\mu^{3/2} \tag{2.21}$$

From Eq. 2.18 and 2.21 and the Sommerfeld expansion the electric current equation can be written as a function of electrical conductivity.

$$J = -\frac{1}{q}\frac{\partial \mu}{\partial x}\sigma - \frac{1}{qT}\frac{\partial T}{\partial x}\frac{\pi^2}{3}(k_B T)^2 \frac{2q^2\sqrt{2m}}{3\pi^2\hbar^3}\frac{\partial(\varepsilon^{3/2}\tau)}{\partial \varepsilon}\Big|_{\varepsilon=\mu} \tag{2.22}$$

The Seebeck coefficient is defined in an open-circuit condition and to clarify the above equation, I introduce a new parameter as $\sigma(\varepsilon) = \frac{2q^2\tau\sqrt{2m}\varepsilon^{3/2}}{3\pi^2\hbar^3}$.

$$S = -\frac{\pi^2}{3q}k_B^2 T \frac{\partial ln(\sigma(\varepsilon))}{\partial \varepsilon}\Big|_{\varepsilon=\mu} \tag{2.23}$$

The above equation is known as the Mott formula. Importantly, for metals and heavily doped semiconductors the Seebeck coefficient grows versus temperature. Relaxation time is often approximated as a power function of energy ($\tau = \tau_0 \varepsilon^r$) that leads to a well-defined formulation for the Seebeck coefficient in metals and heavily doped semiconductors.

$$S = \frac{\pi^2 k_B^2 T}{3q}\frac{r + 3/2}{\mu} \tag{2.24}$$

Having the physical constants replaced in Eq. 2.24 the Seebeck coefficient of metals and heavily doped semiconductors would be no more than a few tens of $\mu V/K$ and it is inversely proportional to chemical potential.

2.3.2 Non-degenerate semiconductors

For a non-degenerate semiconductor the Fermi-Dirac distribution function is estimated as $\exp\left(\frac{\mu-\varepsilon}{k_B T}\right)$ and thus the Fermi-Dirac integral turns into $\mathcal{F}_n(z) = \exp(z)\Gamma(n+1)$, where $\Gamma(z) = \int_0^\infty u^{z-1} exp(-u) du$. With the same assumptions of a parabolic dispersion and a power function for relaxation time, in an analogous way, the electrical conductivity and Seebeck coefficient for a non-degenerate semiconductor are derived.

$$\begin{aligned} \sigma(\mu) &= \frac{q^2\tau_0(r+3/2)}{3\pi^2 m}\Big(\frac{2mk_B T}{\hbar^2}\Big)^{3/2}\Gamma(r+3/2)\exp\Big(\frac{\mu}{k_B T}\Big) \\ S &= \frac{k_B}{q}\Big(\frac{\mu}{k_B T} - r - 5/2\Big) \end{aligned} \tag{2.25}$$

In contradiction with metals, the Seebeck coefficient for a non-degenerate semiconductor is linearly proportional to chemical potential and even for a chemical potential as low as 0.1 eV the Seebeck coefficient can reach nearly $100\mu V/K$. This is a single band model and as an example for a two band system, both bands (valence and conduction) contribute from each band.

$$\begin{aligned}
\sigma_v(\mu) &= \frac{q^2\tau_0(r+3/2)}{3\pi^2 m_v}\Big(\frac{2m_v k_B T}{\hbar^2}\Big)^{3/2}\Gamma(r+3/2)\exp\big(\frac{\varepsilon_v-\varepsilon}{k_B T}\big)\\
S_v &= \frac{k_B}{q}\Big(\frac{\varepsilon_v-\varepsilon}{k_B T}-r-5/2\Big)\\
\sigma_c(\mu) &= \frac{q^2\tau_0(r+3/2)}{3\pi^2 m_c}\Big(\frac{2m_c k_B T}{\hbar^2}\Big)^{3/2}\Gamma(r+3/2)\exp\big(\frac{\varepsilon-\varepsilon_c}{k_B T}\big)\\
S_c &= -\frac{k_B}{q}\Big(\frac{\varepsilon-\varepsilon_c}{k_B T}-r-5/2\Big)
\end{aligned} \tag{2.26}$$

The total electrical conductivity is $\sigma = \sigma_v + \sigma_c$ while the total Seebeck coefficient is the average Seebeck coefficient weighted by electrical conductivity $S = \frac{\sigma_v S_v + \sigma_c S_c}{\sigma_v + \sigma_c}$.

2.4 Semimetals

The search for efficient TE materials with a large figure of merit [66] has been going on for two centuries. Metals were the first class of materials studied for thermoelectric applications. While they have large electrical conductivity, they usually have small Seebeck coefficient values and large thermal conductivity values, making them nonideal candidates for traditional thermoelectric applications. Semiconductors usually own Seebeck coefficient values that are orders of magnitude larger than metals. The large Seebeck coefficient is the result of the presence of the band gap which breaks the symmetry between electrons and holes. There are two major competing factors in the optimization of the figure of merit in semiconductors. First, when the Fermi level is inside the band gap, the Seebeck coefficient is large. As the Fermi level moves into the valence or conduction bands, the difference between the density of states (DOS) of hot electrons (above the Fermi level) and cold electrons (below the Fermi level) becomes small, and so does the Seebeck coefficient. On the contrary, the electrical conductivity increases since there are more available electronic states. As a result, one needs to adjust the position of the Fermi level to optimize the thermoelectric power factor, $PF = \sigma S^2$. Second, as the Fermi level moves inside the band, similar to the electrical

conductivity, the electronic part of the thermal conductivity also increases. It is therefore difficult to design a material with a very large figure of merit although no theoretical upper limit has been found for zT.

Semimetals are a class of materials with properties in between semiconductors and metals. They usually have a very small overlap of bands and therefore while they do not have an energy gap, their intrinsic carrier density can vary in a large range, between $10^{15} - 10^{20}$ cm^{-3}, depending on the band overlap and the size of the carrier pockets. For example, the intrinsic concentrations at liquid helium temperature 4.2 K are about 5.0×10^{15} cm^{-3} for HgTe [67], 3.6×10^{16} cm^{-3} for HgSe [68], 2.7×10^{17} cm^{-3} for Bi [69], 3.7×10^{19} cm^{-3} for Sb [69], and 2.0×10^{20} cm^{-3} for As [69]. These values are much smaller than in metals, which are typically around 10^{23}cm^{-3}, and are comparable with and in some cases smaller than in heavily-doped semiconductors used for thermoelectric applications, $10^{18} - 10^{20}$ cm^{-3}. However, semimetals generally have much larger carrier mobility values compared to metals and heavily doped semiconductors. For example, electron mobilities at 4.2 K are 6.0×10^5 $cm^2V^{-1}s^{-1}$ in HgTe [67], 1.2×10^5 $cm^2V^{-1}s^{-1}$ in HgSe [70, 71] and 11×10^7 $cm^2V^{-1}s^{-1}$ in Bi [69] and at room temperature are 3.5×10^4 $cm^2V^{-1}s^{-1}$ in HgTe [72], 2.0×10^4 $cm^2V^{-1}s^{-1}$ in HgSe [73, 74] and 1.2×10^4 $cm^2V^{-1}s^{-1}$ in Bi [75]. As a result, the electrical conductivity of semimetals is comparable to those of heavily-doped semiconductors. Note that the carrier mobility is much lower in heavily-doped semiconductors due to ionized impurity doping and in metals due to electron-electron and electron-phonon interactions. The thermal conductivity values in semimetals could be also small, especially if they consist of heavy elements. For example, the thermal conductivity at room temperature is about 1.7 $Wm^{-1}K^{-1}$ in HgSe [76], 1.9-2.9 $Wm^{-1}K^{-1}$ in HgTe [76, 77], 6.0 $Wm^{-1}K^{-1}$ in the trigonal direction in pure bismuth [78–80] and could be as low as 1.6 $Wm^{-1}K^{-1}$ in Bi-Sb alloys [79, 81].

Semimetallic and zero gap materials show many interesting properties. They have attracted interest as topologically nontrivial materials [82]. Many of them have strong spin-orbit coupling and comprise of heavy elements. As a result, they possess a low thermal conductivity. Inversion of bands happens in many of the zero-gap alloys such as Bi_xSb_{1-x} [83] and $Hg_xCd_{1-x}Te$ [84], leading to interesting transport properties. While many of these materials have been studied in other fields, there has not been a systematic study of their thermoelectric

properties due to their lack of band gap.

If one is to avoid doping and only choose to work with intrinsic materials, semimetals would be the best potential candidate for having a large thermoelectric power factor [85]. Furthermore, the presence of heavy elements would lower the lattice thermal conductivity, and as a consequence paves the way to achieve greater efficiency. In other words, semimetals are the most efficient choice to achieve high efficiency without doping [86]. This motivates our hypothesis that zero or small band gap materials have the potential of being good thermoelectrics with high power factor PF and zT. We were then encouraged to investigate TE properties of several chemically stable semimetals at room temperature (table 2.1).

In this section, the thermoelectric response of several semimetallic elements, i.e. their Seebeck coefficient values, are studied using first-principles calculations with proper corrections for the energy levels. We restrict ourselves to room temperature where the diffusive part of the Seebeck coefficient is known to be dominant. The rationale to focus only on the Seebeck coefficient is the following: As was discussed, the carrier mobility is expected to be large in semimetals. If semimetals consist of heavy elements, then their thermal conductivity is also expected to be low. The biggest concern with semimetals is therefore the Seebeck coefficient and thus the process of searching for good semimetals for thermoelectric applications should start with the scan for the Seebeck coefficient. From a computational point of view, among the three transport properties determining the figure of merit, the Seebeck coefficient is the least sensitive one to the scattering rates. Therefore, the only property that could be reliably calculated under constant relaxation time approximation and still be of value is the Seebeck coefficient. We should acknowledge that even Seebeck coefficient values can be modified when energy dependent relaxation times are introduced [77, 87–89]. Including energy dependent relaxation times would be a very difficult task when scanning many materials. Here, as the first step towards finding promising semimetallic candidates, we limit ourselves to the constant relaxation time approximation.

In this work, semimetals are divided into three categories based on the band forms (See Fig .2.2). The first group possesses a distinct feature in the band structure: the lowest conduction band has a deep minimum at the center of the Brillouin zone (BZ) where it overlaps with the highest valence bands. When the two bands are symmetric (shown by black curves),

Material	Crystal	Group#	N_{atoms}	E_g (eV) **PBE**	E_g (eV) **HSE/mBJ**	m_h^*/m_e^* **PBE**	m_h^*/m_e^* **HSE/mBJ**
HgTe	cubic	216	2	-0.019	-0.009	3.71	16.29
HgSe	cubic	216	2	-0.018	-0.009	10.34	17.63
HgS	cubic	216	2	0.038	0.305	19.63	25.45
TlP	cubic	216	2	-0.018	0.000	2.52	18.18
TlAs	cubic	216	2	-0.019	-0.009	3.28	1.58
Li_2AgSb	cubic	216	2	-0.009	0.676	0.02	0.08
Na_2AgSb	cubic	216	2	-0.009	0.000	34.59	51.50
Rb_2AgSb	cubic	216	2	-0.020	-0.008	2.51	56.84
α-Sn	cubic	227	2	-0.031	-0.030	0.171	0.30
Bi	trigonal	166	2	-0.122	-0.061	1.711	5.87
Sb	trigonal	166	2	-0.09	-0.039	7.22	1.28
TaAs	tetragonal	109	4	0.062	-0.003	13.92	3.73
TaP	tetragonal	109	4	-0.15	-0.092	1.81	0.13
NbP	tetragonal	109	4	-0.152	0.061	0.07	0.25
Mg_2Pb	cubic	225	3	-0.793	-0.427	0.12	0.11
$PtSb_2$	cubic	205	12	-0.110	-0.083	0.69	0.48
TiS_2	trigonal	164	3	-0.226	0.396	0.13	0.24
$TiSe_2$	trigonal	164	3	-0.623	-0.346	N/A	N/A

Table 2.1: Summary of 18 materials studied in this work including their crystal structure, space group number, number of atoms per unit cell, band gap in PBE and HSE calculations as well as the ratio of hole effective mass to electron effective mass.

the intrinsic chemical potential is expected to be at the midpoint between the two band extrema, and the intrinsic Seebeck coefficient is expected to be very small. However, it is possible to have a band structure similar to the red curve in Fig 2.2a, where the low degeneracy of the conduction band in the vicinity of the Γ point results in a small density-of-states (DOS), the magnitude of which is essentially defined by the electron's effective mass (*i.e.* the curvature of the band). On the other hand, valence bands have heavier effective masses and higher degeneracy with contributions from elsewhere in the BZ. As a result, the DOS is asymmetric around the chemical potential. This is known to be beneficial for the material's electronic properties in general and, in particular, leads to a high Seebeck coefficient. A typical example of such material is HgTe which has been studied in our recent publication both theoretically and experimentally [77]. Other (predominantly cubic) materials are HgSe and HgS, TlAs and TlP [90], α-Sn as well as inverse Heusler materials (Li_2AgSb, Na_2AgSb, Rb_2AgSb) [90, 91]. The band structures of these materials along with their DOS are shown in the Supplementary Material. Here, as the representative of this class of materials, we show the band structure and the DOS of HgTe as shown in Fig. 2.2a. Black curves are used to show PBE results for the band structure and the DOS of all materials reported in this work. Red

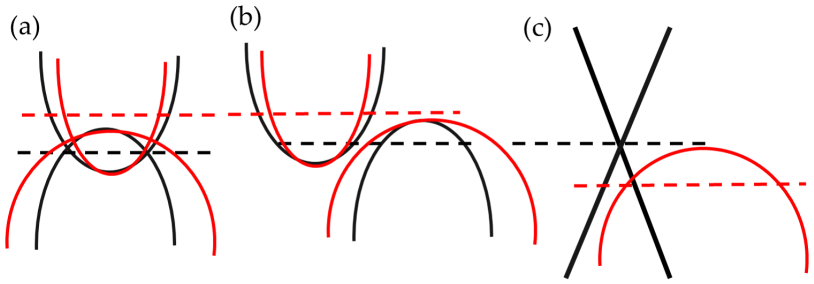

Figure 2.2: Energy dispersion (red:symmetric, black:asymmetric) of three categories of semimetals:(a) direct semimetal with parabolic bands, (b) indirect semimetal with parabolic bands, (c) Dirac or Weyl semimetal with linear dispersion. The Fermi level is denoted by the dashed line.

curves show the HSE results.

Among the materials studied within the first class, the hybrid functional calculations (red curves) reveal that HgS and Li_2AgSb are in fact semiconductors with band gaps of 0.33 eV and 0.67 eV respectively. In almost all cases, we note that the effective masses of the conduction band significantly decrease in HSE compared with PBE calculations. A possible explanation for this effect has been given in Ref. [92] where the small effective masses were attributed to the strong level repulsion between the s-like conduction band and p-like valence band at Γ. This repulsion is inversely proportional to the square of the difference between these two levels [92] which reduces from -0.93 eV for PBE to -0.27 eV for HSE06 in case of HgTe [77, 84] The second group (Fig. 2.2b) includes other semimetallic materials without any distinct feature in their band structure but possessing a low density of states at the Fermi level. The top of the valence band and the bottom of the conduction band are at different k points as shown schematically in Fig. 2.2b. Electron and hole pockets coexist. This class includes, for instance, Mg_2Pb, cubic pyrite structures ($PtSb_2$ and $PtBi_2$) [93–95], TiS_2, $TiSe_2$, TaP, NbP, and $\alpha-Zn_3Sb_2$. [96] We note TiS_2 gap opens up when HSE functional is used and therefore this material is a semiconductor with a band gap of 0.4 eV. Despite its large Seebeck coefficient which is expected for a material with a band gap, the intrinsic carrier concentration is low and therefore it does not fall in the class of materials we are interested in this work. On the other hand, $TiSe_2$ remains semimetallic under HSE, with overlapping conduction (L and M points) and valence bands (Γ point). Its Seebeck coefficient is however found to be small due to the small asymmetry in the bands. In another work where properties of the monolayer $TiSe_2$ were studied[97], we found that the band gap can be opened under

tensile strain, leading to a metal-insulator transition and corresponding non-linear effects. As for Mg_2Pb, the overlap of bands is relatively large and the ratio of the DOS effective mass of the conduction band to that of the valence band is close to one. (see Fig. 2.3b) Therefore this material exhibits a small intrinsic Seebeck coefficient value of about -10$\mu V/K$.

The third class of materials includes relativistic (Dirac and Weyl) semimetals with linear bands close to the Fermi level. These are schematically shown in Fig. 2.2c. The examples include Bi, Sb, Na_3Bi and TaAs-family and inverse Heusler materials Na_2AgSb and Rb_2AgSb. Thermoelectric properties of the latter family as well as some other topologically non-trivial semimetals have been recently investigated in Ref. [82]. The band structure of Bi as the representative of this class of materials is shown in Fig. 2.3c. Most samples in this group demonstrate rather small Seebeck coefficient values. This is expected because there is an inherent symmetry in the band structure at the Dirac point.

We performed density functional theory calculations using Vienna ab initio simulation package (VASP) [98, 99]. Pseudopotentials based on the projector augmented wave method with the generalized gradient approximation by Perdew, Burke, and Ernzehof (GGA-PBE) [100] and hybrid Heyd-ScuseriaErnzehof (HSE06) [101] exchange-correlation (XC) functionals were employed to compute the electronic structure. Since Spin-orbit coupling plays a significant role in calculations, we include it in all calculations. Transport calculations are performed within the constant relaxation time approximation (CRTA) as implemented in Boltz-Wann [35] and BoltzTraP [33, 34] packages to achieve the diffusive part of the Seebeck coefficient. Several of the samples that we have studied in this work have Seebeck coefficient values larger than 100$\mu V/K$ as shown in Fig 2.4. We expect the Seebeck coefficient to be large only when there is a band gap or when there is an asymmetry between electron and hole effective masses. To show this we start by using the equation for bipolar Seebeck coefficient under constant relaxation time approximation [102].

$$S= - \frac{k_B}{2q} \left[\frac{\sigma_e - \sigma_h}{\sigma_e + \sigma_h} (\beta E_g + 5) + \beta(\varepsilon_c + \varepsilon_v - 2\mu) \right] \tag{2.27}$$

where k_B is the Boltzmann constant, q is the elementary charge, $\beta = (k_B T)^{-1}$, σ_e and σ_h are electron and hole conductivities. The band gap E_g is defined similarly to semiconductors as a difference between the bottom of the conduction band ε_c and the top of the valence

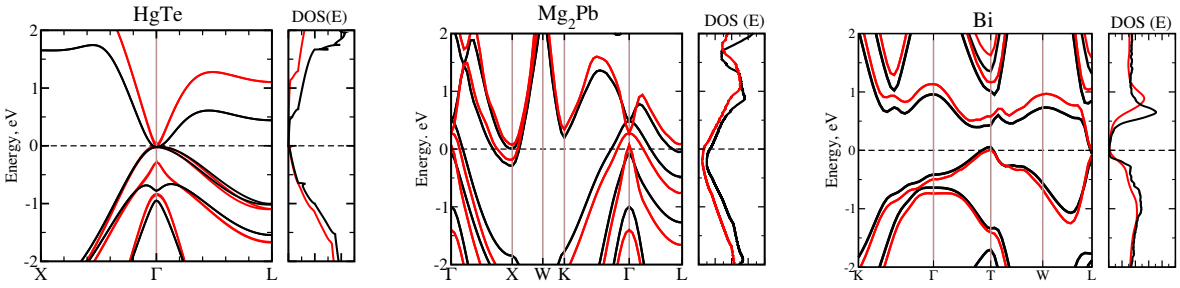

Figure 2.3: The band structures (left panels) and density of states (right panels) of HgTe, Mg_2Pb, and Bi represent the three types of semi-metals described above. Black curves - PBE, red curves - HSE06.

band ε_v and μ is the chemical potential. The band gap E_g is positive for semiconductors and negative for semimetals where there is band overlap. Its values for different materials studied in this work are listed in Table 2.1. For symmetric bands ($m_e = m_h$) the first term in Eq. 2.27 is zero and the Seebeck coefficient grows linearly with the distance of the chemical potential from the middle of the gap. When the gap is small compared to k_BT, the Seebeck coefficient strongly depends on the band asymmetry characterized by $\frac{m_e - m_h}{m_e + m_h}$ or more generally on $\frac{\sigma_e - \sigma_h}{\sigma_e + \sigma_h}$. Assuming non-degenerate statistics, constant relaxation time approximation, and intrinsic conditions ($n = p$), one can simplify Eq. 2.27 to

$$S_{int} = -\frac{k_B}{2q}\left[\frac{\gamma - 1}{\gamma + 1}(\beta E_g + 5) - \frac{3}{2}\ln(\gamma)\right] \tag{2.28}$$

where γ is defined as the effective mass ratio of holes to electrons (listed in Table 2.1). Note that the condition $n = p$ automatically places the chemical potential at its intrinsic level, and we do not need to specify it. Equation 2.28 clearly shows that there are two parameters to which the intrinsic Seebeck is sensitive: one is the band gap and the other is the mass ratio. To demonstrate this, we extract an effective mass from the density of states estimated from the slope of the density of states of the electrons (conduction band) and the holes (valence band) with respect to the square root of energy. The absolute value of the intrinsic Seebeck coefficient of different materials with respect to their effective mass ratio (effective mass of the holes to that of the electrons) and band gap energy is plotted in Fig. 2.4. We see an increasing trend in the Seebeck coefficient values with respect to the mass ratio for semimetals where the band gap is zero or close to zero. In Fig. 2.5 our computational results are compared to reported experimental values of α-Sn, α-HgS, HgSe, HgTe, TiS_2, TaAs and

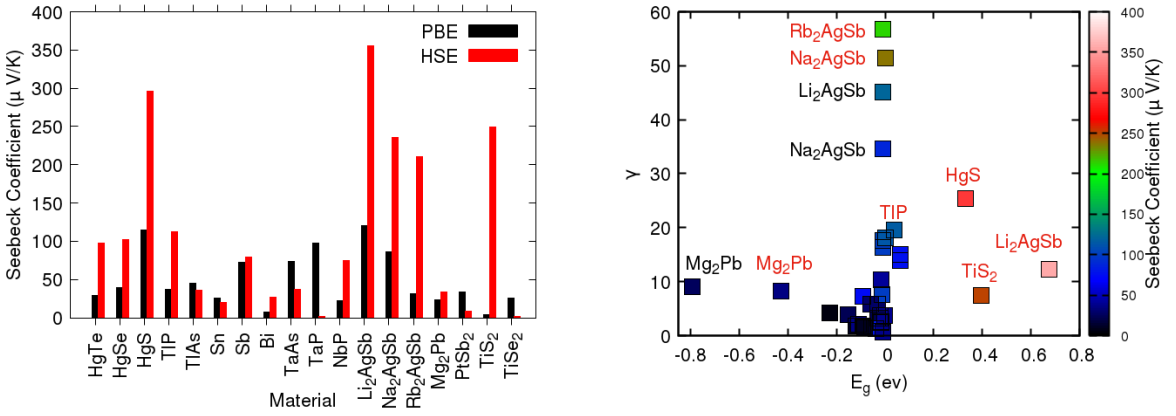

Figure 2.4: Left panels: Absolute value of intrinsic Seebeck coefficient calculated using PBE (black) and HSE (red). Right panels: Absolute value of intrinsic Seebeck coefficient (color bar) as a function of band gap E_g (x-axis) and effective mass ratio γ (y-axis).

$PtSb_2$.As shown in Fig. 2.5, and considering there are no fitting parameters, the agreement between theory and experiment is satisfactory.

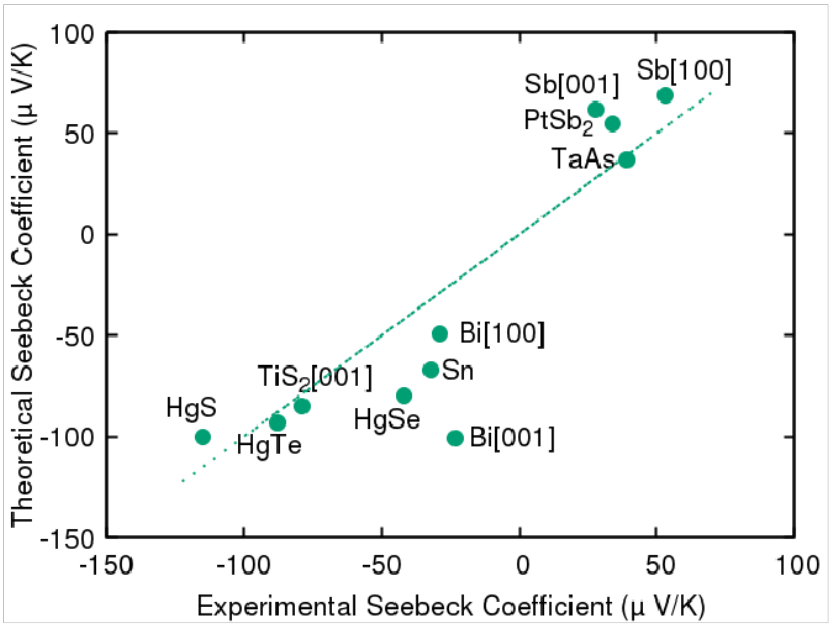

Figure 2.5: Computational Seebeck coefficient values calculated in this work using HSE band structures versus experimental Seebeck coefficient values from literature [103–111].

CHAPTER III

Nernst coefficient within CRTA

In response to external fields, at a point k in the reciprocal space, the distribution function f_k deviates from the equilibrium distribution function f_k^0 as f_k=$f_k^0 + f_k^1$. The force acting on a moving particle due to a magnetic field (H) is described by Lorentz force $q\nu \times H$, and accordingly, the BTE within constant relaxation time approximation (CRTA) needs to be modified as follows [112]:

$$\frac{q}{\hbar}\nu \times H \cdot \nabla_k f_k^1 + \nu \cdot [qE + T\nabla(\frac{\varepsilon_{n,k} - \mu}{T})]\frac{\partial f_k^0}{\partial \varepsilon} = -\frac{f_k^1}{\tau} \tag{3.1}$$

Where q is the electron charge, $\hbar$ is the Planck constant, T is the temperature, E is the electric field, $\varepsilon_{n,k}$ is the energy of the k wave vector with the band index of n and μ is the chemical potential. Eq. 8.1 can be abbreviated by introducing a generalized force, F, and a band operator, Ω defined as follows:

$$\begin{aligned} F &= -\nabla\mu - \frac{(\varepsilon_{n,k} - \mu)}{T}\nabla T \\ \Omega &= \frac{q}{\hbar}\nu \times H \cdot \nabla_k = \frac{q}{\hbar}\nu_j H_k \epsilon_{ijk}(\frac{\partial}{\partial k_i}) \end{aligned} \tag{3.2}$$

Replacing 8.2 in 8.1 leads to an equation for f_k^1:

$$f_k^1 = (1 + \tau\Omega)^{-1}\tau\nu \cdot F(-\frac{\partial f_k^0}{\partial \varepsilon}) \tag{3.3}$$

When $\tau\Omega$ is small, that is at small magnetic fields, the term $(1 + \tau\Omega)^{-1}$ can be expanded according to the Jones-Zener expansion [41]:

$$(1 + \tau\Omega)^{-1} = 1 - \tau\Omega + (\tau\Omega)^2 - \dots \tag{3.4}$$

For the Nernst effect, the first two terms (1-$\tau\Omega$) are required to obtain a response linear in H, and higher order terms are neglected, thus, the transport distribution function (Eq. 3.3) can be rewritten as:

$$f_k^1 = -F_i \frac{\partial f_k^0}{\partial \varepsilon} \tau [1 - \tau\Omega] \nu_j \tag{3.5}$$

Following Smith's notations [112, 113], I define transport coefficients($(ij)_H$) and physical constants (G) as comprehensive tensors.

$$\begin{aligned} (ij)_H &= \begin{pmatrix} \sigma_{ij}(H) \\ B_{ij}(H) \\ \rho_{ij}(H) \\ K_{ij}(H) \end{pmatrix} \\ G &= \begin{pmatrix} q^2 \\ \frac{q}{T}(\varepsilon - \mu) \\ q(\varepsilon - \mu) \\ \frac{(\varepsilon-\mu)^2}{T} \end{pmatrix} \end{aligned} \tag{3.6}$$

Similar to thermoelectric effects [114], I shall define a transport distribution function (Ξ^H) for thermomagnetic effect which relates the $(ij)_H$ and G tensors as below:

$$\begin{aligned} (ij)_H &= \int G\, \Xi_{ij}^H(\varepsilon) \left(-\frac{\partial f(\varepsilon, \mu, T)}{\partial \varepsilon} \right) d\varepsilon \\ \Xi_{ij}^H(\varepsilon) &= \frac{1}{V N_k} \sum_{n,k} \nu_{i,nk} \tau_{nk} [\nu_{j,nk} - \Omega\, \tau_{nk}\, \nu_{j,nk}]\, \delta(\varepsilon - \varepsilon_{n,k}) \end{aligned} \tag{3.7}$$

In the absence of a magnetic field, the second term vanishes and $\Xi_{ij}^H(\varepsilon)$ reduces to the familiar transport distribution function of thermoelectric effect ($\Xi_{ij}(\varepsilon)$). Therefore, the total transport distribution function ($\Xi_{ij}^H(\varepsilon)$) can be written as the sum of the transport distribution function in the absence of a magnetic field (Ξ_{ij}) and the deviation of the transport distribution function due to a magnetic field (Ξ_{ijk}). Note that this last term contains a factor of H. Finally, the isothermal Nernst coefficient is defined as the ratio of the generated voltage along the y-axis to the temperature gradient along the x-axis under an open circuit condition ($J_x = J_y = 0$). Table. 3.1 shows the definition of each thermomagnetic response function along with their corresponding boundary conditions. Figure 3.1 shows the workflow of our code where en-

Table 3.1: Isothermal Nernst (N_T), isothermal Hall (H_T), and Ettinghausen (η) coefficients in adiabatic (A) and isothermal (T) conditions. α,ρ,κ, and π are the Seebeck coefficient, electrical resistivity, thermal conductivity, and Peltier coefficient, respectively.

Coefficient	**Measure**	**Boundary Conditions**	**Equation**
N	$\frac{\varepsilon_y}{\partial_x T}$	J=0, $\partial_y T$=0	$\alpha_{yx}(H)$
H_T	$\frac{\varepsilon_y}{J_x}$	J=J$_x$, ∇T=0	$\rho_{yx}(H)$
η	$\frac{\partial_y T}{J_x}$	J=J$_x$, Q_y=0 $\partial_x T$=0	$\frac{\pi_{yx}(H)}{\kappa_{yy}(H)}$

Table 3.2: Converged k-point meshes of wannierization and transport distribution function calculations for GaAs, Si, and ZnSe.

Material	Wannierization mesh	TDF mesh
GaAs	$8 \times 8 \times 8$	$70 \times 70 \times 70$
Si	$16 \times 16 \times 16$	$50 \times 50 \times 50$
ZnSe	$8 \times 8 \times 8$	$60 \times 60 \times 60$

ergy bands are obtained via DFT as implemented in QUANTUM ESPRESSO package [115] followed by a finer band interpolation via maximally localized Wannier functions (MLWF), as implemented in the WANNIER90 package [40]. I compute the band velocity(ν) and effective mass tensor(m) at each k-point and proceed to calculate of the transport distribution function in the presence of a magnetic field. Table 3.2 shows the wannierization mesh and k-point mesh for each case at which the transport distribution function (TDF) happened to converge. Lastly, I implement the calculation of Nernst, Hall, and Ettingshausen coefficients based on the computed Ξ.

3.1 Analytical solutions

In what follows I develop analytical solutions for several simple band structures for the purpose of comparison and validation of the DFT results. The details of some of these solutions and their interpretation are discussed in our recent work [116].

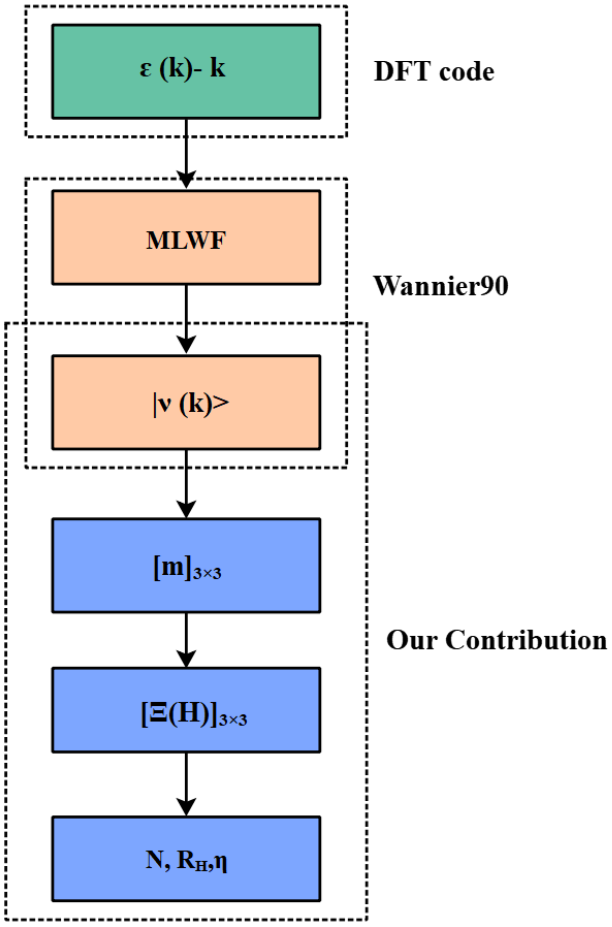

Figure 3.1: Workflow of our code to compute the Nenst(N), Hall (R_H), and Ettingshausen(η) coefficients using DFT results.

3.1.1 Single spherical band

Regardless of the energy-band type, I assume a magnetic field is externally applied only along the c-crystal axis. I begin with the simplest case which is an isotropic single-band for which the energy dispersion is described as $\varepsilon(k)=\frac{\hbar^2k^2}{2m^*}$. It can be proven that due to band symmetry, $\Xi_{ij}(\varepsilon)$ is a diagonal matrix with equal components. $\Xi_{ijk}(\varepsilon)$ contains the Ω operator which operates on velocity vectors ν_j.For a parabolic dispersion $\frac{\partial\nu_j}{\partial k_i}=\frac{\delta_{ij}\hbar}{m^*}$, on the other hand, with the assumption of the magnetic field, applied only along the c-crystal axis, It is shown in the appendix(VIII) that $\Xi_{ijk}(\varepsilon)$ has only two non-zero components as bellow:

$$\begin{aligned}\left[\Xi_{ij}^{H}\right] &= [\Xi_{ij}] + [\Xi_{ijk}] \\ &= \begin{bmatrix} \Xi_{xx} & 0 & 0 \\ 0 & \Xi_{xx} & 0 \\ 0 & 0 & \Xi_{xx} \end{bmatrix} + \begin{bmatrix} 0 & \Xi_{xyz} & 0 \\ -\Xi_{xyz} & 0 & 0 \\ 0 & 0 & 0 \end{bmatrix}\end{aligned} \tag{3.8}$$

The calculation of the distribution function Ξ for parabolic dispersion is explained in the appendix(VIII). The result is:

$$\begin{aligned}\Xi_{xx}&=\frac{2\tau q^2\varepsilon\sqrt{2m\varepsilon}}{3\hbar^3\pi^2V} \\ \Xi_{xyz}&=\frac{2q^3H_z\tau^2\varepsilon\sqrt{2\varepsilon}}{3\hbar^3\pi^2\sqrt{m}}\end{aligned} \tag{3.9}$$

Similar to the transport distribution function, response functions with two indices correspond to zero magnetic fields, and when an external magnetic field is applied response functions are shown with three indices. Each transport coefficient is calculated according to Eq. 8.4. As an example, for the isothermal Nernst coefficient($N_T(H)$) B and σ coefficients are needed.

$$\begin{aligned}\alpha_{ij}(H)&= \left[\sigma_{ij}(H)\right]^{-1}[B_{ij}(H)] \\ N(H)&= -\alpha_{yx}(H)= -\frac{\sigma_{xx}\sigma_{xyz}B_{xx}-\sigma_{xx}^2B_{xyz}}{\sigma_{xx}(\sigma_{xx}^2+\sigma_{xyz}^2)} \\ N(H)&= -\frac{\sigma_{xyz}B_{xx}-\sigma_{xx}B_{xyz}}{\sigma_{xx}^2+\sigma_{yxz}^2}\end{aligned} \tag{3.10}$$

In the appendix I show that $\sigma_{xyz}B_{xx}=\sigma_{xx}B_{xyz}$. Therefore, for a single spherical band, the Nernst coefficient is zero.

3.1.2 Multi isotropic parabolic bands

Transport distribution functions for a multi-spherical-band dispersion are similar to the case of a single isotropic band, however, each transport coefficient needs to be summed over all bands (n) e.g. σ_{ijk}=$\sum_n \sigma^n_{ijk}$. It can be mathematically proven for bands with non-equal effective mass values the Nernst coefficient will be non-zero.

3.1.3 Multi ellipsoidal bands

An anisotropic parabolic dispersion, known as ellipsoidal dispersion, looks like a parabolic dispersion but effective masses differ along each axis: $\varepsilon(k_x, k_y, k_z)$=$\frac{\hbar^2}{2}(\frac{k_x^2}{m_x} + \frac{k_y^2}{m_y} + \frac{k_z^2}{m_z})$. I utilize a scaling change of variable to transform the above dispersion to the simpler isotropic form.

$$\begin{bmatrix} k_x \\ k_y \\ k_z \end{bmatrix} = \begin{bmatrix} \sqrt{\frac{m_x}{m'}} & 0 & 0 \\ 0 & \sqrt{\frac{m_y}{m'}} & 0 \\ 0 & 0 & \sqrt{\frac{m_z}{m'}} \end{bmatrix} \begin{bmatrix} k'_x \\ k'_y \\ k'_z \end{bmatrix} \tag{3.11}$$

The dispersion relation now becomes: $\varepsilon(k'_x, k'_y, k'_z)$=$\frac{\hbar^2}{2m'}(k'^2_x + k'^2_y + k'^2_z)$. Earlier studies [114, 117] have proven for an arbitrary energy dispersion, transport distribution function may be described as $\Xi_{ii}(\varepsilon)$=$\frac{\tau q^2}{3}\nu^2_{ii}g(\varepsilon)$, where $g(\varepsilon)$ is the electronic density of states. Ξ_{ij} is still a diagonal matrix, though, having dissimilar effective mass values results in non-equal diagonal components in transport distribution function Ξ_{ii}=$\frac{\tau q^2}{3}\frac{2E}{m_i}\frac{\sqrt{2m_x m_y m_z \varepsilon}}{\pi^2\hbar^3}$. Similarly, Ξ_{ijk} keeps the previous form with only two non-zero components but with different effective masses as Ξ_{yxz}=$-\frac{q\tau H_z}{m_y}\frac{2E\tau q^2}{3m_x}\frac{\sqrt{2m_x m_y m_z \varepsilon}}{\pi^2\hbar^3}$ and Ξ_{xyz}=$\frac{q\tau H_z}{m_x}\frac{2\varepsilon\tau q^2}{3m_y}\frac{\sqrt{2m_x m_y m_z \varepsilon}}{\pi^2\hbar^3}$. Subsequently, the isothermal Nernst coefficient is obtained as:

$$N(H) = -\frac{\sigma_{xx}B_{yxz} - \sigma_{yxz}B_{xx}}{\sigma_{xx}\sigma_{yy} - \sigma_{xyz}\sigma_{yxz}} \tag{3.12}$$

3.1.4 Multi non-parabolic bands

As a more complicated case, I study a multi-non-parabolic band dispersion whose energy relation is $\varepsilon(1 + \lambda\varepsilon)$=$\frac{\hbar^2}{2}(\frac{k_x^2}{m_x} + \frac{k_y^2}{m_y} + \frac{k_z^2}{m_z})$. where λ is independent of energy. Likewise, the transport distribution function of such dispersion is calculated and followed by the isothermal

Table 3.3: Group velocity and density of states for parabolic, ellipsoidal, and non-parabolic bands. These quantities are employed to estimate the transport distribution function.

Band Dispersion	**Velocity**	**DOS**
Parabolic	$\frac{\hbar\overrightarrow{k}}{m}$	$\frac{m\sqrt{2m\varepsilon}}{\pi^2\hbar^3}$
Ellipsoidal	$\frac{\hbar\overrightarrow{k_i}}{m_i}$	$\frac{\sqrt{2m_xm_ym_z\varepsilon}}{\pi^2\hbar^3}$
Non-parabolic	$\frac{\sqrt{2m_i\varepsilon(1+\lambda\varepsilon)}}{(2\lambda\varepsilon+1)m_i}$	$\frac{(1+2\varepsilon\lambda)\sqrt{m_xm_ym_z\varepsilon(1+\lambda\varepsilon)}}{\pi^2\hbar^3\sqrt{2}}$

Nernst coefficient evaluation.

$$\begin{aligned}\Xi_{ii} &= \frac{\tau q^2}{3}\frac{\varepsilon(1+\lambda\varepsilon)}{m_i(1+2\lambda\varepsilon)}\frac{\sqrt{2m_xm_ym_z\varepsilon(1+\lambda\varepsilon)}}{\pi^2\hbar^3}\\ \Xi_{yxz} &= -\frac{\tau^2q^3H_z}{3}\frac{\varepsilon(1+\lambda\varepsilon)}{m_xm_y(1+2\lambda\varepsilon)^2}\frac{\sqrt{2m_xm_ym_z\varepsilon(1+\lambda\varepsilon)}}{\pi^2\hbar^3}\end{aligned} \tag{3.13}$$

To sum up, band-dependent quantities for each energy-wave vector dispersion relation are summarized in Table 3.3. All derivations are explained in detail in the appendix(VIII).

3.2 Results and discussion

In order to validate our code, I have chosen materials with dispersions that are to a good approximation parabolic, ellipsoidal and non-parabolic, so that DFT results can be compared with the analytical calculations obtained in section 3.1. Keeping parameters such as relaxation time, temperature, and band gap the same as in DFT, I evaluate TM transport coefficients (table. 3.4) for NaCl, GaAs, Si, and ZnSe. These materials were chosen as examples of single-spherical, multi-spherical, ellipsoidal, and non-parabolic bands, respectively. The electronic structure of each was calculated using the QUANTUM ESPRESSO package [115] followed by wannierization process [40] to successfully reproduce finer band structures through maximally-localized Wannier functions(Fig. 3.2). All calculations were carried out at room temperature and with a constant relaxation time of 10 fs and were checked to converge with respect to the interpolation mesh and the k-points mesh used for summation in the first Brillouin zone. Our contribution has been implemented in BoltzWann module [35] of the Wannier90 package. It is noteworthy to add that I have not modified any DFT code, instead, I have extended the Boltzwann capabilities to include thermomagnetic response functions. In other words, as long as the user provides the wannierized band

Table 3.4: Theoretical effective mass and non-parabolicity factor values derived from the wannierized band structures in this work.

Material	Dispersion	m_c	m_{vh}	m_{vl}	m_{vs}
NaCl	single-Isotropic	0.54	-	-	-
GaAs	Multi-Isotropic	0.067	0.14	0.497	0.075
Si	Ellipsoidal	0.73, 0.207	0.54	0.1407	0.29
ZnSe	Non-parabolic λ=0.36	0.13	1.29	0.67	0.497

structure our code could be applied to calculate thermomagnetic coefficients.

I began with the assessment of the isothermal Nernst coefficient which measures the transverse voltage in response to a longitudinal temperature gradient. The Lorentz force pushes electrons and holes to opposite sides. Therefore, the Nernst coefficient shows the maximum value in the middle of the gap where electron and hole concentrations are equal. Fig 3.3 compares the calculated isothermal Nernst coefficient to the analytical models achieved in section 3.1. Both analytical model and numerical solutions confirm that the greatest values of the isothermal Nernst coefficient is obtained for the Fermi level in the gap, and Nernst values reduce to zero as the Fermi energy moves toward band edges. The Hall effect is the transverse voltage response to an applied longitudinal current in the presence of a perpendicular magnetic field. The Hall coefficient or the transverse electrical resistivity is the voltage gradient developed per unit electric current and magnetic field. In practice, the Hall coefficient is utilized to measure the magnetic field and charge carrier density. Fig. 3.4 indicates the isothermal Hall coefficient of ZnSe computed by our code is reasonably close to the analytical results and, more importantly, follows the same trend. Lastly, the Ettingshausen effect is the production of a temperature gradient perpendicular to the plane of electric current and magnetic field [118]. For the first time, it was observed in Bismuth by Ettingshausen [119] and the effect was then named after him. Ettingshausen coefficient measures the developed temperature gradient per unit electric current, thus, it is expected to be inversely proportional to the electronic thermal conductivity. One may conclude that metals generally possess small values of the Ettingshausen coefficient which is confirmed by experiments [119]. On the other hand, since it is the response to a unit current, it is expected to reach a peak in the gap where carrier density decreases, as shown in Fig. 3.5. Some discrepancies may be noted

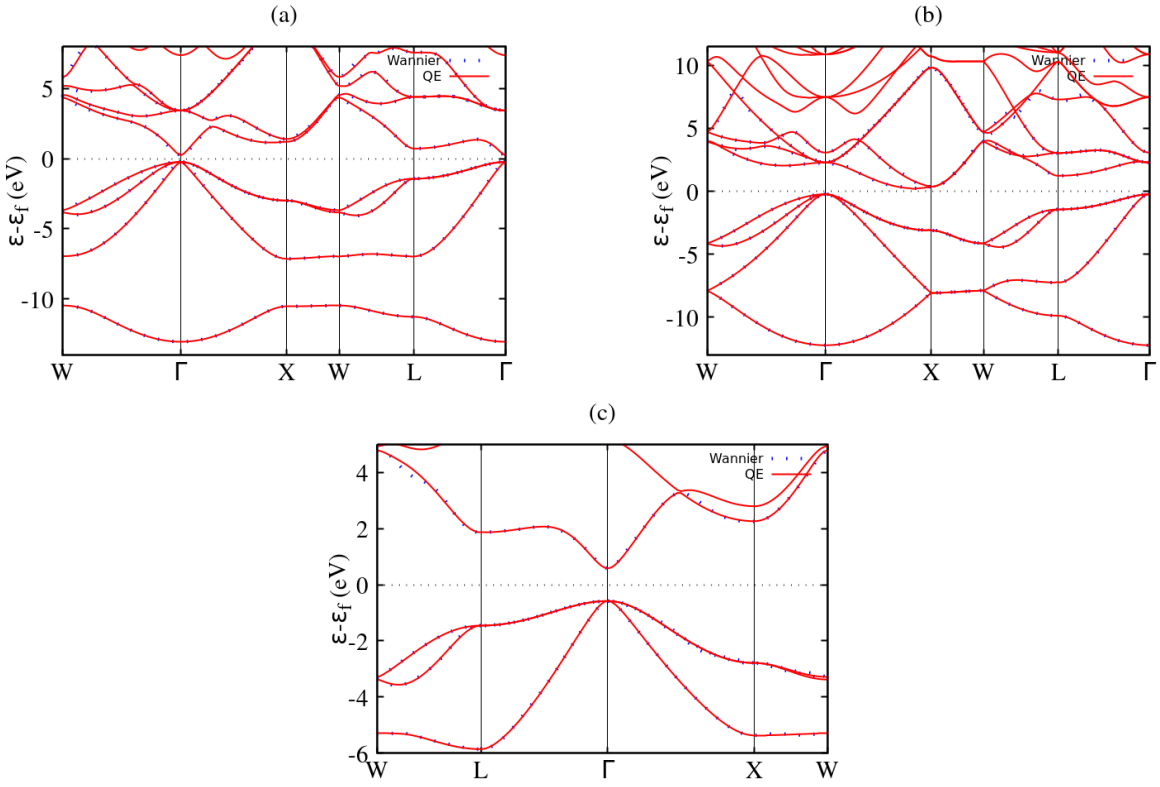

Figure 3.2: The DFT band structure (red lines) versus wannierized band structure (blue dots) of GaAs (a), Si(b), and ZnSe (c) as spherical, ellipsoidal, and non-parabolic bands, respectively.

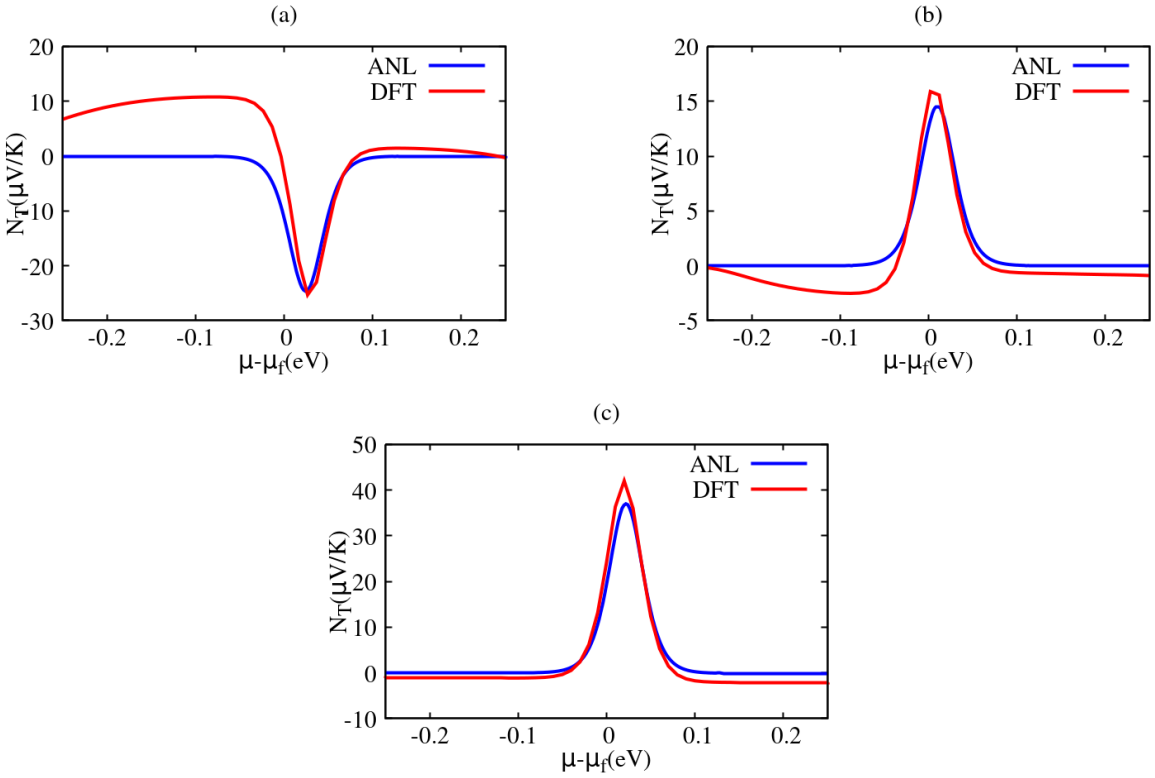

Figure 3.3: The theoretical isothermal Nernst coefficients with a constant τ of 10 fs from DFT calculations (red) and analytical models (blue) versus the chemical potential for GaAs (a), Si(b), and ZnSe (c). Zero chemical potential is fixed right in the middle of the gap.

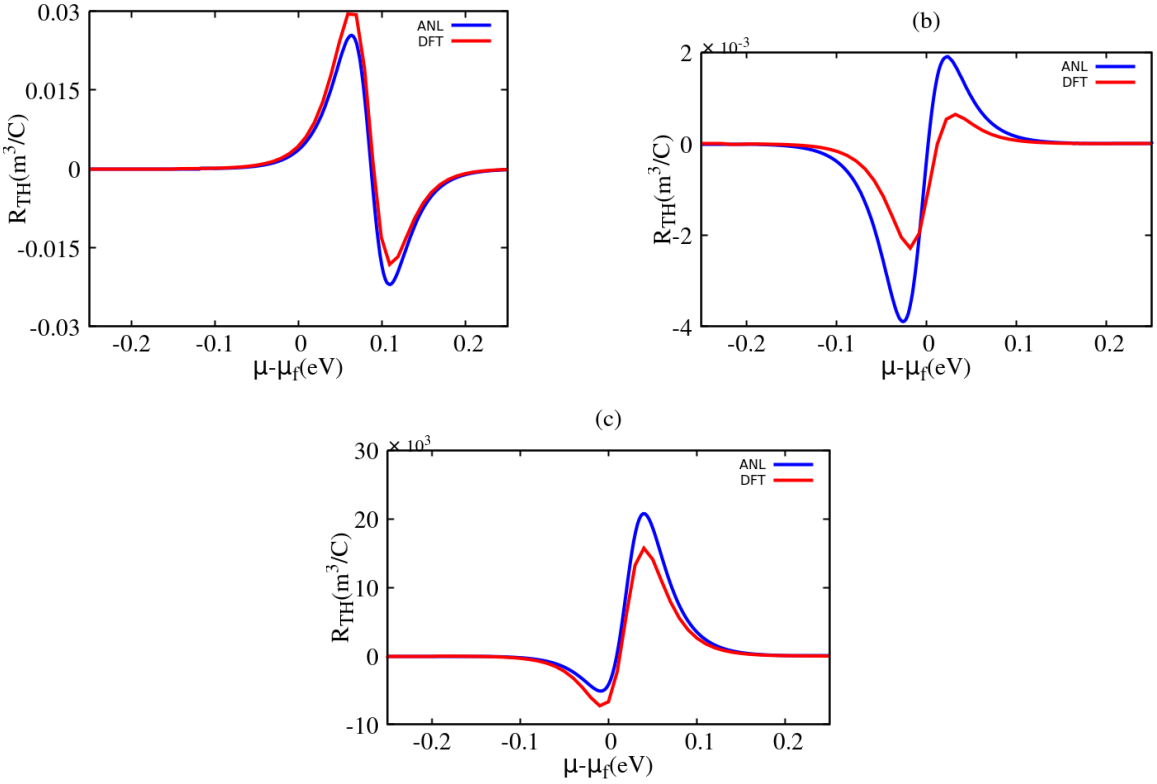

Figure 3.4: Isothermal Hall coefficients of GaAs (a), Si(b), and ZnSe (c) in SI unit (m^3/C) with a constant τ of 10 fs. DFT results (red) lie along the analytical models (blue).

between the analytical and numerical results. This may be due to the fact that over the energy window of integration, the isotropic and/or parabolic assumptions do not exactly hold for the considered materials. I have however made sure of the convergence of the transport distribution functions with respect to the number of integration k-points in the first Brillouin zone. It should also be noted that our calculations were done with a constant relaxation time, but if an energy-dependent τ model is available, it can readily be included in the code. So our results for the thermomagnetic properties should not be taken as accurate, even for GaAs, Si, NaCl, and ZnSe since their relaxation time was unknown.

3.3 Relaxation time value

So far I have assumed the constant relaxation time approximation for which any arbitrary value of relaxation time could be chosen. Within CRTA the Seebeck coefficient is entirely independent of the constant relaxation time value. Since the transport distribution function of the Nernst effect maintains a quadratic formula of the relaxation time even within CRTA the Nernst coefficient largely depends on the constant value of the relaxation time and strikingly

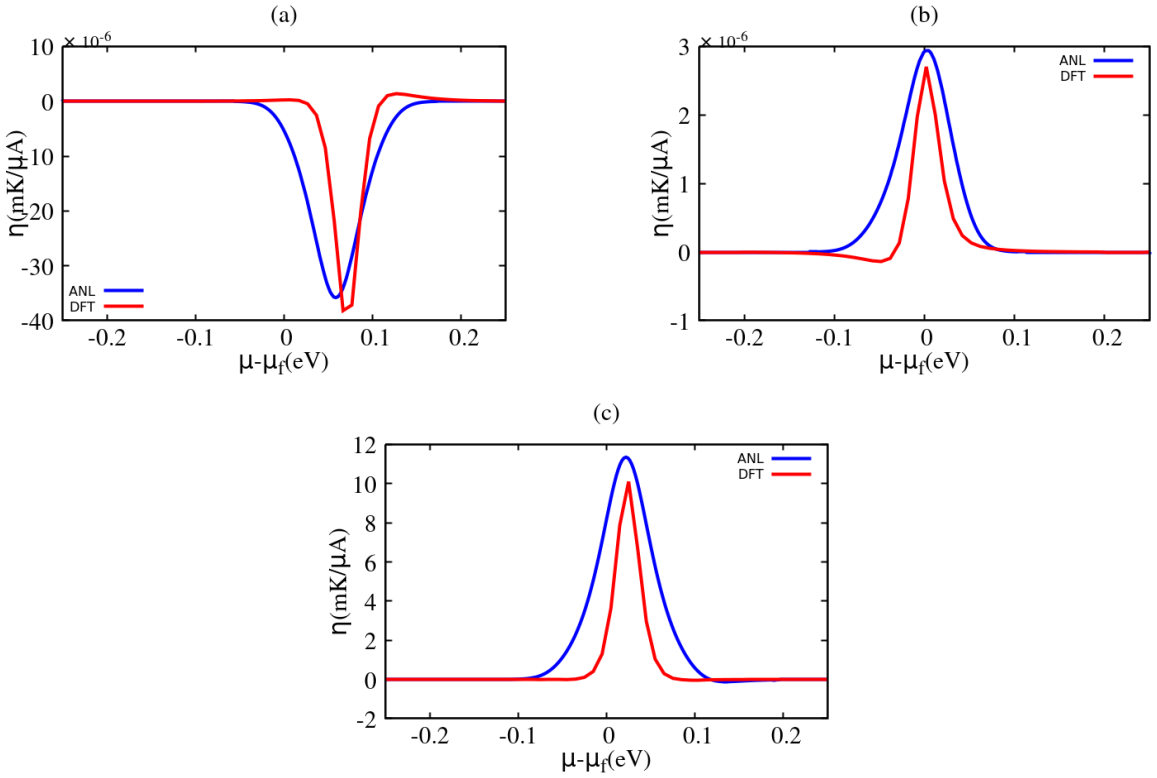

Figure 3.5: Ettingshausen coefficients (η) of GaAs (a), Si(b), and ZnSe (c), with a constant τ of 10 fs, estimated through analytical solutions (blue) confirm the validity of the DFT-aided solution (red).

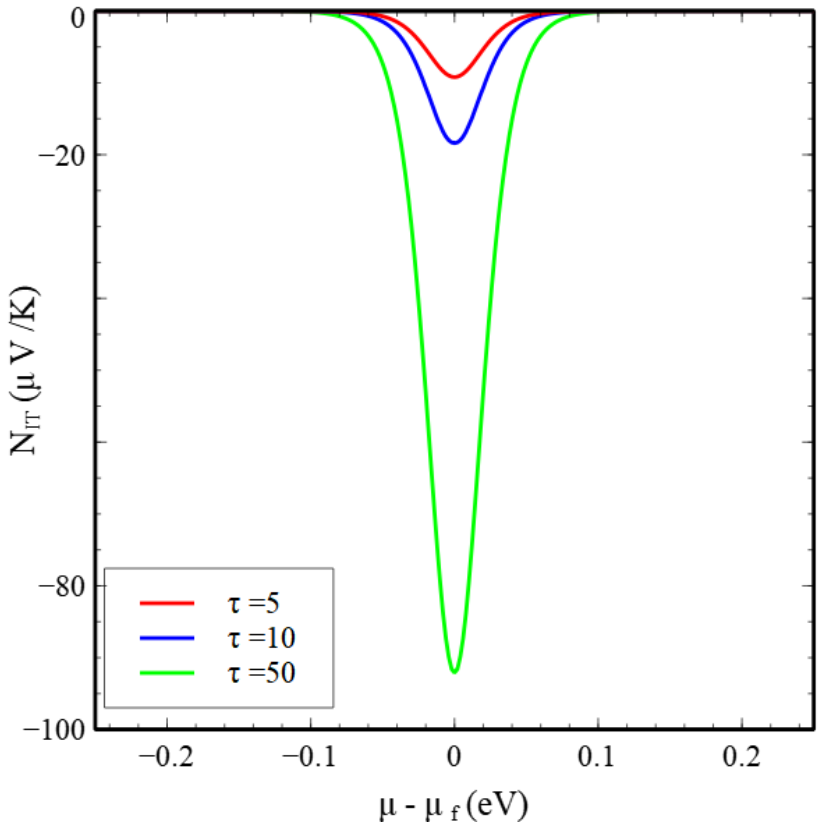

Figure 3.6: The Nernst coefficient of a two-spherical band model for various constant relaxation time values in the units of fs.

grows. Fig 3.6 portrays the Nernst coefficient for an imaginary material with two spherical bands and a band gap of 0.5 eV. One may conclude that the CRTA seems not efficiently predict the Nernst coefficient and the relaxation time needs to be taken into account.

3.4 Conclusion

In this chapter, I demonstrated a method to evaluate the Nernst, Hall, and Ettingshausen coefficients using first-principles Density Functional theory calculations. To validate the method, four types of band dispersion were considered and for each case, the thermomagnetic response functions were analytically and numerically obtained. Our first-principles DFT results were validated by comparing them with the analytical results. Our approach may be applied to all categories of materials. This method paves the road to assess the Nernst coefficient of materials and, subsequently, the thermomagnetic power factor which shows the efficiency of material for thermomagnetic energy conversion applications.

CHAPTER IV

Nernst Coefficient Beyond CRTA

4.1 Introduction

In the previous chapter III I presented a solution for the Nernst coefficient within constant relaxation time approximation, though, it is nearly impossible to reproduce the experimental data of the Nernst coefficient with a constant relaxation time since the Nernst signal depends on energy-dependent τ^2. It was shown that even within CRTA the Nernst signals drastically change versus the constant value of the relaxation time. That being the case, the constant relaxation time needs to be replaced by a robust and realistic relaxation time which largely relies on the scattering mechanisms.

Studies on the Nernst effect continued by examining semiconductors, namely, Germanium [120, 121] and InSb [122]. Germanium was the first semiconductor that showed a remarkable Nernst signal at room temperature. As of today, germanium still holds the record of the largest Nernst coefficient at room temperature. Indium antimonide also emerged as a potential candidate for the Nernst-based applications at room temperature owing to its noticeable Nernst coefficient, nearly 100 $\mu V/KT$, where T signifies Tesla. Advances in superconducting magnets facilitated the induction of strong magnetic fields. As a consequence, the Nernst effect was proposed for extended applications such as cryogenic cooling [123], thermal radiator detection [124], and thermopile systems [125].

Along with the measurements, efforts were made to model the Nernst coefficient. The earliest model was proposed by Moreau that describes the Nernst coefficient as a product of the electrical conductivity (σ), Hall coefficient (R_H), and Thompson coefficient dS/dT as $N = \frac{dS}{dT} R_H T/\rho$. Moreau's equation was derived by making multiple thermodynamics and physical assumptions but was successful in explaining the Nernst coefficient measured in several metals. For the first time, Delves [28] analytically solved the Boltzmann transport

equation (BTE) in the presence of a magnetic field for spherical bands within relaxation time approximation. With the help of the Onsager relations and heat/electric current equations he derived the Nernst, Ettingshausen, and Hall coefficients and replicated the experimental results of HgSe. Later, the Nernst coefficient was estimated using the Mott's formula [126] for $Ni_{80}Fe_{20}$ and Ni thin films and produced the trend of the experimental data [127]. Apart from the fact that the Mott formula is applicable only to metals, it was found to fall far from the experimental Nernst coefficient values of $BaFe_2As_2$ and $CaFe_2As_2$ [128]. More recently, Heremans et.al. [129] applied a semi-empirical method to support their Nernst measurement. They performed a tight-binding model of a Weyl semimetal by taking a trigonometric Hamiltonian and obtained results relatively close to the experiments in the case of NbP.

The empirical or semi-empirical models are not very accurate to be compared to experimental results unless fitting parameters are used, although can explain the trends. Besides, the effect of the electronic structure-dependent quantities such as group velocity and effective mass are oversimplified in such approaches. In our previous study [130] I presented an approach to calculate the Nernst coefficient using first-principles density functional theory within the constant relaxation time approximation. Unlike the Seebeck coefficient, the Nernst coefficient is proportional to the carrier mobility and hence is extremely sensitive to the details of the relaxation time. The constant relaxation time approximation is therefore insufficient to accurately predict the Nernst coefficient. Herein, I demonstrate a new approach to computing the Nernst coefficient including electron-phonon and ionized impurity scattering rates with the basis sets of maximally-localized Wannier functions. Our method combines the scattering rates with the Boltzmann transport equation in the presence of a magnetic field and calculates the Nernst coefficient. The Nernst coefficients of germanium, silicon, and InSb are attained at a reasonable computational cost and our theoretical results are in fairly close agreement with the experiments.

4.2 Theoretical formalism

In the previous chapter III, I showed that the Boltzmann transport equation in the presence of an external magnetic field is modified as below:

$$f_k^1 = -F_i \frac{\partial f_k^0}{\partial \varepsilon}[1 - \tau\Omega]\tau\nu_j \tag{4.1}$$

Where F is the driving force containing the gradients of chemical potential and temperatures Ω is a band operator which maintains the Lorentz force caused by the external magnetic field.

$$\Omega = \frac{q}{\hbar}\nu \times H \cdot \nabla_k = \frac{q}{\hbar}\nu_j H_k \epsilon_{ijk}\left(\frac{\partial}{\partial k_i}\right) \tag{4.2}$$

Response functions due to the magnetic field are summarized in (ij) tensor, while, the physical constants are represented in G.

$$\begin{aligned} (ij)_H &= \begin{pmatrix} \sigma_{ij}(H) \\ B_{ij}(H) \\ \rho_{ij}(H) \\ \kappa_{ij}(H) \end{pmatrix} \\ G &= \begin{pmatrix} q^2 \\ \frac{q}{T}(\varepsilon - \mu) \\ q(\varepsilon - \mu) \\ \frac{(\varepsilon-\mu)^2}{T} \end{pmatrix} \end{aligned} \tag{4.3}$$

Accordingly, the physical constants (G) and transport coefficients($(ij)_H$) are related by the transport distribution function (Ξ^H) in the presence of a magnetic field.

$$\Big[N(H)\Big] = \Big[\sigma(H)\Big]^{-1}\Big[B(H)\Big] \tag{4.4}$$

And the Nernst coefficient is identified as $N_T = N_{yx}(H)$.In Eq. 4.2, the Ω operates on both relaxation time (τ) and band velocity (ν) in which the derivative can be taken part by part.

$$\begin{aligned}\Omega(\tau\nu)&=\frac{q}{\hbar}\nu\times H\cdot\nabla_k=\frac{q}{\hbar}\nu_j H_k\epsilon_{ijk}\left(\frac{\partial\tau\nu}{\partial k_i}\right)\\&=\frac{q}{\hbar}\nu_j H_k\epsilon_{ijk}\left(\tau\frac{\partial\nu}{\partial k_i}+\nu\frac{\partial\tau}{\partial k_i}\right)\end{aligned}\tag{4.5}$$

Relaxation time is implemented for each band at a given k-point($\tau(n,k)$), though, it could be easily transformed into energy space by $\tau(\varepsilon)=\sum_{n,k}\tau(n,k)\delta(\varepsilon-\varepsilon_{n,k})/\sum_{n,k}\delta(\varepsilon-\varepsilon_{n,k})$. Such that energy-dependent relaxation time will be placed in Eq. 4.5.

$$\begin{aligned}\Omega(\tau\nu)&=\frac{q}{\hbar}\tau(\varepsilon)\nu_j H_k\epsilon_{ijk}\left(\frac{\partial\nu}{\partial k_i}+\nu\frac{\partial\tau(\varepsilon)}{\partial\varepsilon}\frac{\partial\varepsilon}{\partial k_i}\right)\\&=\frac{q}{\hbar}\tau(\varepsilon)\nu_j H_k\epsilon_{ijk}\left(\frac{\partial\nu}{\partial k_i}+\nu\frac{\partial\tau(\varepsilon)}{\partial\varepsilon}\hbar\nu_i\right)\end{aligned}\tag{4.6}$$

$\nu\times H$ is perpendicular to ν and hence its dot product by ν is zero, therefore, $\nu_j H_k\epsilon_{ijk}\nu\frac{\partial\tau(\varepsilon)}{\partial\varepsilon}\hbar\nu_i=0$, and the derivative of relaxation time in Eq. 4.6 is omitted. The transport distribution function may be stated with the energy-dependent relaxation time.

$$\Xi_{ij}^{H}(\varepsilon)=\frac{1}{VN_k}\sum_{n,k}\nu_{i,nk}\tau(\varepsilon)[\nu_{j,nk}-\Omega\,\tau(\varepsilon)\,\nu_{j,nk}]\,\delta(\varepsilon-\varepsilon_{n,k})\tag{4.7}$$

The workflow of our approach is displayed in Fig. 4.1. I start with the electronic structure obtained from DFT codes. The maximally localized wannier functions [40] (MLWF) are required to represent a fine interpolation of electron energy dispersion followed by the derivation of band velocity and effective mass tensors. Several post-processing packages were developed to compute the scattering rates [131–134], among those I choose the AMSET code [134] in which not only electron-phonon collisions are taken into account, but it also evaluates ionized impurity scattering. Charge carrier relaxation times are achieved by AMSET code [134] and transformed into energy space. Relaxation times are then coupled with band-dependent quantities to compute the transport distribution function. Input parameters of all steps (DFT, wannierization, and AMSET) for each material are provided in the appendix. Now that the formalism has been clarified (for more details reference [116] can be consulted), I will proceed to give the details of the first-principles calculations, display and discuss the results in comparison with experimental results.

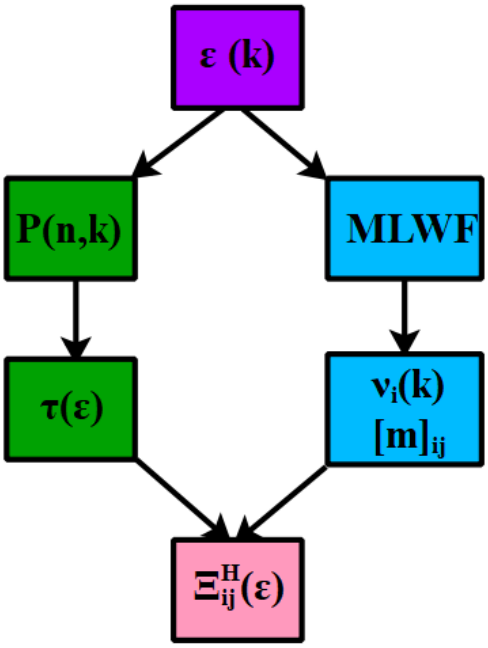

Figure 4.1: The workflow used in this work to calculate the Nernst coefficient. Wannier functions, group velocity, and effective mass tensor (blue boxes) come from the Wannier90 package. Scattering rates (P) and relaxation times are taken from AMSET code (green boxes). I couple the output of the two codes to obtain the total transport distribution function (Ξ).

4.3 First-principles calculations

Vienna ab initio simulation package (VASP) was employed to conduct the first-principles density functional theory calculations based on plane wave self-consistent field (PWscf) and projector-augmented waves pseudopotential [135] method as treated in the generalized gradient approximation [136]. Monkhorst–Pack scheme was used to sample the Brillouin zone. DFT input parameters of this article are summarized in table 4.1. It is noteworthy to add that the PBE exchange-correlation functional yielded a zero gap and nearly linear dispersion around the Gamma point in the conduction bands for Ge and InSb. That is to say, the electronic structures were calculated using the mBJ exchange-correlation type.

The electronic structures were then wannierized in order to have a finer band interpolation via maximally localized Wannier functions (MLWF), as implemented in the Wannier90 package [40] (table 4.2). Due to the calculation of the effective mass tensor, the Nernst effect transport distribution function (Ξ) is expected to converge at finer k-mesh values rather than the Seebeck effect. All the integrals discussed in Section 4.2 were performed in the

reciprocal space on fine MLWFs. The physical properties of each material for scattering rates were taken from the experiments and the total scattering rate is summed over all the mechanisms according to Matthiessen's rule [137]. A wide range of values has been reported for some physical properties e.g. deformation potential, whether in experiments or theory, and It has to be made clear that I selected the deformation potentials that bear the best fit to the experiments(see table 4.3). Table4.3 shows the physical parameters used to calculate the mobility of each material. Lastly, after convergence was assured, the isothermal Nernst coefficient was computed and compared to the experiments.

Table 4.1: Parameters used in DFT calculations.

Material	cutoff energy (eV)	k-mesh	Lattice constant (Å)
Ge	500	12×12 × 12	5.657
Si	550	12×12 × 12	5.429
InSb	500	12×12 × 12	6.479

Table 4.2: Parameters used for wannierization.

Material	# of wannierized bands	wannierization k-mesh	Ξ k-mesh	convergence tolerance
Ge	8	6×6 × 6	300	10^{-8}
Si	8	12×12 × 12	200	10^{-8}
InSb	8	6×6 × 6	300	10^{-8}

4.4 Results and discussion

The band structure for each material was plotted along high symmetry k-points (Fig 4.2- 4.4). I continued the procedure with the mBJ electronic structures and the conduction bands were shifted to reproduce the experimental band gap for calculation of the transport distribution function and relaxation time. The experimental mobility was replicated for each sample in a range of temperatures as well as doping concentration(Fig 4.5- 4.7).

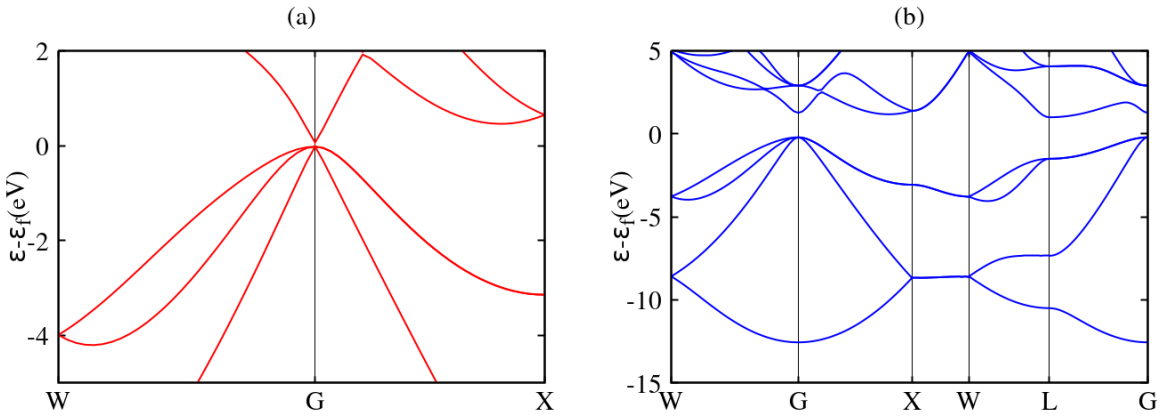

Figure 4.2: Band structure of Germanium with PBE (a) and mBJ (b) XC-functional.Ge is a direct band gap semiconductor.

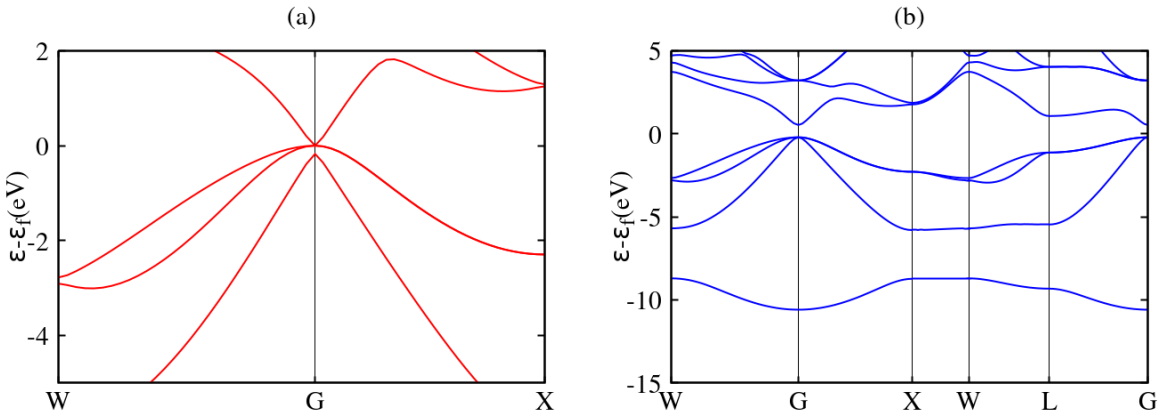

Figure 4.3: Band structure of InSb with PBE (a) and mBJ (b) XC-functional. Top of valence band and bottom of conduction band happen at G-point.

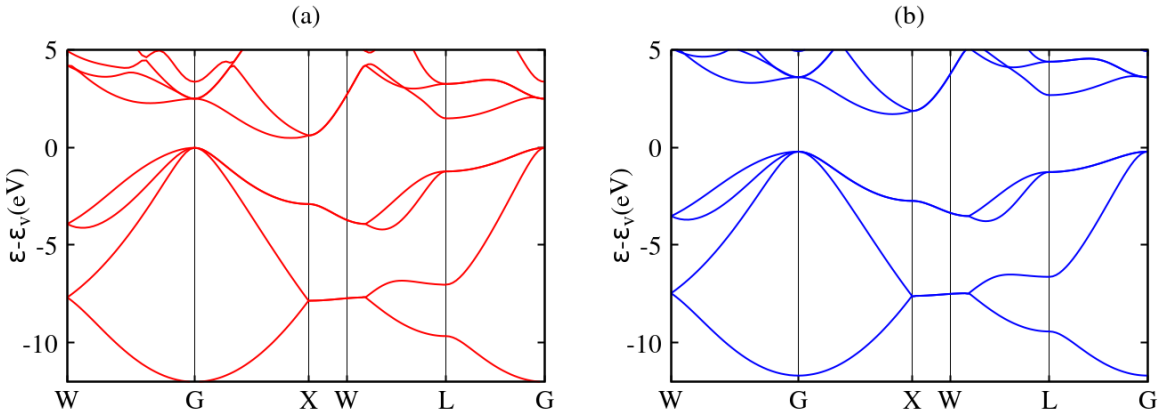

Figure 4.4: Band structure of Silicon which is an indirect band gap semiconductor calculated using PBE (a) and mBJ (b) functionals. Top of valence band is the G point while the conduction band minimum is along the GX direction.

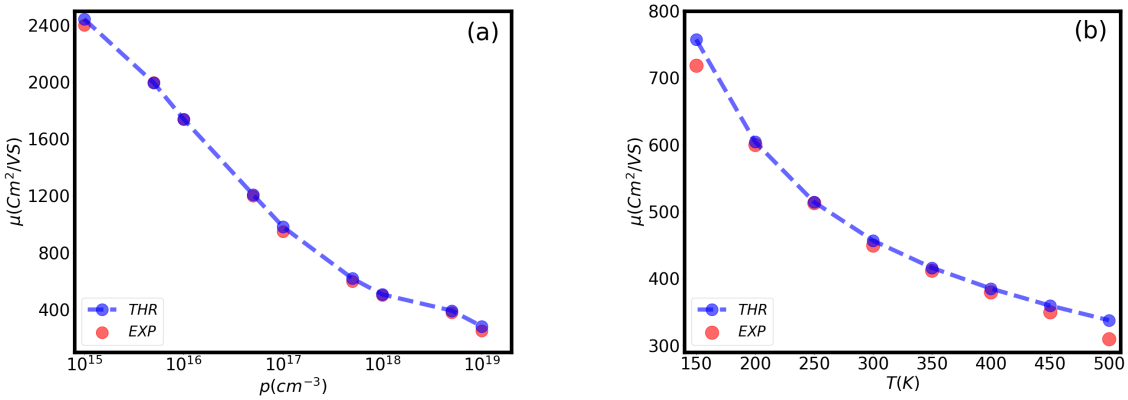

Figure 4.5: Hole mobility for Germanium at room temperate versus doping concentration (a) and versus temperature for a constant carrier concentration of $4.9 \times 10^{18} Cm^{-3}$. Red circles and blue dashed lines indicate experimental [145] and theoretical data, respectively.

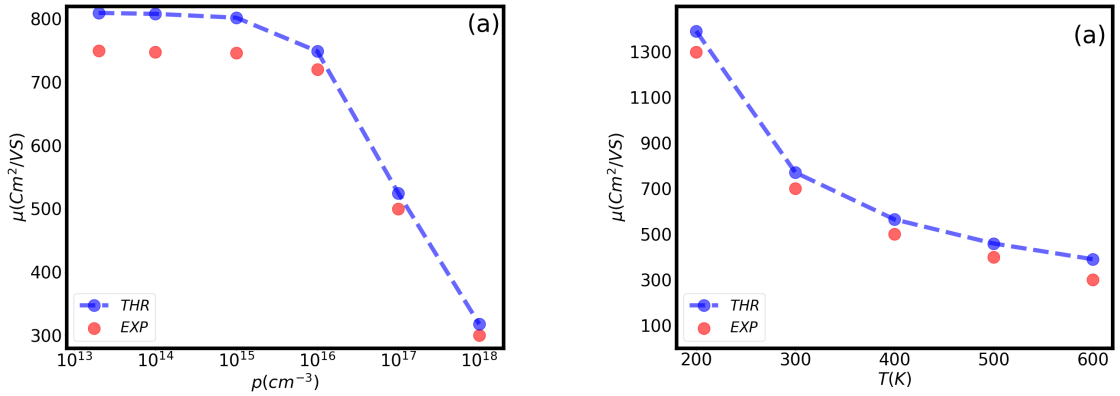

Figure 4.6: Hole mobility of InSb versus carrier concentration at 290 K (a). Hole mobility of InSb versus temperature for hole concentration of $1.8 \cdot 10^{14} Cm^{-3}$ [146, 147].

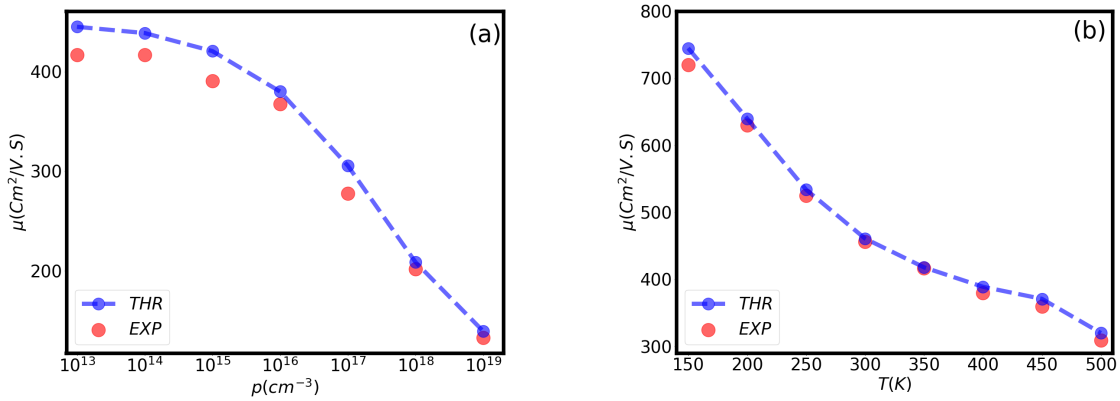

Figure 4.7: Hole mobility of Si at 300 K versus hole concentration (a). Hole mobility of Si for hole concentration of $2 \cdot 10^{17} Cm^{-3}$ versus temperature [148, 149].

Table 4.3: Physical properties of materials including shifted band gap, deformation potential, phonon frequency, bulk modulus, dielectric constant, and piezoelectric constant taken from literature[138–144] .

Material	$E_g^{exp}(eV)$	$E_g^{mBJ}(eV)$	$\mathcal{D}_A^v$(eV)	$\mathcal{D}_A^c$(eV)	ν_{op}(THz)	$\mathcal{C}(GPa)$	ϵ_r	$d_{pz}(C/m^2)$
Ge	0.66	1.47	0.85	0.95	8.94	75	16.2	0.0
Si	1.12	1.91	0.9	1.5	15.2	202	11.68	0.0
InSb	0.16	0.73	1.9	2.0	6.04	46.6	16.8	0.07

4.4.1 Germanium

Germanium in its single crystal form is one of the first semiconductors in which the Nernst signal was reported and in fact, it holds the record for the largest Nernst coefficient around room temperature. Therefore, I chose to test our method on Ge. Electrical properties including mobility, electrical resistivity, Seebeck coefficient, and indeed Nernst coefficient largely depend on the scattering rates, thus, the scattering rates and the mobility need to be validated. Fig. 4.5.a depicts the hole mobility of single crystal Germanium versus doping concentration at room temperature. Fig. 4.5.b shows the same quantity versus temperature for a hole concentration of $4.9 \times 10^{18} cm^{-3}$. As temperature increases, the population of phonons increases leading to an increase in the electron-phonon scattering rates and a decrease in electron mobility. The acoustic deformation potential scattering and the ionized impurity scatterings are the dominant scattering mechanism in this material and the combination of the two can reproduce the experimental data closely. This fact was also previously reported in the literature [150]. Our theoretical results for Ge are found to be within less than 5% of the experiments. A wide range of values has been reported for the deformation potential, whether in experiments or theory. Therefore, here I selected the deformation potentials that best fit the experiments.

The Nernst coefficient of single crystal Ge was measured to be as large as 350 $\mu V/KT$ around room temperature [120]. Yamaguchi [121] also observed extremely large values of the Nernst coefficient for Ge, but they failed to replicate their measurements by a parabolic band model. In this work, I calculate the Nernst coefficient of Ge in a wide range of

temperatures using density functional theory.

After the successful replication of Ge mobility (Fig 4.5), I proceeded with the same physical parameters used to establish the scattering rates. It was then followed by substituting the resulted scattering rates into the transport distribution function (Eq. 4.7) and, finally, evaluation of the Nernst coefficient (Eq. 4.4). Fig. 4.8 shows our theory can accurately predict the experimental Nernst coefficient for Ge in a wide range of temperatures and for various doping concentrations. For a slightly doped sample ($\rho = 30\Omega.cm$) the Nernst coefficient continuously decreases versus temperature, though, it decreases less rapidly at high temperatures. The corresponding chemical potential of the electrical resistivity of $\rho = 30\Omega.Cm$ is 240 meV below the intrinsic Fermi level. Since for these specific samples it was not reported how resistance changes with temperature experimentally, I performed our modeling under constant chemical potential conditions. The dominant carriers are holes. However, the concentration of both electrons and holes increases with the rise in temperature as shown in Fig. 4.9a. The carrier mobility as shown in Fig. 4.9b drops as temperature increases. Various models (see Moreau's equation for example) have shown that the Nernst coefficient is proportional to carrier mobility. In this case, I also observe that the Nernst coefficient follows the carrier mobility trend and decreases with temperature.

Comparing the two samples, the sample with larger mobility also exhibits a larger Nernst coefficient. The trend of the Nernst coefficient with respect to temperature is different in the case of the low-resistance sample. Here, as shown in Fig. 4.8, the Nernst coefficient reaches a maximum value at around 410 K both in theory and experiments. To explain this maximum in the Nernst coefficient, I have plotted the Seebeck coefficient of the two samples in Fig. 4.9C. In the case of the low-resistance sample, there is a large drop in the Seebeck coefficient vs. temperature at around 400 K which can be in turn attributed to the increase in the population of minority carriers. The Nernst coefficient is proportional to the slope of the Seebeck coefficient with respect to temperature (represented by the Thomson coefficient) within Moreau's relation. In this case, the maximum of the Nernst coefficient happens where the Thomson coefficient is the maximum. I emphasize that Moreau's relation can only qualitatively explain the results and it is not in quantitative agreement with our first-principles model. An alternative explanation is to correlate this maximum to the Seebeck coefficient of the minority carriers. It has been shown that the Nernst coefficient within

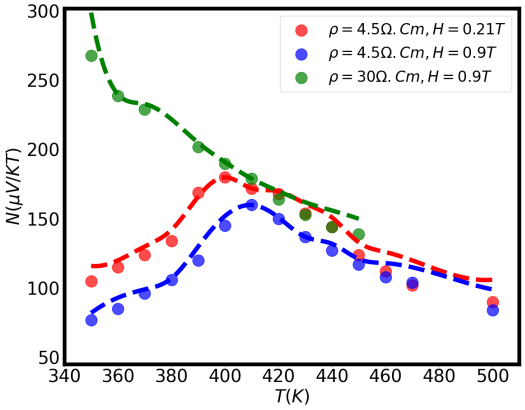

Figure 4.8: Nernst coefficient of Germanium versus temperature. Solid circles are the experimental data from literature [120] and our theoretical predictions are shown by lines in the corresponding color for each case. Samples possess different electrical resistivity (ρ) and are under magnetic fields (H) of 0.21 T and 0.9 T.

constant relaxation time approximation and within parabolic bands, comes only from the cross-term correlating between the valence and conduction bands and is proportional to the Seebeck coefficient of the minority carriers. (See Eq 45 of Ref. [116]). The 400 K is where the minority carriers start to contribute and have a finite and large Seebeck coefficient.

Our findings are normalized to the magnetic field in the units of ($\frac{\mu V}{KT}$) and the Nernst signals appeared to be larger in the smaller magnetic field of 0.21 T compared to 0.9 T whether in experiments or theory (Fig. 4.8). The total distribution function of the Nernst effect is a two-term equation(Eq. 4.7) whose first term is greater and independent of the magnetic field. In an oversimplified model, $N = \alpha + \beta H$ where $\alpha \gg \beta$. It can be mathematically proved that N/H would be larger for smaller magnetic fields. Fig. 4.8 unveils that the Nernst coefficient reaches a maximum value at around 410 ^{0}K both in theory and experiments. Furthermore, Fig 4.9 (a) exhibits that the hole mobility of the lighter doped sample is larger, such that greater Nernst coefficient values are observed for that sample. Although, as temperature goes up the discrepancy between mobilities dwindles which leads to comparable Nernst signals for both samples. Electron and hole concentrations surge at higher temperatures (Fig 4.9(b)).

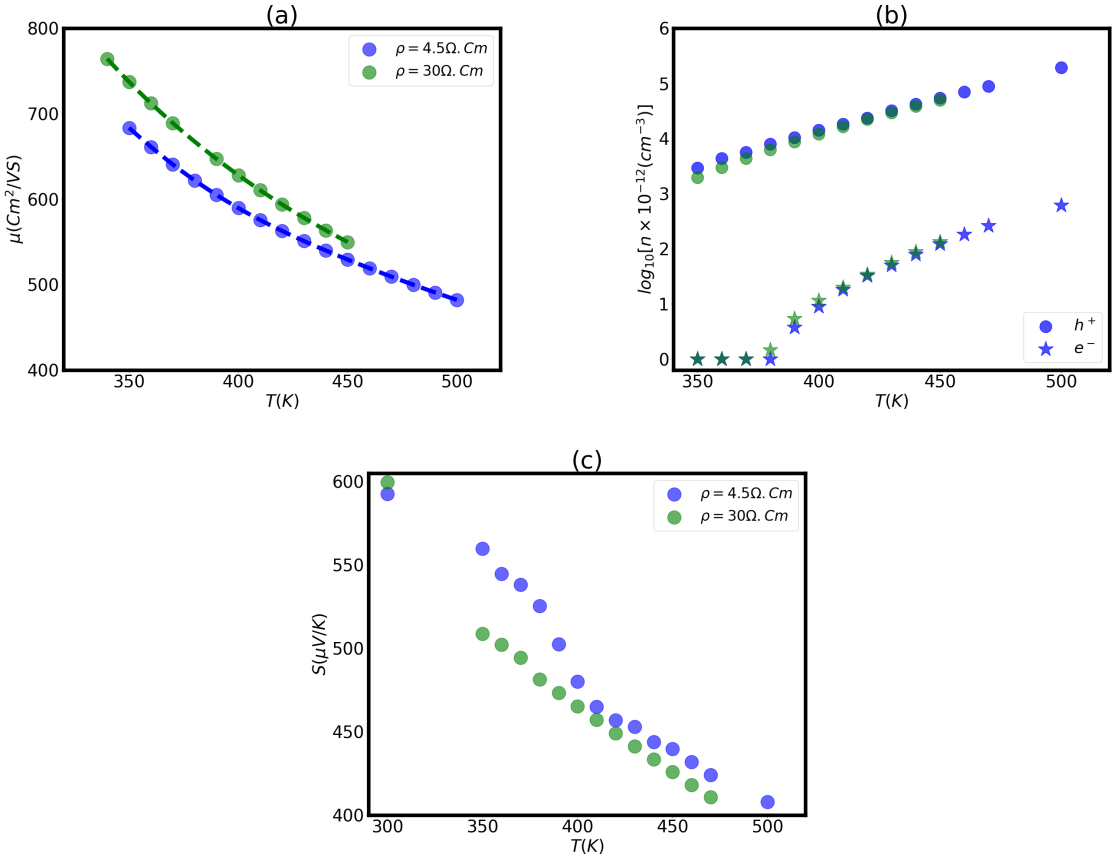

Figure 4.9: (a) Hole and electron concentrations of Germanium with the electrical resistivity of 4.5 $\Omega.cm$ (red) and 30 $\Omega.cm$ (green) versus temperature. Carrier mobility (b) and Seebeck coefficient (c) for the same samples versus temperature.

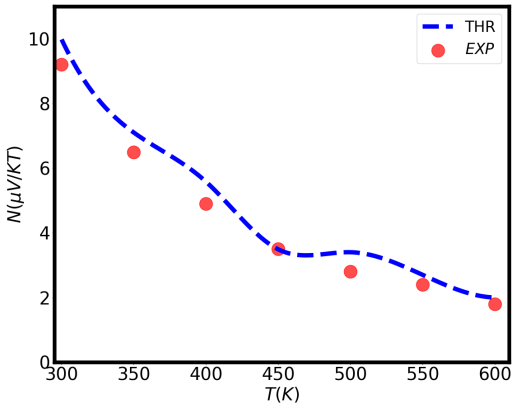

Figure 4.10: Nernst coefficient of p-type Silicon at elevated temperatures under a magnetic field of 0.9 Tesla. Our theory (blue dashed line) is in agreement with the experimental data (red circles) [151].

4.4.2 Silicon

Inspired by large Nernst signals of germanium, silicon was thought to show large Nernst signals due to similarities with germanium. Mette continued his work on the Nernst effect and chose silicon, however, the Nernst coefficient in silicon is significantly smaller [151]. It originates from a larger band gap of silicon (1.12 eV versus 0.66 eV in Ge). The band gap in silicon is so wide that the charge carriers would be negligible far from the band edges, hence, the Nernst signal will vanish deep in the gap. Instead, peak values are expected to appear in the band edges due to maximum relaxation time, however, effective mass values of Si are not small, then even at the band edges, minor peaks are anticipated. It is worth saying that in order to achieve the electrical resistivity of 0.22Ω.cm in p-type silicon it needs to be doped as much as $3 \times 10^{18} cm^{-3}$ that has to take place inside the valence band.

4.4.3 InSb

Indium antimonide is a narrow gap semiconductor widely used in semiconductor applications e.g. transistors, magnetic field sensors, and infrared cameras [152–154]. InSb was among the earliest semiconductors that showed relatively large Nernst signals at room temperature. El-saden et.al [155] reported the Nernst effect in InSb for the first time in the temperature range from 260 to 340 ^{0}K and applying magnetic fields from 0.4 to 1.2 T. They used a measurement method similar to what Lindberg [156] employed for Hall measurement.

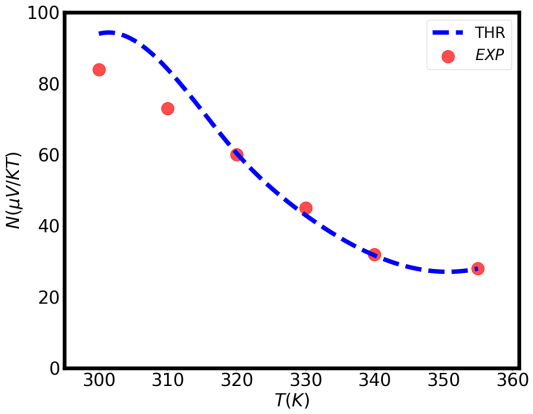

Figure 4.11: Nernst coefficient of p-doped Indium antimonide in a range of temperature and a 4 Tesla magnetic field. Red circles are the measurements from Ref [122] and values obtained by our approach are shown by the blue dashed line.

The length of the sample had to be kept at least three times larger than its width in order to avoid the shorting effect of the end electrodes. Decades later, Nakamura [157] carried out thorough measurements of thermoelectric as well as thermomagnetic properties on bridged shape InSb samples and recorded Nernst coefficient values as big as 80 $\mu V/KT$, however, his phenomenological models deviate from the experiments. I performed DFT-based calculations of the Nernst coefficient and found fairly close values to the experiments for a p-type InSb whose electrical conductivity is $2.2\times10^4 S/m$ under a magnetic field of 4 T.

Although the hole mobility of InSb is larger than Ge, the chemical potential which yields the electrical conductivity of $2.2\times10^4 S/m$ is in the vicinity of the valence band edge. For a large Nernst signal in semiconductors, minimum coexistence of electrons and holes is needed. The chemical potential that bears the minimum coexistence of the opposite charges occurs at the intrinsic Fermi level. Considering the fact that the product of electron concentration and hole concentration is constant in equilibrium, as the chemical potential moves toward either bands, the total concentration of electrons and holes grows and the Nernst signals shrink due to higher carrier concentration. Moreover, InSb is a narrow gap semiconductor (0.16 eV) such that at even room temperature the intrinsic electron and hole concentrations are substantial, thereby, a lower Nernst coefficient in comparison with Ge is expected.

Having the density of states from DFT and the Fermi-Dirac distribution function I can calculate the electron and hole carrier concentration at a given temperature and a chemical poten-

tial. At the intrinsic Fermi level electron concentration equals hole concentration. Table 4.4 summarizes the hole concentration for InSb, Ge, and Si samples studied in this work.

Table 4.4: Hole concentration at 300 ^{0} K for p-type InSb, Ge, and Si samples studied in this work.

Material	Hole concentration (cm^{-3})	$\rho(\Omega.cm)$
InSb	1.16×10^{17}	4.5×10^{-5}
Ge	1.2×10^{15}	30.00
Ge	2.8×10^{15}	4.5
Si	8×10^{16}	0.22

4.4.4 Bismuth

Bismuth is a well-known semimetal for unique quantum features including giant oscillatory magnetostriction, magnetoresistance, Shubnikov–de Hass effect, and de Hass–van Alphen effect [158]. The effect of applied magnetic field on the transport properties of bismuth has caught attention for the last decades. The electrical resistivity of bismuth may be improved 10^6 times larger upon applying a magnetic field. The semi-classical transport theory is unable to explain the quasilinear magneto-resistance in bismuth and it was unveiled by quantum mechanics [159].

The mean-free path of bismuth at 300 K was found to be 2 μm [160], which is a hundred times greater than that of copper. Due to low carrier concentration, the quantum limit in bismuth may be reached by a magnetic field of 9 T along the c-axis. In that limit, electrons will be moved to the lowest Landau level, and the Fermi wavelength will turn larger than the magnetic length (the radius of the lowest-energy quantized isolated electron orbit in a magnetic field), as a result, massive quantum oscillations of the Nernst coefficient was observed [158].

Specifically, the Nernst effect was discovered in Bismuth. The bismuth crystal structure is rhombohedral that is transformed from the high symmetry cubic structure by a distortion along the diagonal, thus, a small portion of the Brillouin zone is occupied by the Fermi

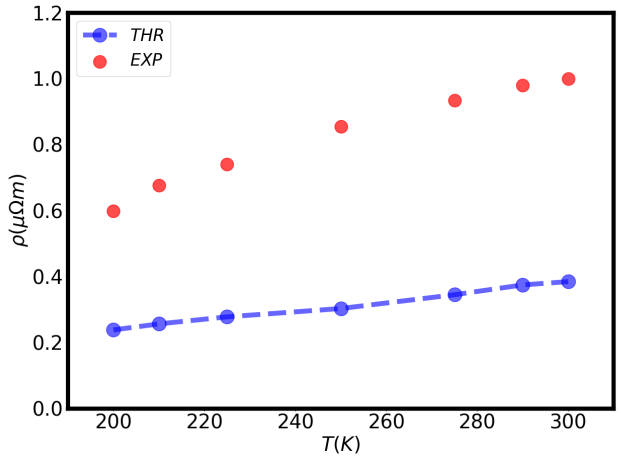

Figure 4.12: Electrical resistivity of polycrystalline bismuth below room temperature. Our theoretical results (blue dashed line) slightly deviate from the experiments [163].

surface. Relatively low carrier concentration accompanied by small effective masses makes bismuth ideal for the Nernst-Ettingshausen cooling systems. The largest Nernst coefficient has been observed in a bismuth single crystal at the temperature of 4 K about 1 mV/KT [161]. Carrier mobility in bismuth was reported to be in the order of 10^4 cm^2/Vs whether for the bulk system or in nanowires [162]. Notably, even polycrystalline bismuth shows considerable Nernst signals at room temperature. Hasegawa et.al. measured the electrical resistivity and Nernst coefficient of the polycrystalline bismuth. Similar to the single crystal, the electrical resistivity of the polycrystalline samples was fairly small (in the order of $\mu\Omega m$) and the Nernst coefficient was about 20 $\mu V/KT$ in the presence of a magnetic field of 0.2 T.

I reproduced the electrical resistivity of the polycrystalline bismuth in temperatures between 200 K and 300 K (see Fig). In addition to acoustic phonon deformation potential, the grain boundary scattering rate was estimated as $\frac{1}{\tau_{GB}} = \frac{\nu}{d}$ where d is the grain size which was reported to be several microns. Consequently, the grain boundary scattering rate was far smaller compared to the electron-phonon scattering rate, and more specifically, the acoustic phonon deformation potential was found to be the dominant mechanism which is consistent with the previous studies [162, 163]. It needs to be emphasized that since bismuth is a semimetal I considered a pure polycrystalline bismuth in which acoustic phonon deformation potential and grain boundary scatterings were taken into account. The band gap of bismuth is zero and a single value of D=3.6 eV, obtained from DFT calculations, was used in the calculations. I then continued to the calculation of the Nernst coefficient. Fig 4.13 shows that our DFT

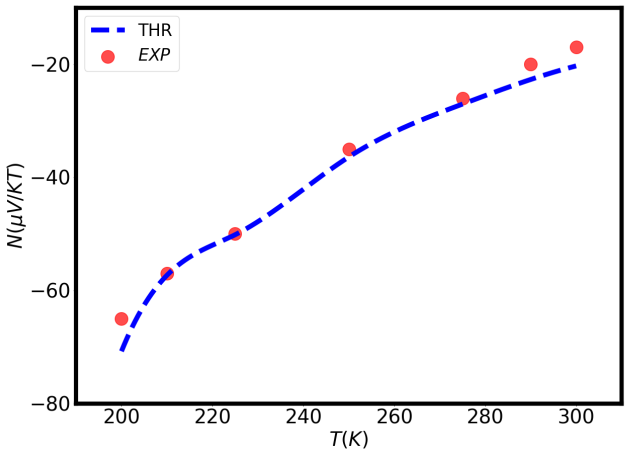

Figure 4.13: Nernst coefficient of polycrystalline bismuth below room temperature and under a magnetic field of 0.2 T. Our theory (blue dashed line) predicts the experiments [163] (red circles).

results agree with the experimental data in a wide range of temperatures. The Nernst coefficient of bismuth at room temperature is strikingly smaller than the cryogenic conditions. Furthermore, as the temperature decreases the Nernst coefficient magnitude increases due to growth in mobility.

4.5 Computational aspects

A significant endeavor was allocated to code optimization in terms of parallelization and memory usage. External libraries that I used are open-source codes, namely, Linear Algebra PACKage (LAPACK) and Basic Linear Algebra Subprograms (BLAS). By Switching from GFortran compiler to ifort compiler, I managed to speed up the code as much as 330%, while the numerical results change no more than 8%. Therefore, I strongly suggest the user to compile the code with Intel Fortran Compiler (ifort) which surpasses Gfortran weather for the Seebeck, scattering rates, and the Nernst calculations. (Fig. 4.14).

Computation of the Nernst coefficient within RTA is carried out by a post-processing code which requires a hierarchical procedure shown in Fig 4.1. Fig. 4.15 exhibits the computation time for each procedure in the case of Ge. Evaluation of the transport distribution function takes longer as $\frac{\partial \nu}{\partial k}$ is assessed at a sufficiently dense grid ($300 \times 300 \times 300$ in this case). It should be noted that the transport distribution function of the Nernst effect happens to converge at denser grids compared to the Seebeck coefficient. Coupling the TDF and relaxation

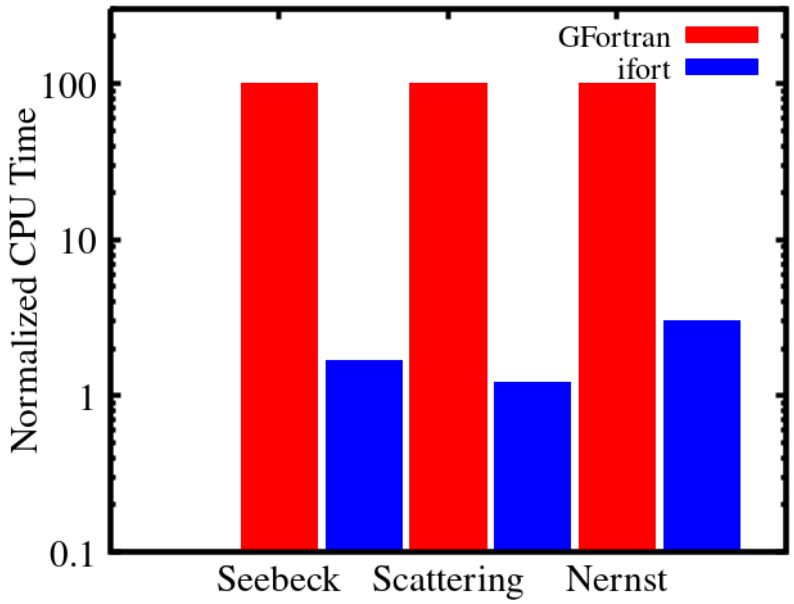

Figure 4.14: Dramatic improvement of the CPU time by ifort compiler.

times, which results in the Nernst coefficient, is carried out on one single node that might take a considerable amount of time depending on scattering mechanisms, temperature, and doping concentration. It is notable that for each temperature and doping concentration the relaxation time has to be appraised. As an example, Fig. 4.15 was plotted for 18 temperature points, 3 doping concentrations, 3 scattering mechanisms, and 2 magnetic fields.

4.6 Material descriptors for the Nernst coefficient

Materials discovery and high-throughput calculations are ubiquitous in the realm of computational materials science. Direct calculations of the Nernst effect could be computationally heavy as time-consuming tensor operations are required. Herein, a semi-empirical approach based on analytical models is presented to expedite the evaluation of the Nernst coefficient. Within relaxation time approximation, I adopt a model to simulate charge transport in the presence of an external magnetic field followed by finding the parameters that optimize the Nernst coefficient.

4.6.1 Model

I consider a two-spherical band model for which the transport distribution function was derived in chapter III. For parabolic bands, scattering rate equations can be simplified and

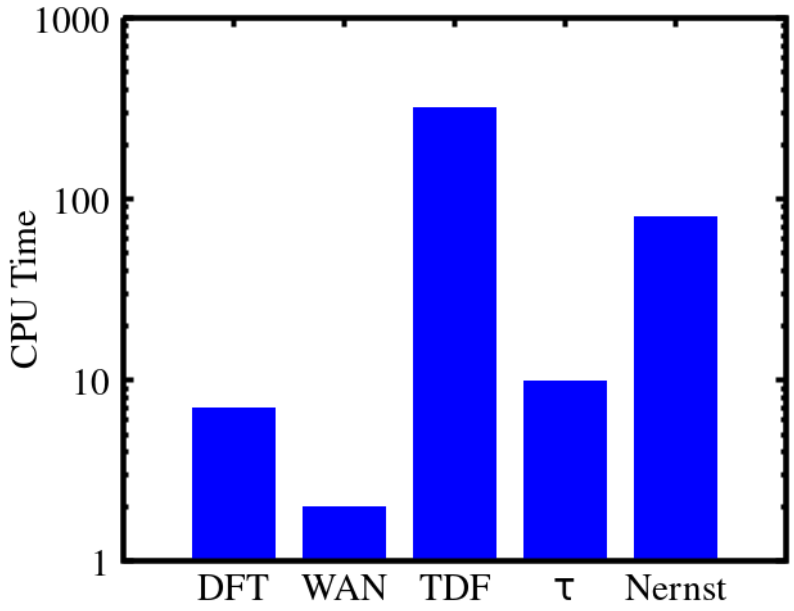

Figure 4.15: CPU time of sequential procedures for Ge: band structure calculation, Wannierization, transport distribution function, relaxation time, and the Nernst coefficient calculation. DFT, WAN, and TDF parts were carried out in a parallel run on 4 nodes.

formulated as a function of energy [164]. Within this frame, I scrutinize the effects of band structure and scattering parameters on the Nernst coefficient. In order to simplify the scattering rates, an intrinsic single-atom system was assumed in which the dominant scattering mechanism is acoustic deformation potential (as in the case of Ge) and the temperature was kept at 300 ^{0}K.

4.6.2 Band gap

The band gap is an intrinsic feature of materials and even for semiconductors it vastly varies from narrow-gap semiconductors (0.17 eV in InSb) to wide-gap semiconductors (3.54 eV in ZnS). Carrier concentration in the gap comes from the tail of the Fermi-Dirac distribution function and inversely changes versus the band gap, e.g. higher electron/hole concentration in the gap for a smaller band gap. In the case of a wide band gap semiconductor, Chemical potentials towards the middle of the gap fall far from the tail of the Fermi-Dirac distribution function, as a result, there might be no electrons/holes at a range of chemical potentials.

For the Nernst effect, the coexistence of electrons and holes in the gap is desired, thus, the band gap needs to be relatively narrow. For very small band gaps, However, the electron/hole concentration would be fairly larger which would lead to a considerable electrical conduct-

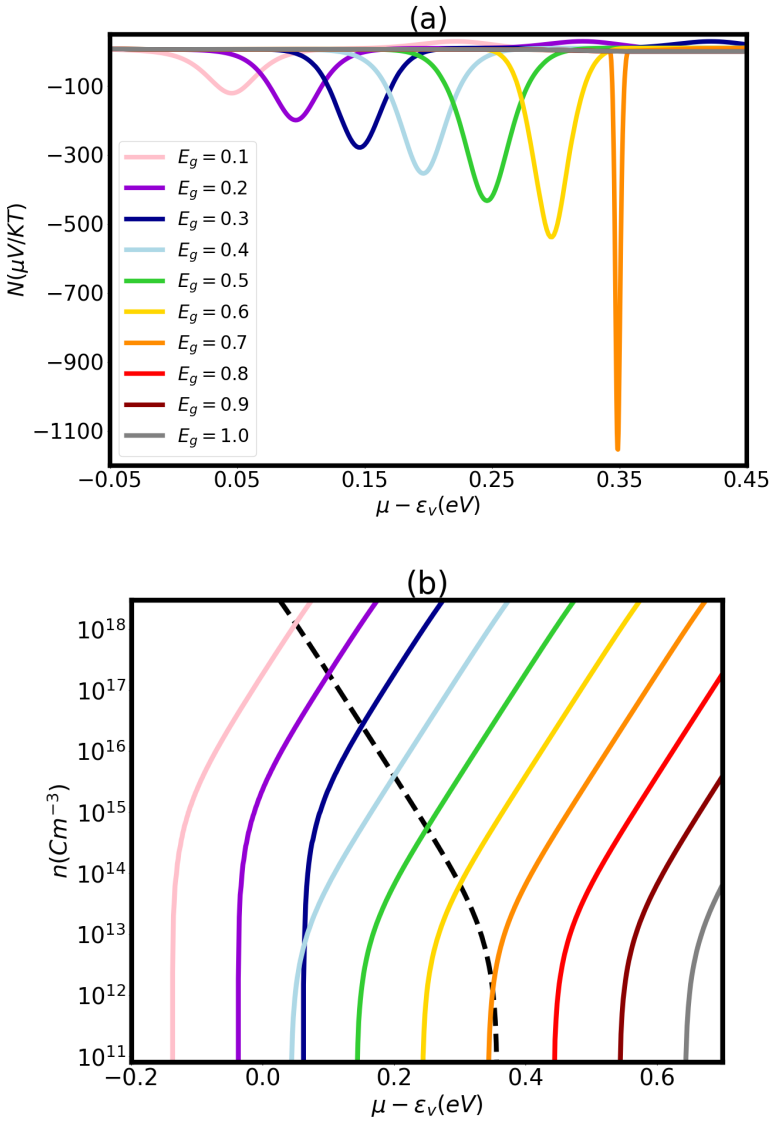

Figure 4.16: Nernst coefficient versus chemical potential for various band gap values (a). electron concentration (dashed lines) and hole concentration (black solid line) (b). Colors correspond to (a).

ivity. As the electrical conductivity grows the Nernst signal measurement setup will be more likely to become short-circuit and the Nernst signals will vanish. Therefore, there has to be an optimum value of the band gap for larger Nernst signals.

Fig 4.16 exhibits the Nernst signal changes with respect to the band gap values ranging from 0.1 eV to 1.0 eV for a two-spherical band system with an equal electron-hole effective mass of $0.5m_0$. Similar to the Seebeck coefficient, the Nernst coefficient grows as the band gap increases, though, for the band gap values larger than 0.7 eV the Nernst signal in the gap vanishes. The reason lies in the coexistence of holes and electrons in the gap. As the band gap goes beyond 0.7 eV electrons and holes no longer coexist and the Nernst effect will be terminated(Fig 4.16).

4.6.3 Effective mass

Effective mass was found as a significant element in charge transport phenomena. Not only does the mobility principally rely on effective mass, but electron and hole concentrations are determined by effective mass, thence, effective mass in the Nernst effect plays a crucial role. The band gap was kept at 0.7 eV, which was found to be the optimum value, and the effective mass of both bands was concurrently changed from 0.1 m_0 to m_0. Fig 4.18(a) reveals smaller effective mass values cause outstandingly larger Nernst coefficient in the gap which is attributed to higher mobility. Fig 4.18(b) discloses the electron and hole concentration continuously diminish as the effective mass is reduced. It is noteworthy to emphasize that since the band gap was held unchanged the minimum electron and hole concentrations remain at the same chemical potential but continuously reduce as for a spherical band density of states which is proportional to $m\sqrt{m}$. Basically, there are no optimized values and basically smaller effective mass values are preferred for large Nernst signals.

Moreover, at the band edges where the relaxation time is maximum, the Nernst coefficient happens to increase. As the effective mass is reduced the mobility will rise which triggers the Nernst coefficient to grow (4.18 (c)). More eminently, a light effective mass can compensate for the effect of the band gap. Fig exhibits that the Nernst signals of a narrow band gap semiconductor (E_g=0.10 eV) with the effective mass of 0.1 m_0 for each band could be multiple times higher rather than the case of E_g=0.7 but m_v=m_c=0.5m_0, whether in the gap

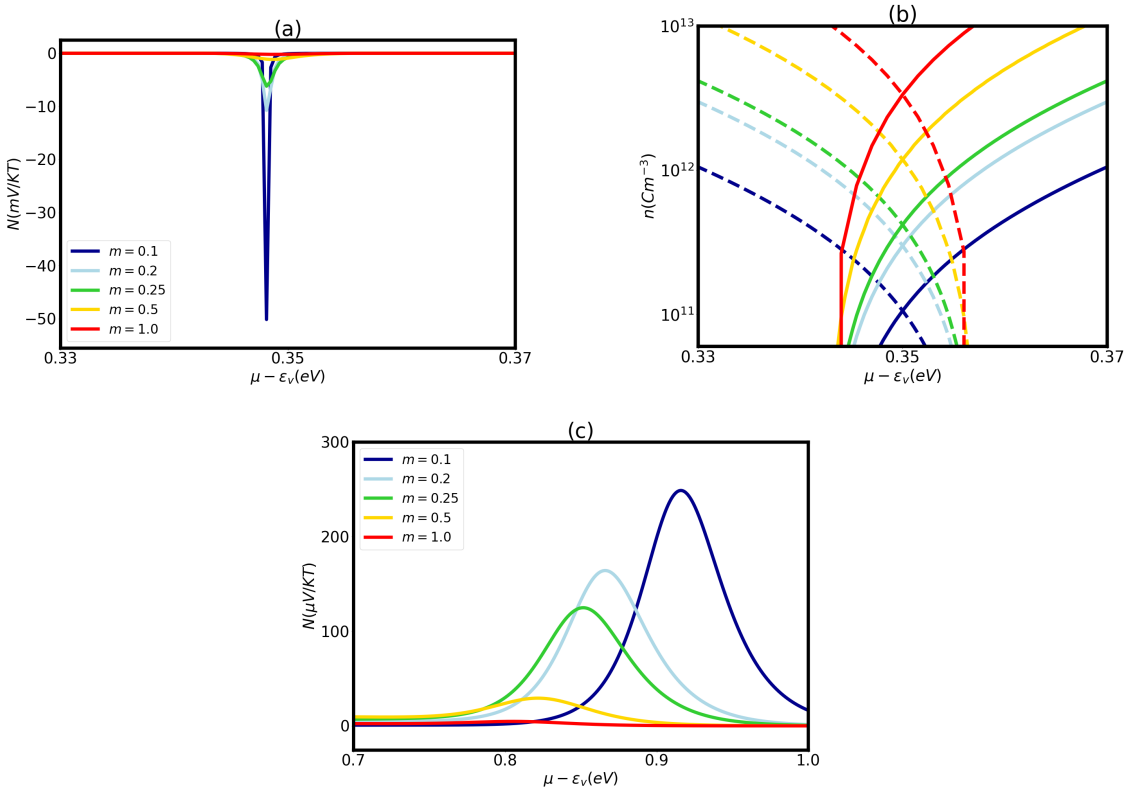

Figure 4.17: Nernst coefficient surges versus the inverse of effective mass (a). intrinsic electron concentration (dashed lines) and hole concentration (solid lines) dwindle at smaller effective masses(b). Larger Nernst signals for lighter mass values at the conduction band edge (c). Colors are corresponding to (a).

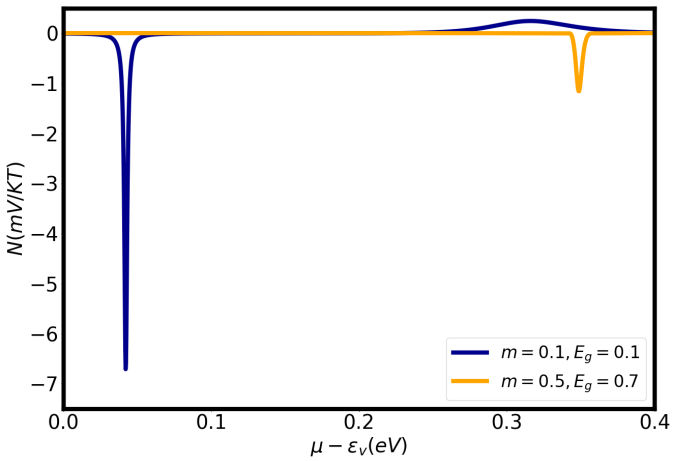

Figure 4.18: Effective mass dominates the band gap to yield a large Nernst coefficient.

or around the band edges. This behavior was earlier observed in the experiments, namely in topological Dirac semimetals such as TaP [165], TaAs [165], NbP [166], and NbAs [167] significantly large Nernst coefficient values were recorded. It can then be concluded that the effective mass is the right descriptor for the Nernst coefficient.

4.7 Technological applications

The study of thermomagnetic applications was begun in the 50s on Ge [120] and Bi [168], but it did not last long because of the induction of a strong magnetic field that would result in a significant amount of energy loss. Advances in superconducting magnets ease the induction of strong magnetic fields. As a result, possible applications of the Nernst effect have caught attention in the last decade.

4.7.1 Cryogenic cooling

Lowering temperature below 100 ^{0}K is widely used for quantum computing, superconductors, and cold hardening. According to the National Institute of Standards and Technology (NIST) cryogenic cooling is defined as lowering temperature as much as 93 ^{0}K or lower. Such low temperatures are often reached by liquid nitrogen with a boiling temperature of 77 ^{0}K. Maintaining a system at the cryogenic condition requires the continuous monitoring of heat flux. A Nernst- Ettingshausen cooler would provide better control of temperature rather than balancing the heat flux with a reservoir and liquid nitrogen.

Nernst-Ettingshausen coolers are based on Thermomagnetic phenomena. In the presence of an electric current, a fraction of electrons are pushed toward the bottom of the sample (-y-direction). The absence of electrons would release their energy as an exothermic reaction and raise the temperature of its vicinity, known as crystal heating. At the same time, the resulting electron-hole pairs at the opposite side (+y-direction) absorb energy from the lattice that will cool the top of the sample, ergo, a temperature gradient will be generated along the sample. Bogason and Heremans made a Nernst-Ettingshausen cooler of Bismuth single crystal and observed a temperature difference of 5 ^{0}K by applying an electric current of 3 A [123].

4.7.2 Nernst- based thermopile systems

A Thermopile is composed of multiple thermocouples connected in series or, less frequently, in parallel. Thermopiles have been utilized to convert thermal energy into electrical energy based on the thermoelectric effect. It was recently proposed to design thermopiles working on the principles of the Nernst effect [169, 170]. Nernst- based thermopiles manifest advantages over their Seebeck-based counterparts such as more flexibility in structures and lower cost. Interestingly, the conversion efficiency of a Nernst-based thermopile can be improved with the assistance of the device architecture. Mizuguchi and Nakatsuji [125] posited that a Nernst-based thermopile system consisting of ferromagnetic wires is the most efficient design. In their device, ferromagnetic FePt and nonmagnetic Cr wires were connected in series and the Nernst voltage was observed to improve for a larger number of wires and it may reach over 0.8 mV for 120 FePt wires under a magnetic field of 2 T and a temperature gradient of 3.3 K/mm (Fig 4.19).

4.7.3 Radiation detector

Thermopiles are commonly utilized in thermal radiation detection. Despite its lower performance compared to photoconductors, it efficiently runs over a wide range of wavelengths and it does not need to be refrigerated. Though, long response times are the main issue of thermopiles as thermal radiation detectors. Radiation detectors based on the Nernst effect emerged as favorable substitutes for thermopiles as they own strikingly shorter response times. Since in a Nernst module the voltage is perpendicular to the temperature gradient the thermal path length can become impressively small. For a radiation detector, in addition to

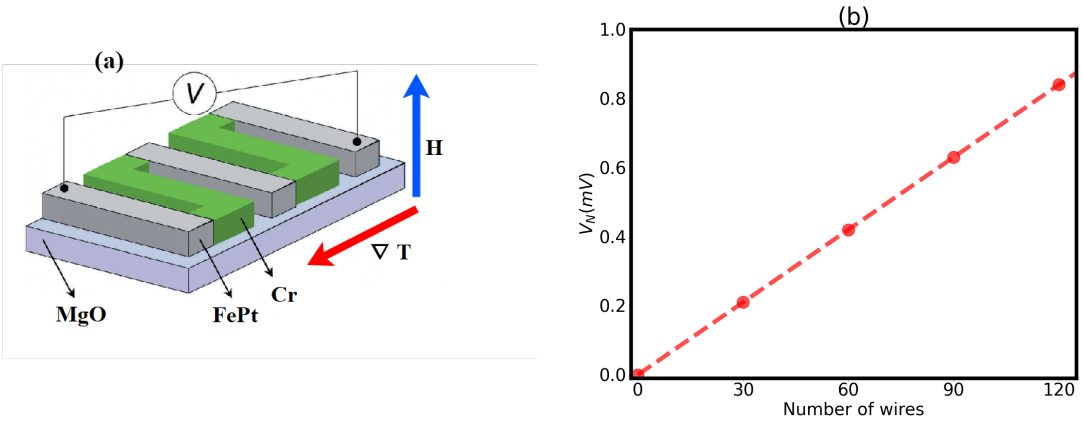

Figure 4.19: A thermopile based on the Nernst effect made of Fe/pt and Cr wires (a). The Nernst voltage in the thermopile is linearly proportional to number of wires (b).

the efficiency of thermal energy conversion to electrical energy, response time is of great importance.

Assuming the device's width along the magnetic field is measured to be "d" while its length along the Nernst voltage is "l" with a thickness of "t" we could record the developed voltage as a function of the thermal radiation intensity (I) as V=NHlI/κ, where κ is the thermal conductivity. For a reasonably thick sample, the response time (τ_r) is estimated by $\tau_r = \alpha C t^2/\kappa$ in which C is the heat capacity and α is a constant. Substituting the thickness and the product of width by a length with the surface area, the ratio of the developed voltage to the thermal radiation intensity is assembled.

$$\frac{V}{I} = (\frac{\tau_r}{\alpha})^{1/4}\sqrt{AR}\frac{NH}{\kappa^{3/4}C^{1/4}\sqrt{\rho}} \tag{4.8}$$

In which $\frac{NH}{\kappa^{3/4}C^{1/4}\sqrt{\rho}}$ is identified as the merit factor for a thermomagnetic detector material. Bismuth alloys, InSb-NiSb, and Cd_3As_2-NiAs materials were found to work efficiently for thermomagnetic radiation detector applications [124].

4.8 Conclusion

In this chapter, I proposed an efficient approach to compute the Nernst coefficient based on the first-principles density functional theory within relaxation time approximation. Unlike the constant relaxation time approximation, in this chapter, I account for the charge carrier

relaxation time caused by various mechanisms. Despite the phenomenological models, our approach does not perform any fitting and it is based on MLWFs. In order to authenticate the method, our findings were compared to experimental data of Ge, InSb, Bi, and Si. The effects of experimental conditions such as temperature, doping concentration, and strength of the magnetic field were investigated and a remarkable accuracy was observed in a moderate computational cost. This approach is valid within the validity of the DFT and the validity of the AMSET code used for relaxation times calculations and it accelerates the materials discovery and prediction of promising candidates for thermomagnetic applications.

CHAPTER V

Charge carrier relaxation time for doped semiconductors

5.1 Introduction

Electronic materials are ubiquitous in science and industry such as transistors [171, 172], photonic materials [173, 174],batteries [175–177], thermoelectric [178–180],quantum simulators [181, 182], photovoltaic [183], and sensors [184, 185] for detection of biological and chemical species [186, 187]. Electronic devices are based on charge transfer which strongly depends on the possible scattering mechanisms. In other words, for all applications of electronic materials charge transfer is the key to choosing a promising candidate that meets the required conditions.

The Boltzmann transport equation (BTE) describes the charge transfer in solids [188] and is often solved within the relaxation time approximation (RTA) which assumes the collision term is inversely proportional to the carrier relaxation time. The most commonly used way to deal with the carrier relaxation time is to assume a constant value for the relaxation time, known as the constant relaxation time approximation (CRTA). CRTA makes the computations less heavy, though, in some cases it produced unrealistic data [189, 190]. The efforts to go beyond CRTA have been going on for decades starting from the empirical models [114, 164, 191–193] to the parabolic and non-parabolic band models that worked for some materials like SiGe [194], MoS2 [195] , BaGaGe [196], and half-heusler compounds [197]. Such models are not universal and are likely to inaccurately predict the experiments [132].

In recent years, attempts have been made to find scattering rates from the first-principles density functional theory. Noffsinger et.al. [131] proposed a way to compute electron-phonon coupling through maximally-localized Wannier functions and density-functional perturbation theory. They calculated electron-phonon interaction self-energies, electron-phonon spectral functions, and electron-phonon coupling strengths. Their method is very accurate

but requires very dense sampling of the Brillouin zone and might be computationally heavy. Samsonidze and Kozinsky [198] simplified the electron-phonon coupling matrix calculation by integrating over energy instead of integration over momentum-space. It dramatically decreased the computational cost but appeared to deviate for semiconductors with strongly anisotropic effective masses. Similarly, Graziosi [132] approximated the momentum-dependent relaxation time with state velocities and successfully evaluated the thermoelectric power factor of five Co-based half-Heusler alloys. Ganose et.al. [134] began from the isotropic equations and then extended them to cover anisotropic bands including ionized impurity, piezoelectric scattering, and electron-phonon coupling interactions. Their code was tested on a group of materials and the results were in relative agreement with the experimental measurements of mobility and the Seebeck coefficient. Although their code significantly lowered the computer operation time, eigenvalues and group velocities required to calculate scattering rate and transport distribution function were governed by Fourier interpolation of the band structures which were found to be less accurate compared to the maximally-localized Wannier functions. More recently, the PERTURBO code [199] was developed to assess charge transport and carrier dynamics based on Wannier interpolation. It yields remarkably accurate results, though, density functional perturbation theory calculations are needed which might take considerably longer.

As a side project, I demonstrate a new approach to compute the isotropic scattering rates for doped semiconductors with the assumption of elastic collisions for electron-phonon due to various mechanisms as well as ionized impurity interactions with the basis sets of maximally-localized Wannier functions. Our method does not need DFPT calculations and relies on some physical properties of materials that can be taken directly from the experimental data and all the scattering rates are treated as a function of $\vec{k}$. Electrical resistivity and mobility values for different materials were computed at a reasonable computational cost and our theoretical results emerged fairly close to the experiments.

5.2 Results

In an electronic device, charge carriers are likely to collide with phonons, impurities, and even other carriers. Such collisions are often assessed by the probability of transition from

an initial state with the wave vector of k in the state n to the final state with the wave vector of k' in the state n' per unit time known as the scattering rates. The perturbation Hamiltonian H' illustrates the scattering rate by the Fermi golden rule as below:

$$P(k,k') = \frac{2\pi}{\hbar}\Big| < n',k'|H'|n,k > \Big|^2 \delta(\varepsilon(n',k') - \varepsilon(n,k) - \Delta\varepsilon) \tag{5.1}$$

Where $\Delta\varepsilon$ shows the change in energy and is expressed by $\hbar\omega$ in the case of phonon scattering. The term $< n',k'|H'|n,k >$ is referred as the Matrix element, $M(k,k')$, and is specified by the scattering mechanism. Using plane wave approximation, One may approximate the matrix element as $\frac{1}{V}\int e^{-ik'.r} H' e^{ik.r} d^3r$, which is known as the Born approximation.

5.2.1 Electron–Phonon scattering rates – deformation potential

According to the deformation-potential theory, the perturbation of electrons or holes by the lattice vibrations originates from the lattice deformation. The perturbation Hamiltonian is a function of the change of the displacement field of atoms, $y(r)$ with respect to the positions and the deformation potential tensor($\mathcal{D}$).

$$H' = \sum_{i,j} \mathcal{D}_{ij} \frac{\partial y_i}{\partial r_j} \tag{5.2}$$

The displacement of an atom from its equilibrium position in terms of the wave vector $q = \pm k \mp k' + G$ is expressed by:

$$y(r) = \sum_{q,l} p_{q,l} \sqrt{\frac{\hbar}{2V\rho\omega(q)}} \left(a_{ql}^- + a_{ql}^+\right) e^{iqr} \tag{5.3}$$

In which l is the phonon mode, p is polarization, ρ is mass density and ω is angular frequency. Phonons may be created (a_{ql}^+) or annihilated (a_{ql}^-). Eq. 5.3 gives the perturbation Hamiltonian for the deformation potential.

$$H' = \sum_{i,j} \mathcal{D}_{ij} \sum_{q,l} [p_{q,l}] iq \sqrt{\frac{\hbar}{2V\rho\omega(q)}} \left(a_{ql}^- + a_{ql}^+\right) e^{iqr} \tag{5.4}$$

The summations in Eq. 5.4 are the Fourier transform of $\sum_{i,j}\mathcal{D}_{ij}\sum_{q,l}[p_l]iq\sqrt{\frac{\hbar}{2V\rho\omega(q)}}a_{q,l}$. Besides, number of phonons(N) in the state n is acquired by the quantum operators.

$$\begin{aligned} N_{ql} &= \left|< n'|a^{-}_{q,l}|n >\right|^2 \\ N_{ql}+1 &= \left|< n'|a^{+}_{q,l}|n >\right|^2 \end{aligned} \tag{5.5}$$

Collecting the above equations in the scattering rate equation 5.1 I can formulate the probability of transition from an initial state to a final state.

$$P(k,k') = \frac{\pi}{V\rho\omega(q)}\begin{bmatrix} N_{ql} \\ N_{ql}+1 \end{bmatrix}\left|\sum_{ij}\mathcal{D}_{ij}q[p_{q,l}]\right|^2\delta(\varepsilon(n',k')-\varepsilon(n,k)-\hbar\omega) \tag{5.6}$$

5.2.1.1 Acoustic phonons

Acoustic phonon population in equilibrium is assessed by the equipartition theorem as N=$\frac{1}{\exp(\frac{\hbar q\nu_s}{k_BT})-1}$. Acoustic phonon energy ($\hbar q\nu_s$) is significantly smaller than thermal energy (k_BT), thus acoustic phonon population can be approximated by Taylor's expansion.

$$N_q = \frac{1}{\exp(\frac{\hbar q\nu_s}{k_BT})-1} \approx \frac{1}{1+\frac{\hbar q\nu_s}{k_BT}+\frac{1}{2}(\frac{\hbar q\nu_s}{k_BT})^2-1} \approx \frac{k_BT}{\hbar q\nu_s}-\frac{1}{2} \tag{5.7}$$

The ratio of velocity (ν) to the angular frequency ω is wave vector as $q=\nu/\omega$. Furthermore, acoustic phonon energy ($\hbar\omega$) is negligible compared to elctron energy $\varepsilon(n,k)$, thus $\delta(\varepsilon(n',k')-\varepsilon(n,k)-\hbar\omega)\approx\delta(\varepsilon(n,k')-\varepsilon(n,k))$. As a consequence, Eq.5.6 can be further simplified.

$$P^{ac}(k,k')=\frac{\pi\mathcal{D}_A^2 q}{\rho\, V\nu_s}\left[\frac{k_BT}{\hbar q\nu_s}\mp\frac{1}{2}\right]\delta\left(\varepsilon(n',k')-\varepsilon(n,k)\right) \tag{5.8}$$

Deformation potential scattering by acoustic phonons is an elastic scattering in which final states caused by emission or absorption are not distinguishable, therefore, the sum of emission and absorption should be considered.

$$P^{ac}(k,k') = \frac{2\pi D_A^2 k_BT}{\hbar\rho V\nu_s^2}\delta(\varepsilon(n',k')-\varepsilon(n,k)) \tag{5.9}$$

Total scattering probability per time is obtained by integration over all final states (k') in Brillouin zone volume. Herein, I integrate over all states with the assumption of isotropic

collisions.

$$\begin{aligned}\frac{1}{\tau^{ac}(k,k')} &= \frac{V}{(2\pi)^3}\int_0^{2\pi} d\phi \int_{-1}^{1} d\cos\theta \int_0^{\infty} \frac{2\pi\mathcal{D}_A^2 k_B T}{\hbar\rho V \nu_s^2}\delta(\varepsilon(n',k')-\varepsilon(n,k))k'^2 dk' \\ &= \frac{V(2\pi)(2)}{(2\pi)^3}\frac{2\pi\mathcal{D}_A^2 k_B T}{\hbar\rho V\nu_s^2}\int \delta(\varepsilon(n',k')-\varepsilon(n,k))k'^2 dk' \\ &= \frac{\mathcal{D}_A^2 k_B T}{\pi\hbar\nu_s^2\rho}\int \delta(\varepsilon(n',k')-\varepsilon(n,k))k'^2 dk'\end{aligned} \tag{5.10}$$

Where τ is the charge carrier relaxation time. Elastic constant $\mathcal{C}$ relates sound velocity ν_s and density ρ as $\nu_s^2\rho = \mathcal{C}$.In order to solve the last integral with δ function, I need to focus on the definition of density of states $g(\varepsilon)$.

$$\begin{aligned} g(\varepsilon) &= \frac{2}{(2\pi)^3}\int dV \int_0^{\infty} k^2 dk \quad \delta[\varepsilon(k')-\varepsilon(k)] \\ g(\varepsilon) &= \frac{2}{(2\pi)^3}4\pi\int_0^{\infty} k^2 dk \quad \delta[\varepsilon(k')-\varepsilon(k)] \\ \pi^2 g(\varepsilon) &= \int_0^{\infty} k^2 dk \quad \delta[\varepsilon(k')-\varepsilon(k)]\end{aligned} \tag{5.11}$$

Therefore, total scattering by acoustic phonons 5.10 may be written as a function of energy.

$$\frac{1}{\tau^{ac}(\varepsilon)} = \frac{\mathcal{D}_A^2 k_B T\pi^2}{\pi\hbar\mathcal{C}}g(\varepsilon) = \frac{\mathcal{D}_A^2 k_B T\pi}{\hbar\mathcal{C}}g(\varepsilon) \tag{5.12}$$

5.2.1.2 Optical phonons

The energy of optical phonons is comparable to the thermal energy and the Eq. 5.7 is not applied to optical phonons. Furthermore, emission and absorption are distinguishable for optical phonons. Integration of Eq. 5.6 over all states yields the charge carrier relaxation time due to optical phonon deformation potential.

$$\begin{aligned}\frac{1}{\tau^{op}(k)} &= \frac{V}{(2\pi)^3}\int_0^{2\pi} d\phi \int_{-1}^{1} d\cos\theta \int_0^{\infty} \frac{\pi\mathcal{D}_{op}^2}{\rho V\omega_{op}}\begin{bmatrix} N_{op} \\ N_{op}+1\end{bmatrix}\delta[\varepsilon(n',k')-\varepsilon(n,k)\pm\hbar\omega_{op}]k^{2\prime}dk' \\ &= \frac{4\pi\mathcal{D}_{op}^2}{8\pi^2\rho\omega_{op}}\int\begin{bmatrix} N_{op} \\ N_{op}+1\end{bmatrix}\delta[\varepsilon(n',k')-\varepsilon(n,k)\pm\hbar\omega_{op}]k^{2\prime}dk'\end{aligned} \tag{5.13}$$

Assuming optical phonon density is independent of wave vector and density of states 5.11, it will be simplified to:

$$\frac{1}{\tau^{op}(\varepsilon)} = \frac{\pi \mathcal{D}_{op}^2}{2\rho\omega_{op}} \begin{bmatrix} N_{op} \\ N_{op}+1 \end{bmatrix} g(\varepsilon \pm \hbar\omega_{op}) \tag{5.14}$$

In which $g(\varepsilon \mp \hbar\omega_{op})$ is shifted density of states by $\hbar\omega_{op}$. This equation looks identical to Jacoboni's [164] and Lundstrom's [114].

5.2.2 Electron–phonon scattering rates – electrostatic interaction

In semiconductors with more than one type of atoms vibrating dipoles are associated with optical phonons. Moreover, lack of inversion symmetry causes acoustic phonons to be associated with the strain field, and as a consequence, a polarization field will be generated. These phenomena are long-range interactions of electrons with phonons that are named piezoelectric scattering and polar scattering for acoustic phonons and optical phonons, respectively.

5.2.2.1 Acoustic phonons – piezoelectric scattering

According to the Ridely [200], analogous to the deformation potential scattering, for the piezoelectric effect polarization filed is expressed in terms of strain and the piezoelectric stress constant (d_{pz}).

$$P_\alpha(r) = \sum_{\beta\gamma} d_{pz_{\alpha\beta\gamma}} \frac{\partial y_\beta(r)}{\partial r_\gamma} \tag{5.15}$$

After doing the similar procedures Eq. 5.2-Eq. 5.4 for the piezoelectric scattering with the help of Fourier transformation and polarization theory, the matrix element for piezoelectric scattering is achieved [201].

$$M(k,k') = \left(\frac{e d_{pz}}{\epsilon_r \epsilon_0}\right)^2 \frac{k_B T}{V\mathcal{C}} \left(\frac{q}{q^2+q_0^2}\right)^2 \tag{5.16}$$

Where ϵ_r and ϵ_0 are the low-frequency dielectric constant and vacuum permittivity, respectively. q_0 is the inverse of Debye length, also known as screening length, and is attained by $1/q_0 = \sqrt{\frac{\epsilon_0}{e^2}(\frac{\partial n}{\partial \mu})^{-1}}$. d_{pz} is the average value of piezoelectric stress constants in the units C/m^2 over all directions to generate a spherically symmetric average. Using the aforementioned matrix element and Eq. 5.1 the charge carrier relaxation time due to piezoelectric

interaction will be earned.

$$\begin{aligned}\frac{1}{\tau^{pz}(k)} &= \frac{2\pi V}{\hbar(2\pi)^3}\int_0^{2\pi} d\phi \int_0^{\infty} k^{2\prime} dk' \delta(\varepsilon(n',k') - \varepsilon(n,k)) \int_{-1}^{1} \left(\frac{ed_{pz}}{\epsilon_r\epsilon_0}\right)^2 \frac{k_B T}{V\mathcal{C}} \frac{q^2 d\cos\theta}{(q^2+q_0^2)^2} \\ &= \frac{2\pi}{\hbar}\frac{2\pi V}{(2\pi)^3}\pi^2 g(\varepsilon) \int_{-1}^{1} \left(\frac{ed_{pz}}{\epsilon_r\epsilon_0}\right)^2 \frac{k_B T}{V\mathcal{C}} \frac{q^2 d\cos\theta}{(q^2+q_0^2)^2}\end{aligned} \tag{5.17}$$

q relates the initial and final states as $q^2 = |k-k'|^2 = 2k^2(1-\cos\theta) = 4k^2\sin^2(\theta/2)$, where θ is the deflection angle.Changing the variable $1-\cos\theta = u$ in 5.17 I will face a familiar integral.

$$\begin{aligned}\frac{1}{\tau(k)} &= \left(\frac{ed_{pz}}{\epsilon_r\epsilon_0}\right)^2 \frac{\pi k_B T g(\varepsilon)}{2\hbar\mathcal{C}} \int_{-2}^{0} \frac{-2k^2 u du}{(q_0^2+2k^2u)^2} \\ &= \left(\frac{ed_{pz}}{\epsilon_r\epsilon_0}\right)^2 \frac{\pi k_B T g(\varepsilon) k^2}{2\hbar\mathcal{C}} \int_{0}^{2} \frac{u du}{(q_0^2+2k^2u)^2} \\ &= \left(\frac{ed_{pz}}{\epsilon_r\epsilon_0}\right)^2 \frac{\pi k_B T g(\varepsilon) k^2}{2\hbar\mathcal{C}} \frac{1}{4k^4}\left[\ln\frac{4k^2+q_0^2}{q_0^2} - \frac{4k^2}{4k^2+q_0^2}\right] \\ &= \left(\frac{ed_{pz}}{\epsilon_r\epsilon_0}\right)^2 \frac{\pi k_B T g(\varepsilon)}{\hbar\mathcal{C}} \frac{1}{8k^2}\left[\ln\frac{4k^2+q_0^2}{q_0^2} - \frac{4k^2}{4k^2+q_0^2}\right]\end{aligned} \tag{5.18}$$

5.2.2.2 Optical phonons – polar scattering

The polarization due to interactions between optical phonons and ionic charges of atoms is given by $P(r) = e^* y(r)/\mathcal{V}$, where e^* is the effective charge on atoms and is determined by ${e^*}^2 = \epsilon_0 M\omega_{op}^2 \mathcal{V}(1/\epsilon_r^{\infty} - 1/\epsilon_r)$[202, 203]. Note that $\mathcal{V}$ is the total volume which equals the number of units multiplied by the unit cell volume. Similar to optical phonon deformation potential, for the polar scattering by optical phonons the energy difference between the final and initial states is $\hbar\omega_{op}$. Derivation of the matrix element is thoroughly explained in the references [114, 164, 193] and I directly use their results.

$$M(k,k') = \left(N_{op} + \frac{1}{2} \mp \frac{1}{2}\right) \frac{\hbar e^2 \omega_{op}}{2\epsilon_0 V}\left(\frac{1}{\epsilon_r^{\infty}} - \frac{1}{\epsilon_r}\right)\left(\frac{q}{q^2+q_0^2}\right)^2 \tag{5.19}$$

Likewise 5.17, the above summation can be turned into three integrals.

$$\begin{aligned}\frac{1}{\tau^{po}(k)} &= \frac{2\pi V}{\hbar(2\pi)^3}\int_0^{2\pi} d\phi \int_0^{\infty} k^{2\prime} dk' \delta\left[\varepsilon(n',k') - \varepsilon(n,k) \pm \hbar\omega_{op}\right] \\ &\left(N_{op} + \frac{1}{2} \mp \frac{1}{2}\right)\frac{\hbar e^2 \omega_{op}}{2\epsilon_0 V}\left(\frac{1}{\epsilon_r^{\infty}} - \frac{1}{\epsilon_r}\right)\int_{-1}^{1}\left(\frac{q}{q^2+q_0^2}\right)^2 (1-\cos\theta) d\cos\theta \\ = \frac{\pi e^2 \omega_{op}}{4\epsilon_0} g(\varepsilon \pm \hbar\omega_{op}) &\left(N_{op} + \frac{1}{2} \mp \frac{1}{2}\right)\left(\frac{1}{\epsilon_r^{\infty}} - \frac{1}{\epsilon_r}\right)\int_{-1}^{1}\left(\frac{q}{q^2+q_0^2}\right)^2 (1-\cos\theta) d\cos\theta\end{aligned} \tag{5.20}$$

In the above $q = 2k' sin(\theta/2)$. Analogous to 5.18, the above integral is solved and the optical phonon polar interaction relaxation time is derived.

$$\begin{aligned}\frac{1}{\tau^{po}(k)} = \frac{\pi e^2 \omega_{op}}{4\epsilon_0} g(\varepsilon \pm \hbar\omega_{op}) &\left(N_{op} + \frac{1}{2} \mp \frac{1}{2}\right)\left(\frac{1}{\epsilon_r^{\infty}} - \frac{1}{\epsilon_r}\right) \\ \frac{1}{k^2}&\left[\frac{q_0^2}{2k^2}\ln\frac{q_0^2}{4k^2+q_0^2} + \frac{q_0^4}{4k^2}\left(\frac{1}{q_0^2} - \frac{1}{4k^2+q_0^2}\right) + 1\right]\end{aligned} \tag{5.21}$$

The top sign signifies absorption while the bottom sign indicates emission and only applies when $\varepsilon(n,k) > \hbar\omega$.

5.2.3 Ionized impurity scattering

Ionized impurity scattering is attributed to a screened Coulomb potential which is estimated by an exponential form of screening potential ($\mathbf{V}(r)$) based on the Brooks and Herring approach [204].

$$\mathbf{V}(r) = \frac{ze(-e)}{4\pi\epsilon}\exp(-q_0 r) \tag{5.22}$$

Where z is the number of charge units of the impurity. Following the definition of matrix element and Fourier transformation, the matrix element is earned as below:

$$M^{ii}(k,k') = \frac{n_i z^2 e^4}{V\epsilon^2}\frac{1}{(q^2+q_0^2)^2} \tag{5.23}$$

In which n_i is the ionized impurity concentration and $\epsilon = \epsilon_0 \cdot \epsilon_r$. Following the Eq 5.1 the charge carrier relaxation time will be governed.

$$\frac{1}{\tau^{ii}(k,k')} = \frac{2\pi}{\hbar}\frac{n_i z^2 e^4}{V\epsilon^2}\frac{1}{(q^2+q_0^2)^2}\delta[\varepsilon(n',k') - \varepsilon(n,k)] \tag{5.24}$$

An ionized impurity deflects charge carriers by an angle such that a fraction of the incident wave vector will be retained. Thus, only a part of transitions occurs and the total scattering

needs to be modified by a factor of $1-\cos\theta$. Note that in the ionized impurity scattering there is no energy difference between the initial and the final states. q relates the initial and final states as $q^2 = |k-k'|^2 = 2k^2(1-\cos\theta) = 4k^2\sin^2(\theta/2)$, where θ is the deflection angle. Switching to the polar coordinates, the total relaxation time is obtained by:

$$\begin{aligned}
\frac{1}{\tau^{ii}(k,k')} &= \frac{V}{(2\pi)^3}\int_0^{2\pi} d\phi \int_0^{\infty} k'^2 dk' \int_{-1}^{1} P(k,k')(1-\cos\theta)d\cos\theta \\
&= \frac{V}{(2\pi)^3}\int_0^{2\pi} d\phi \int_0^{\infty} k'^2 dk' \int_{-1}^{1} \frac{2\pi}{\hbar}\frac{n_i z^2 e^4}{V\epsilon^2}\frac{\delta[\varepsilon(n',k')-\varepsilon(n,k)]}{(q^2+q_0^2)^2}(1-\cos\theta)d\cos\theta \\
&= \frac{V}{(2\pi)^3}\int_0^{2\pi} d\phi \int_0^{\infty} k'^2 dk' \int_{-1}^{1} \frac{2\pi}{\hbar}\frac{n_i z^2 e^4}{V\epsilon^2}\frac{\delta[\varepsilon(n',k')-\varepsilon(n,k)]}{(2k^2(1-\cos\theta)+q_0^2)^2}(1-\cos\theta)d\cos\theta
\end{aligned} \tag{5.25}$$

Let's first solve the innermost integral by changing the variables $1-\cos\theta = u$ and $d\cos\theta = -du$.

$$\begin{aligned}
\frac{1}{\tau^{ii}(k,k')} &= \frac{\Omega}{(2\pi)^3}\int_0^{2\pi} d\phi \int_0^{\infty} k'^2 dk' \frac{2\pi n_i z^2 e^4 \delta[\varepsilon(n',k')-\varepsilon(n,k)]}{\hbar\Omega\epsilon^2}\int_2^0 \frac{-u\quad du}{(2k^2u+q_0^2)^2} \\
&= \frac{1}{(2\pi)^2\hbar}\int_0^{2\pi} d\phi \int_0^{\infty} k'^2 dk' \frac{n_i z^2 e^4 \delta[\varepsilon(n',k')-\varepsilon(n,k)]}{\epsilon^2}\frac{1}{4k^4}\left[\ln(\frac{2k^2u+q_0^2}{q_0^2}) + \frac{q_0^2}{4k^2(2k^2u+q_0^2)}\right]_0^2 \\
&= \frac{1}{(2\pi)^2\hbar}\int_0^{2\pi} d\phi \int_0^{\infty} k'^2 dk' \frac{n_i z^2 e^4 \delta[\varepsilon(n',k')-\varepsilon(n,k)]}{\epsilon^2}\frac{1}{4k^4}\left[\ln(\frac{4k^2+q_0^2}{q_0^2}) - \frac{4k^2}{4k^2+q_0^2}\right] \\
&= \frac{2\pi}{(2\pi)^2\hbar}\frac{n_i z^2 e^4}{4k^4\epsilon^2}\left[\ln(\frac{4k^2+q_0^2}{q_0^2}) - \frac{4k^2}{4k^2+q_0^2}\right]\int_0^{\infty} k'^2 dk' \delta[\varepsilon(n',k')-\varepsilon(n,k)]
\end{aligned} \tag{5.26}$$

The most recent integral has appeared before in 5.11. Such that, the ionized impurity scattering is articulated.

$$\frac{1}{\tau(k)} = \frac{\pi n_i z^2 e^4}{8\hbar k^4\epsilon^2}\left[\ln(\frac{4k^2+q_0^2}{q_0^2}) - \frac{4k^2}{4k^2+q_0^2}\right] g(\varepsilon) \tag{5.27}$$

5.3 Methods

Electronic structures were achieved using DFT as implemented in QUANTUM ESPRESSO package [115] and then the band structures were wannierized in order to have a finer band interpolation via maximally localized Wannier functions (MLWF), as implemented in the Wannier90 package [40]. All the integrals discussed in Section 5.2 were performed in the

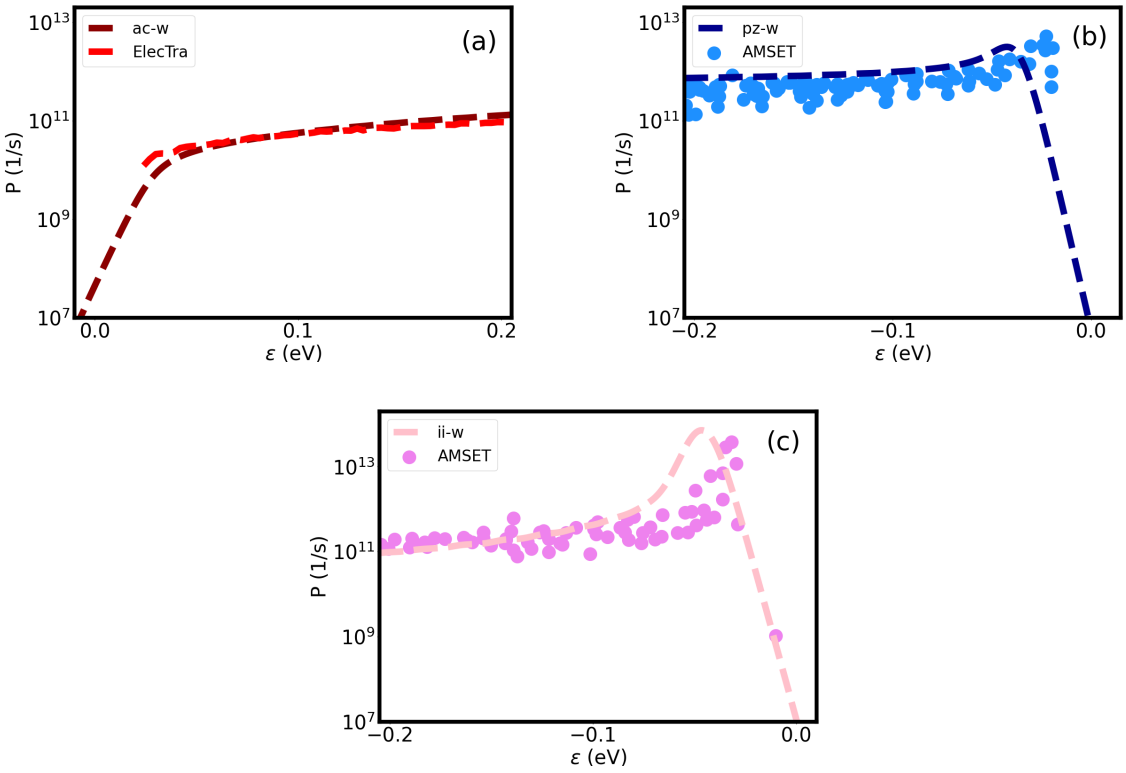

Figure 5.1: The MLWF-based scattering rates (w) versus AMSET and ElecTra codes of n-type (a) and p-type (b,c) GaAs with doping of $10^{15} cm^{-3}$ for acoustic phonon deformation potential (a), piezoelectric (b), and ionized impurity (c) mechanisms.

reciprocal space on the fine MLWFs. The physical properties of each material were taken from the experiments and the total scattering rate is summed over all the mechanisms according to Matthiessen's rule [137]. Lastly, after convergence was assured, carrier mobility was calculated and compared to the experimentally measured values from the literature.

5.4 Discussion

5.4.1 Available codes

AMSET [134] and ElecTra [132, 133] are two available open-source post-processing codes to compute the charge carrier relaxation times based on first-principles DFT results. The details of these codes can be found in the references. I chose GaAS as a benchmark and assessed our results with the aforementioned codes. Input parameters such as deformation potential and elastic constants were kept the same and the doping concentration was as high as $10^{15} cm^{-3}$ for both n-type and p-type samples. Agreements in magnitude and trend for each mechanism signify that our approach is valid.

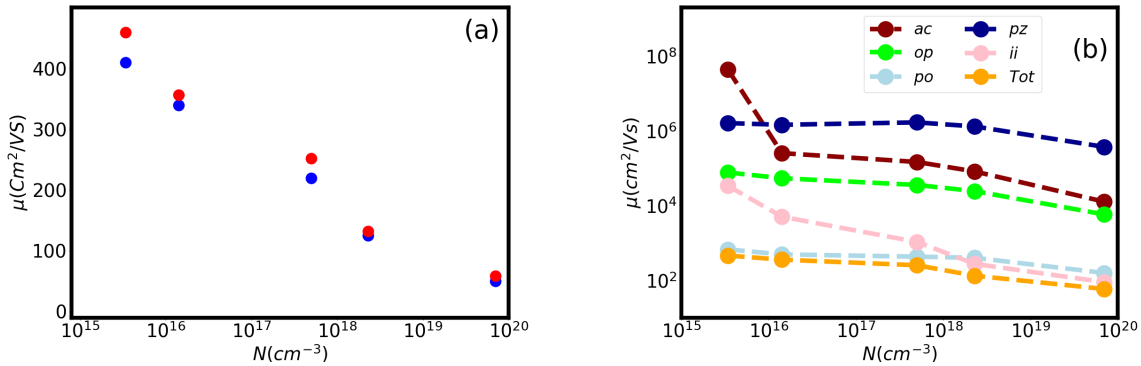

Figure 5.2: (a)The experimental data of hole mobility (blue points) versus our theoretical values (red points) for p-type GaAs in a wide range of doping concentrations. (b) hole mobility of each mechanism solely. The smallest mobility determines the dominant mechanism. ac, pz,op,ii, and po stand for acoustic phonon deformation potential, piezoelectric interaction, optical phonon deformation potential, ionized impurity, and polar optical phonon, respectively. The total scattering rate is abbreviated as Tot.

5.4.2 Experimental data

In addition to the analytical models and already available codes, I reproduced the experimental data of drift mobility and electrical resistivity of several materials in the following section.

5.4.2.1 GaAs

GaAs is a commonly used semiconductor in electronics and its electronic structure derivative properties were well studied. The effect of dopant concentration is shown in Fig 5.2. Our theoretical findings are reasonably close to the experiments [205–209] and the hole mobility decreases as the dopant concentration increases which is expected in semiconductors. Furthermore, the hole mobility caused by each scattering mechanism is plotted in Fig 5.2 from which the dominant scattering mechanism is determined. The smallest mobility prevails over the total mobility and in the case of GaAs, for the lower doping concentrations, smaller than $n_h = 10^{18} cm^{-3}$, the polar optical phonon mechanism dominates that is consistent with the literature [210–212], while for the higher concentrations the ionized impurity scattering controls charge transport as it was reported in the previous works [213–215]. Moreover, the matrix elements of scattering mechanisms depend on temperature, and at different temperatures, the scattering mechanism will change. Such changes for each scattering mechanism rely on the matrix element formulation,e.g. the acoustic phonon deformation potential scat-

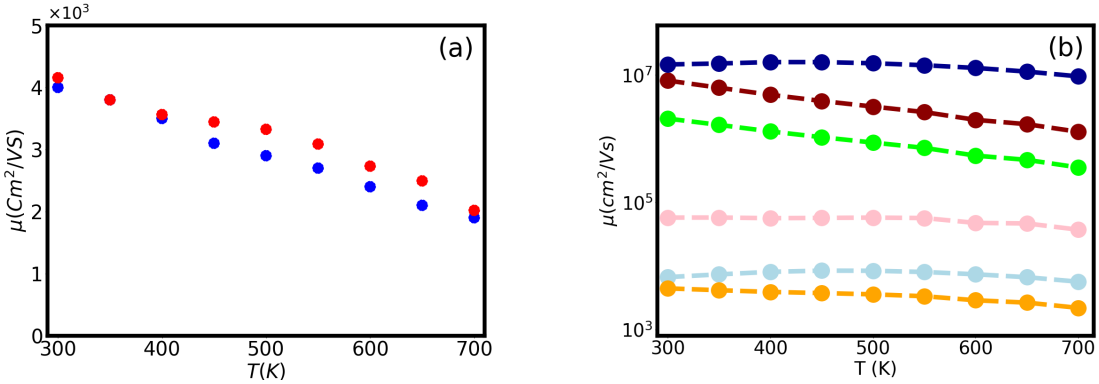

Figure 5.3: (a)The measured electron mobility [217–219] (blue points) versus our theory (red points) for n-type GaAs with a donor concentration of $N_D = 10^{17} cm^{-3}$. (b) drift mobility of each mechanism. Similarly, the smallest drift mobility controls total mobility. Colors correspond to Fig. 5.2

tering rate is linearly proportional to the inverse of temperature. Fig 5.3 exhibits a close reproduction of the electron mobility of n-doped GaAs from room temperature to 700 K. The scattering rates due to each mechanism vary versus temperature, although, for temperatures from 300 K to 700 K, polar optical phonon remains the dominant mechanism which has no conflicts with the previous articles [216].

5.4.2.2 GaN

Our approach was tested on Wurtzite GaN as a non-cubic structure. Highly doped samples, ranging from $10^{17} cm^{-3}$ to over $10^{20} cm^{-3}$, were investigated to ensure that our approach detects the role of ionized impurity scattering. In addition to the reproduction of the experimental data, this range of doping ionized impurity scattering appeared to control electron mobility which is consistent with the earlier studies [220]. Besides, the ionized impurity scattering remains the dominant mechanism even at higher temperatures (see 5.5).

5.4.2.3 InP

Deformation potential scattering mechanisms turn critical in some semiconductors. I choose to examine the scattering rates of InP as deformation potential scattering was found to be the dominant mechanism [224]. Indium phosphide is a frequently used semiconductor in transistors for which charge carrier is of great importance. The acoustic phonon deformation potential of InP was reported as large as 21 eV [224, 225]. Such a large value of acoustic

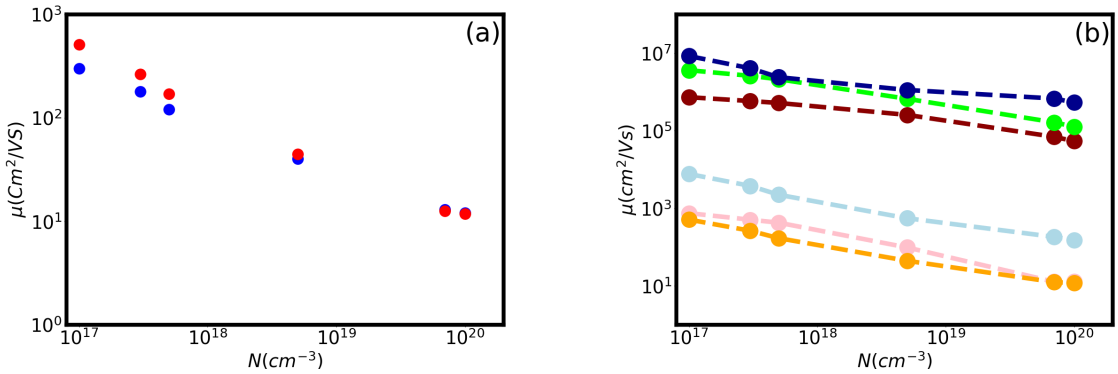

Figure 5.4: (a)Electron mobility of n-type Wurtzite GaN: experiments [220, 221] (blue points) and theory (red points) for highly doped samples. (b) contribution of each mechanism to electron mobility.

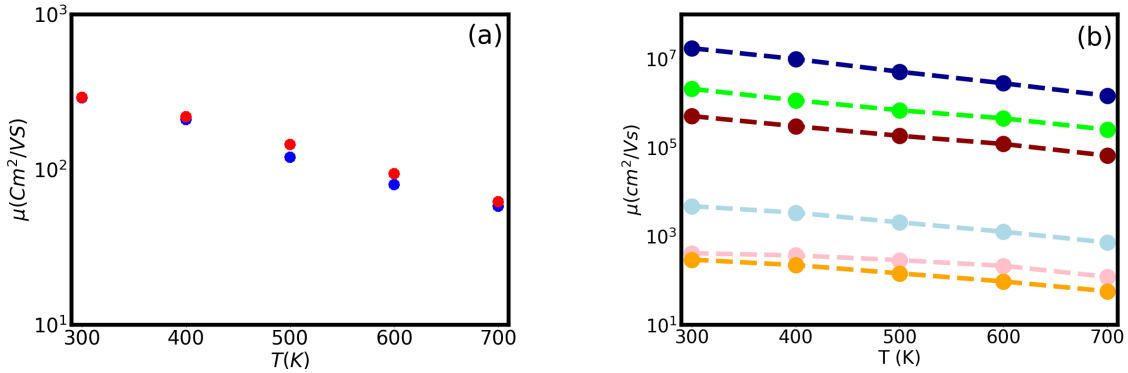

Figure 5.5: (a)Electron mobility for n-type GaN taken from the experiments [222, 223] (blue points) along with our theoretical findings (red points) doping concentrations is $N_D = 5 \times 10^{17}$. (b) ionized impurity scattering is the far most dominant mechanism.

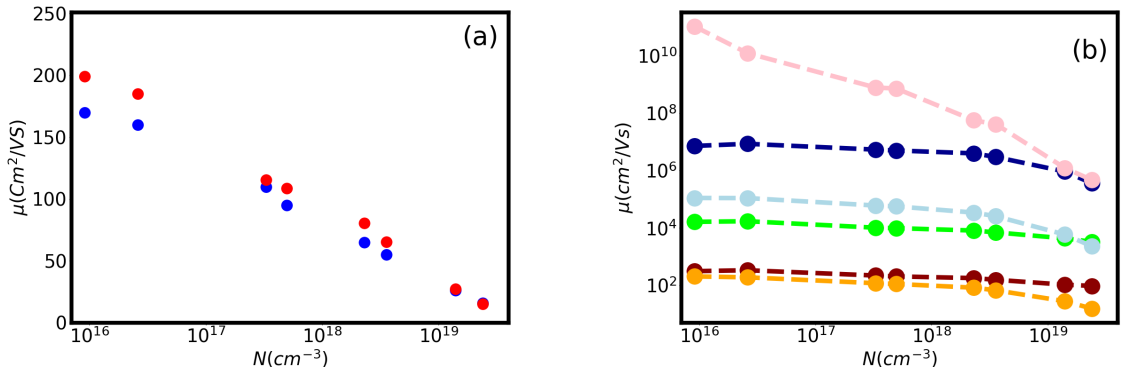

Figure 5.6: (a)Electron mobility of n-type InP: experiments [220, 221] (blue points) and theory (red points) for highly doped samples. (b) contribution of each mechanism to electron mobility.

deformation potential makes the acoustic deformation potential mechanism critically contribute to electron mobility. Our method was applied to InP and the theoretical predictions emerged to be fairly close to the experiments for a broad range of doping concentrations. On the other hand, the results show that the acoustic phonon deformation potential scattering controls electron mobility in InP 5.6.

5.4.2.4 SiC

Silicon carbide (SiC) has been a replacement for silicon in electronics because of its wide band gap, great thermal conductivity, and large breakdown voltage. Interestingly, SiC has several allotropes, namely cubic phase (3C) and hexagonal structures (4H,6H). 4H-SiC was observed to possess a greater mobility [226]. Apart from the fact that the unit cell is relatively larger than the commonly used semiconductor such as Si, Ge, and GaAs and I needed to test my code on a bigger unit cell containing more atoms. Subsequently, the electronic structure comprises more bands and features more complexity compared to Si or GaAs.

The theoretical electron mobility of n-doped samples is in agreement with the experiments and decreases versus doping concentrations. Acoustic phonon deformation potential exhibits high scattering rates and plays a key role in total mobility. This behavior is not strange and was seen in SiC before [227, 228]. Fig 5.9 portrays electron/hole mobility values obtained by our approach for several semiconductors variously doped at the temperature of 300 K. The dotted line indicates the deviation between theory and experiments. Our theory effectively reproduces experimental data (μ_{EXP}) for doped semiconductors whether they are

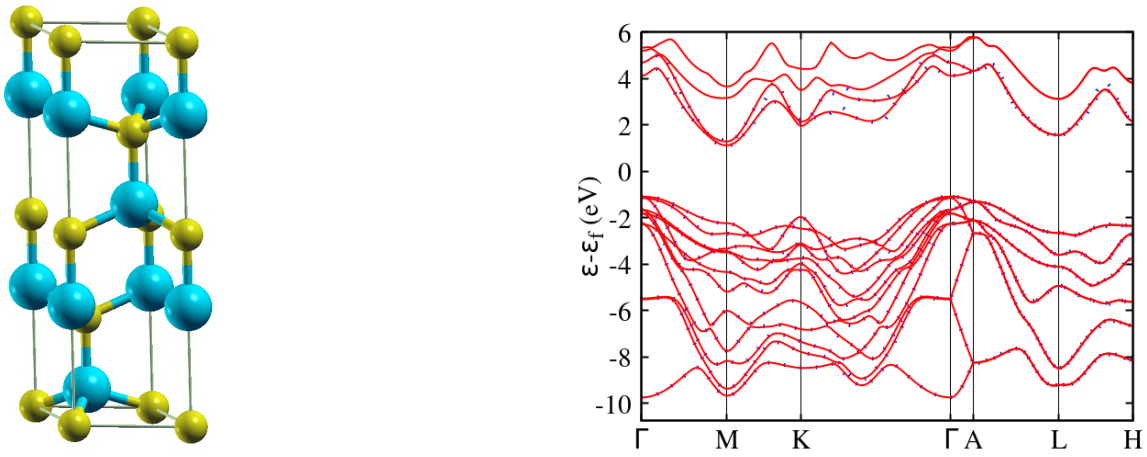

Figure 5.7: 4H Silicon Carbide crystal structure. The cubic unit cell contains 8 atoms along with the electronic structure. Red dash lines and blue dots display DFT and wannierized band structures, respectively.

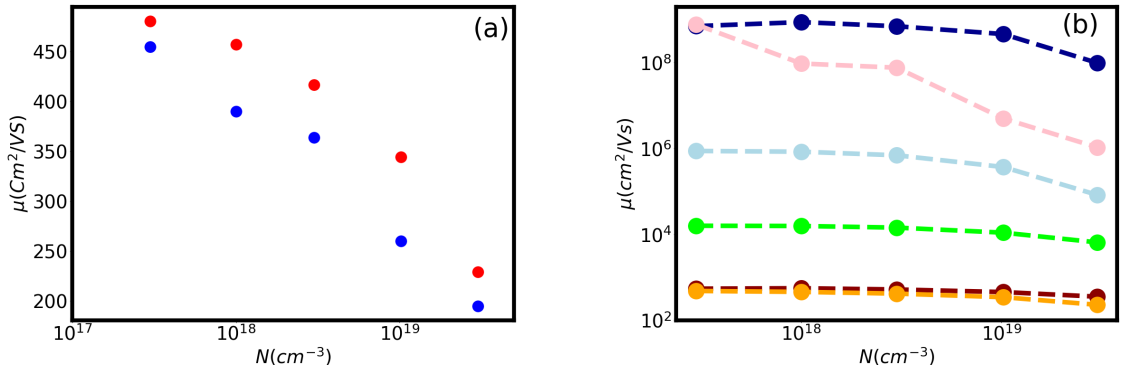

Figure 5.8: (a)Electron mobility for n-type 4H-SiC taken from the experiments [222, 223] (blue points) along with our theoretical findings (red points) (b) Acoustic phonon deformation potential exhibits the lowest mobility [228]

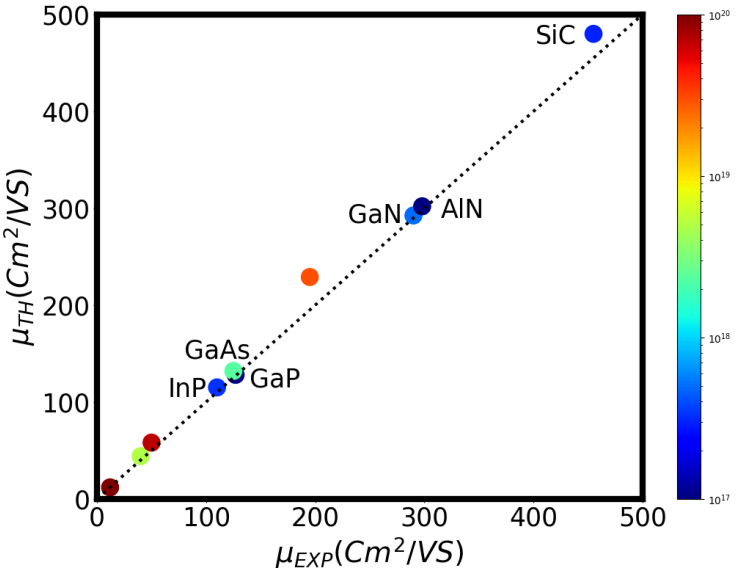

Figure 5.9: Theoretical Electron/hole mobility (y-axis) for some materials in a broad range of doping concentration (color bar) at room temperature. The corresponding experimental values are shown on the horizontal axis.

narrow band gap, e.g. InP, or large band gap, e.g. GaN, semiconductors. However, due to assumptions made in our formalism, our theoretical results are not in agreement with the experiments for intrinsic samples.

5.5 conclusion

In this chapter, I proposed an efficient approach to assess the charge carrier relaxation time in solids due to various mechanisms with the assumption of isotropic and elastic collisions using first-principles Density Functional theory calculations. In order to validate the method, not only our results were compared to the other codes, but some experimental data on electrical resistivity and mobility were reproduced. A remarkable accuracy was observed in a moderate computational cost. This approach was found to yield reasonable predictions of mobility for doped semiconductors, although, the assumptions are not accurate for intrinsic samples with a low concentration of dopants. This method promotes the materials discovery and prediction of electronic materials in a wide range of applications.

CHAPTER VI

Anomalous Nernst Effect

6.1 Introduction

Thermoelectric (TE) modules are two-terminal devices and are analyzed through the Seebeck effect. In a TE module, the temperature difference between two ends gives rise to an electric field in the same direction as the temperature gradient. Such configuration might be an obstacle for some applications due to the necessity of a heat reservoir and as a result, low thermal conductivity but high electrical conductivity are simultaneously required [229]. Multi-terminal modules emerged as a solution by separating the heat reservoir and the electric circuit [230], specifically, the Nernst modules have recently caught attention. In a Nernst device, in addition to a temperature gradient, a magnetic field needs to be present and the developed voltage is perpendicular to the plane of the temperature gradient and magnetic field. Due to the lack of need for oppositely charged samples, Nernst modules are simpler to integrate compared to TE devices [229].

In the previous sections III, IV I introduced the ordinary Nernst effect which requires applying an external magnetic field. Materials that possess non-zero Berry curvature have the advantage of a fictitious magnetic field and upon applying a temperature gradient a Nernst voltage will be generated. This phenomenon is recognized as the anomalous Nernst effect (ANE) and the developed voltage is named anomalous Nernst coefficient (ANC). Furthermore, ANC was observed to grow rapidly in low magnetic fields while the changes of the ordinary Nernst coefficient are negligible in small magnetic fields [231], therefore ANE can potentially be superior to yield a large Nernst power factor in low magnetic fields.

ANC is not directly proportional to the magnetic momentum of the material, in fact, it is derived from Berry curvature [$\Omega_n(k)$] of the system which is defined as the Berry phase (Φ) per unit area [232]. In a sense, ANC is the summation of Berry curvature values around the

Fermi level [233], consequently, materials with large Berry curvatures could be promising candidates for Nernst applications. ANC was reported to considerably grow in topological materials by tailoring the Berry curvature [234] such as external perturbations to split band degeneracy [235] and centrosymmetry breaking through strain [236]. Besides, the crossing of non-degenerate flat bands will generate nontrivial topological states and the ANE will increase [237]. In a similar physics, significantly large values of ANC were measured for $Fe_3Ga(Al)$ [238] and Co_2MnGa [239] due to the Lifshitz transition which is an abrupt change in the topology of a Fermi surface.

Iron-based ferromagnetic compounds have emerged as promising candidates for ANE applications due to their topological states and magnetic moments [240]. Among those, the binary structures based on the kagome lattice have got great attention due to itinerant electrons caused by the interference of hopping ways in the vicinity of the kagome bracket. More interestingly, a kagome lattice can concurrently contain topologically protected bands and flat bands [241]. Fe_3Sn with a hexagonal crystal structure was observed not only to be a bilayer kagome magnet but also to form a nodal plane. The kagome lattice is formed by Fe atoms and Sn atoms sit at the center of it and the second layer is rotated by $\pi/3$. Experiments showed that AHC and ANC of Fe_3Sn are significant at room temperature and may be tuned up as big as $3\mu V/K$.

Herein, I reproduced the experimental data of ANC for Fe_3Sn in a wide range of temperatures using first-principles density functional calculations with the basis sets of maximally-localized Wannier functions. Our approach does not assume any specific types of band dispersion and does not require any fitting parameters. After replication of the electrical resistivity and the Seebeck coefficient, the anomalous Nernst coefficient was computed at a reasonable computational cost and our theoretical results emerged fairly close to the experiments.

6.2 Theory

6.2.1 Equation of motion

Electrons are often described as wave packets constructed from the Bloch waves $\Psi_{nk}(r) = e^{ik.r}u_{n,k}(r)$. Semi-classical equations of motion for materials with nonzero magnetization

require a correction of weighting to the wave packet [242].

$$W_{k_c,r_c}(r,t) = \sum_k a_k(k_c,t)\Psi_{nk}(r) \tag{6.1}$$

The wave packet is centered at r_c so that $r_c = \langle W_{k_c,r_c}|r|W_{k_c,r_c}\rangle$, and zero order in the magnetic field only, it demanded that $a_k(k_c,t) = |a_k(k_c,t)|e^{i(k-k_c).A_n(k_c)-ik.r_c}$, in which $A_n(k)$ is the Berry connection $A_n(k) = i\langle u_{nk}|\nabla_k|u_{nk}\rangle$ [232, 242].

$$A_n(k) = i\int u^*_{n,k}(r)\nabla_k u_{n,k}(r)d^3r \tag{6.2}$$

More importantly, the curl of the Berry connection is called Berry curvature [232].

$$\Omega^B_n(k) = \nabla_k \times A_n(k) = i\int \nabla_k u^*_{n,k}(r) \times \nabla_k u_{n,k}(r)d^3r \tag{6.3}$$

Berry curvature is the quantity that rectifies the equation of motion. Berry curvature and the corresponding anomalous velocity are associated with the nth-band properties of the periodic part of the wave function. One may annotate the Berry curvature as a second-rank anti-symmetric tensor:

$$\begin{aligned} \Omega^B_{n,l} &= \epsilon_{ijl}\Omega^B_{n,ij}(k) \\ \Omega^B_{n,ij}(k) &= -2\,\mathrm{Im}\Big\langle \frac{\partial u_{n,k}}{\partial k_i}|\frac{\partial u_{n,k}}{\partial k_j}\Big\rangle \end{aligned} \tag{6.4}$$

The total Berry curvature at a given wave-vector is accomplished by the summation of Berry curvature over all bands weighted by the occupation of each state.

$$\Omega^B_{ij}(k) = \sum f_n(k)\Omega^B_{n,ij}(k) \tag{6.5}$$

Anomalous Hall effect may be observed in the crystal structure with broken time-reversal symmetry and non-zero Berry curvature. Under these conditions, the equation of motion for an electron wave packet is reformulated.

$$\dot{r} = \frac{\partial\varepsilon(n,k)}{\hbar\partial k} + \dot{k} \times \Omega^B_k \tag{6.6}$$

Additionally, the presence of magnetic and electric fields affects the motion of electrons.

$$\dot{k} = \frac{q}{\hbar}E + \frac{q\dot{r}}{\hbar} \times H \tag{6.7}$$

Solving the above equations gives us $\dot{r}$ and $\dot{k}$.

$$\begin{aligned} \dot{r} &= \Big(1 + (H \cdot \Omega_k^B)q/\hbar\Big)^{-1}\Big(\nu_k + q/\hbar(E \times \Omega_k^B + \nu_k \cdot \Omega_k^B H)\Big) \\ \dot{k} &= \frac{q}{\hbar}\Big(1 + (H \cdot \Omega_k^B)q/\hbar\Big)^{-1}\Big(E + \frac{\nu_k}{\hbar} \times H + \frac{q}{\hbar}(E \cdot H)\Omega_k^B\Big) \end{aligned} \tag{6.8}$$

For the sake of simplicity I show $1 + (H \cdot \Omega_k^B)q/\hbar$ by $\mathcal{D}(H, k)$. Having changes of location and wave vector I could solve the semi-classical Boltzmann equations within relaxation time approximation.

$$(\dot{k} \cdot \nabla_k + \dot{r} \cdot \nabla_r) f_k = \frac{f_k^0 - f_k}{\tau} \tag{6.9}$$

The deviation of the distribution function from the equilibrium is shown as f_k^1=$f_k - f_k^0$. After replacing the equations for $\dot{k}$ and $\dot{r}$ (6.8) in BTE (6.9) an equation for the distribution function is formed.

$$\begin{aligned} &\frac{q}{\hbar}\Big(E + \frac{\nu}{\hbar} \times H + \frac{q}{\hbar}(E \cdot H)\Omega_k^B\Big) \cdot \nabla_k f_k^1 + \Big(\nu + q/\hbar(E \times \Omega_k^B + \nu \cdot \Omega_k^B H)\Big) \cdot \nabla_r f_k^1 = -\frac{\mathcal{D} f_k^1}{\tau} \\ &\frac{q}{\hbar}\Big(E + \frac{\nu}{\hbar} \times H\Big) \cdot \nabla_k f_k^1 + \frac{q^2}{\hbar^2}\Big((E \cdot H)\Omega_k^B\Big) \cdot \nabla_k f_k^1 + \nu \cdot \nabla_r f_k^1 + \Big(q/\hbar(E \times \Omega_k^B + \nu \cdot \Omega_k^B H)\Big) \cdot \nabla_r f_k^1 = -\frac{\mathcal{D} f_k^1}{\tau} \end{aligned} \tag{6.10}$$

The gradient with respect to the wave vector in Eq. 6.10 could be turned into gradients with respect to energy and temperature.

$$\frac{q}{\hbar^2}\nu \times H \cdot \nabla_k f_k^l + \frac{q}{\hbar}\nu \cdot E\frac{\partial f^0}{\partial \varepsilon} + \nu \cdot T\nabla\Big(\frac{\varepsilon - \mu}{T}\Big)\frac{\partial f^0}{\partial \varepsilon} + \frac{q^2}{\hbar^2}(E \cdot H)\Omega_k^B \nabla_k f_k^0 + \frac{q}{\hbar}(E \times \Omega_B^k + \nu \cdot \Omega_B^k H)\nabla_r f_k^1 = -\frac{\mathcal{D} f_k^1}{\tau} \tag{6.11}$$

The first three terms in Eq. 6.11 describe the ordinary Nernst effect and are explained in Ref [130]. The last two terms illustrate the anomalous transport and accordingly, anomalous Hall conductivity (σ^a) and anomalous Nernst conductivity (α^a) will be defined.

$$\begin{aligned} \sigma_{ij}^a &= \frac{q^2}{\hbar}\int \Omega_{ij}^B(k) f_k d^3k \\ \alpha_{ij}^a &= \frac{k_B q}{\hbar}\int \Omega_{ij}^B(k) S_k d^3k \end{aligned} \tag{6.12}$$

Where $S_k = -f_k \ln f_k - (1 - f_k)\ln(1 - f_k)$ known as the entropy density. With the help of the Fermi-Dirac distribution function and integration by parts, a simpler form for anomalous Nernst conductivity can be extracted.

$$\alpha_{ij}^{a}(\mu) = -\frac{1}{q}\int(-\frac{\partial f}{\partial \varepsilon})\frac{\varepsilon - \mu}{T}\sigma_{ij}^{a}(\varepsilon)d\varepsilon \tag{6.13}$$

The above equations (Eq. 6.10-6.12) pronounce that the Berry curvature Ω^B is the key in anomalous transport. It was discussed that the Berry curvature is an antisymmetric tensor with zero diagonal components, so will be the anomalous Hall and Nernst conductivities. The total response functions is the summation of ordinary(o) and anomalous (a) parts,e.g. $[\sigma^t] = [\sigma^o] + [\sigma^a]$.

Similar to the ordinary Nernst effect (Eq. 8.4), response functions are achieved and the total Nernst coefficient matrix is $N = [\sigma^t]^{-1}[\alpha^t]$. Calculation of Berry curvature is implemented in Wannier90 package and I developed a post-process code to establish the anomalous response functions (σ^a and α^a). The ordinary Nernst coefficient was thoroughly discussed in the previous chapter IV, however, the matrix elements of scattering mechanisms are different in metals and semimetals.

6.2.2 Scattering mechanisms in metals

In a metal, an electron is likely to collide with phonons, impurities, or other electrons. Ziman [188] expressed that at elevated temperatures quantization of lattice vibrations becomes irrelevant and the scattering will be proportional to the fluctuation amplitude of the ions, thus, the electrical resistivity will linearly grow with temperature ($\rho_L \propto T$). On the contrary, at temperatures lower than the Debye temperature, the lattice vibration modes have to be counted. Due to momentum conservation and the small changes in wave vector over all phonons, the scattering angle will be minute. Ziman proposed that at such temperatures the electrical resistivity changes intensely with temperature ($\rho_L \propto T^5$), although, he found the electrical resistivity due to impurities in metal is independent of temperature. In the next sections, I assume the pure metallic Fe_3Sn and formulated the electron-electron and electron-phonon scattering.

6.2.2.1 Electron-electron scattering

The interaction between electrons in metals could be relatively considerable, therefore, one may infer that electrons collide with each other numerously, but because of Pauli's exclusion principle, the probability of electron-electron (e-e) collision is suppressed as low. According to the Born approximation, e-e scattering rate from the initial states of k_1 and k_2 to the final states of k_1' and k_2' is stated by:

$$P(k_1, k_2, k_1', k_2') = \frac{2\pi}{\hbar}\Big| < n', k'|H'|n, k > \Big|^2 \delta\big[\varepsilon(n_1', k_1') + \varepsilon(n_2', k_2') - \varepsilon(n_1, k_1) - \varepsilon(n_2, k_2)\big] \tag{6.14}$$

Based on the Fermi liquid theory [243], Suzuki [244] proved that the e-e scattering is linearly related to the Fermi energy.

$$\frac{1}{\tau_{e-e}} = \frac{(k_B T)^2}{\hbar \varepsilon_F} \mathcal{F}(0) \tag{6.15}$$

Where $\mathcal{F}$ is an integral of the Fermi-Dirac distribution function of two states.

$$\mathcal{F}(\mathbf{t}) = \int_0^\infty \int_0^\infty \frac{1}{1 + e^{u+v-t}} \frac{1}{1 + e^{-u}} \frac{1}{1 + e^{-v}} du dv \tag{6.16}$$

If $0 < t < 1$ $\mathcal{F}$ has a finite value, and specifically $\mathbf{F}(0) = \frac{\pi^2}{24}$.

6.2.2.2 Electron-phonon scattering

Kabanov [245] began with a non-thermal relaxation of the electron distribution function and formulated electron-phonon (e-ph) relaxation by the collision integral.

$$\begin{aligned} \frac{\partial f}{\partial t} = 2\pi \int \int Q(\omega, \varepsilon, \varepsilon') \Big[& \delta(\varepsilon - \varepsilon' - \hbar\omega)\big[(f_{\varepsilon'} - f_\varepsilon) N_\omega - f_\varepsilon (1 - f_{\varepsilon'})\big] + \\ & \delta(\varepsilon - \varepsilon' + \hbar\omega)\big[(f_{\varepsilon'} - f_\varepsilon) N_\omega + f_\varepsilon' (1 - f_{\varepsilon')}\big]\Big] d\omega d\varepsilon' \end{aligned} \tag{6.17}$$

Where $Q(\omega, \varepsilon, \varepsilon')$ is the e-ph spectral function.

$$Q(\omega, \varepsilon, \varepsilon') = \frac{1}{\hbar g(\varepsilon)} \sum_{k,q} M^2(q) \delta(\varepsilon_{k-q} - \varepsilon') \delta(\varepsilon_k - \varepsilon) \delta(\omega_q - \omega) \tag{6.18}$$

After doing some algebra, the e-ph relaxation time in metals is obtained as follows:

$$\frac{1}{\tau_{e-ph}(\varepsilon)} = \frac{2\pi k_B T}{\hbar} \int_0^{\omega_{max}} \alpha^2 F(\omega) \Big[\frac{1}{\sinh(\omega/2)\cosh(\omega/2)} + \frac{\sinh^2(\varepsilon/2)\tanh(\omega/2)}{\cosh(\frac{\omega+\varepsilon}{2})\cosh(\frac{\omega-\varepsilon}{2})} \Big] d\omega \tag{6.19}$$

In which ω_{max} is the maximum phonon frequency and $\alpha^2 F$ is the Eliashberg function that is frequently used in the theory of superconductivity [246, 247]. The calculation of the Eliashberg function is implemented in Quantum Espresso by averaging the electron-phonon coupling strength (λ) associated with a phonon mode of ν and wave vector of q in the Brillouin zone.

$$\alpha^2 F(\omega) = \frac{1}{2} \sum_{\nu} \int_{BZ} \frac{dq}{V} \omega_{q\nu} \lambda_{q\nu} \delta(\omega - \omega_{q\nu}) \tag{6.20}$$

6.3 DFT calculations

Fe_3Sn crystallizes in the hexagonal structure (Fig 6.1). I start with the experimental lattice constants (a=5.460 and c=4.330 A^0) and relax the atomic position to reach the lowest energy. Fe_3Sn is reported to be a magnetic compound with an atomic magnetic moment of 2.47 μ_B. Local density approximation turned out to predict the magnetic moment incorrectly (3.9 μ_B), thus, I employed Hubbard U method [248] to correct the DFT results. Its real-space second quantization formalism is perfectly suited to describe electron localization on atomic orbitals. The simplest form is a one-band system whose Hubbard Hamiltonian is expressed as below:

$$H_{Hub} = t \sum_{<\alpha,\beta>,\lambda} \left(c^+_{\alpha,\lambda} c^-_{\beta,\lambda} + c^+_{\beta,\lambda} c^-_{\alpha,\lambda} \right) + U \sum_{\alpha} n_{\alpha,\uparrow} n_{\alpha,\downarrow} \tag{6.21}$$

In which $< \alpha, \beta >$ designates the nearest-neighbor atomic sites, $c^-_{\alpha,\lambda}$, $c^+_{\alpha,\lambda}$, and $n_{\alpha,\lambda}$ indicate electronic annihilation, creation, and number operators for electrons of spin λ and on-site α. Lastly, t is the hopping amplitude which is determined by the localization level [249]. In case of the strong localization, the Coulomb repulsion between electrons on the same atom is estimated by a term "U" that is linked to the product of the occupation numbers of atomic. In DFT packages, this method is known as LDA(GGA)+U and is a convincing approach to enhance the accuracy of DFT electronic structure results. The method has been successful to capture the electronic localization in d and f orbitals [250, 251]. Within LDA+U the total

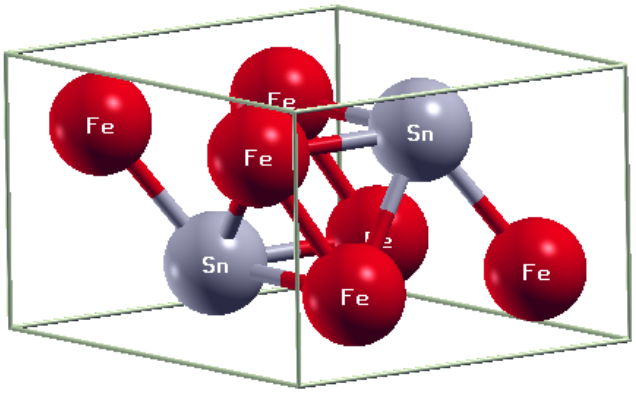

Figure 6.1: Hexagonal unit cell of Fe_3Sn with 6 Fe atoms and 2 Sn atoms.

energy of a structure is corrected as below:

$$\mathcal{E}_{LDA+U} = \mathcal{E}_{LDA} + \mathcal{E}_{Hub} - \mathcal{E}_{d} \tag{6.22}$$

Where $\mathcal{E}_d$ removes the double counting the overlap between DFT and Hubbard energy. LDA+U method is implemented in Quantum Espresso with the linear-response method of Cococcioni and de Gironcoli [251]. In order to procure a fine interpolation of the band structure, the electronic structure was wannierized and calculation of Berry curvature and effective mass tensor were carried out on the MLWF basis sets using Wannier90 package [40, 130]. It is worth mentioning that the convergence of Berry curvature and the effective mass tensors occurred at nonidentical interpolation grids. Electron-phonon coupling constant and Eliashberg function is implemented in Quantum Espresso package [115]. Having Eliashberg function and energy dispersion I could evaluate the relaxation time. Lastly, O sum the ordinary and anomalous counterparts of the transport distribution function within relaxation time approximation and accomplish the anomalous Nernst coefficient.

6.4 Results

Our simulation needs to be initially authenticate by verifying the magnetic moment. With a U value of 2.4, I obtained the atomic magnetic moment of 2.56 μ_B. Additionally, at the low temperatures, where the magnon contribution becomes negligible, the specific heat is attributed to the contributions of electrons and lattice vibrations and it is clarified as $C = \gamma T + \beta T^3$. γ coefficient can be earned from the number of states by $\gamma = \frac{\pi^2}{3} k_B g(\varepsilon)$. Fig 6.2

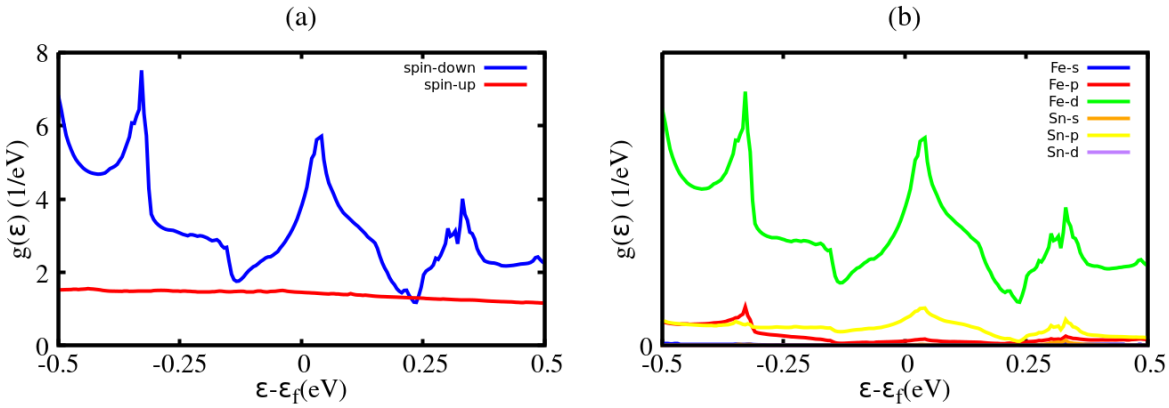

Figure 6.2: Total density of states of bulk Fe_3Sn for both spins (a). Projected density of states for s,p,and d orbitals of Fe spin-down and Sn (b).

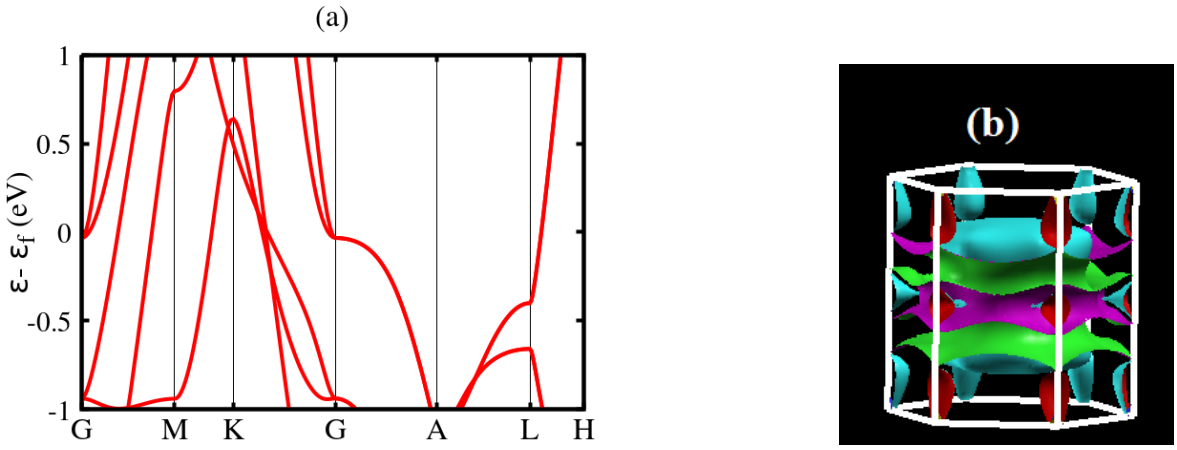

Figure 6.3: LDA+U band structure of bulk Fe_3Sn (a). Merged Fermi surface of three spin down bands crossing the Fermi level (b).

(a) shows the density of states of bulk Fe_3Sn including spin-up and spin-down states. The measurements of specific heat gives γ=17.1 mJ/mol K^2 [252] while the LDA+U results bear a γ=12.46 mJ/mol K^2. It points out the effective mass of electrons is improved 26 % due to the correlation effect. All DFT calculations were continued with the U value of 2.4. Fig 6.2 (a) shows the majority of states near the Fermi level are directed spin-up, more importantly, the d-orbitals of iron have the main contribution to those states which generates a magnetic moment. I then proceeded with the band structure calculation of Fe_3Sn (Fig. 6.3(a)). It is found to be a metallic system which is consistent with the previous studies [253]. Fig 6.3(b) displays the Fermi surface of spin-down states near the Fermi level which marks the metallic nature of Fe_3Sn. Since the electron-phonon coupling constant ensues from summation over both electrons and phonons wave vectors, electron eigenvalues and phonon dispersion are

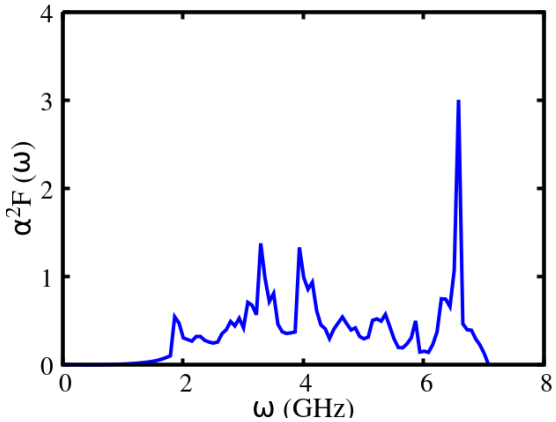

Figure 6.4: The Eliashberg function ($\alpha^2 F$) of bulk Fe_3Sn versus phonon angular frequency.

required to attain the electron-phonon coupling constant. Having electron-phonon coupling constant I could move on to the Eliashberg function (Fig 6.4) and finally assess the electron-phonon relaxation time through Eq. 6.17. The total relaxation time of Fe_3Sn was found to be in the order of 10^{-15}s which is reasonably close to the relaxation time reported for iron [254]. The resulted relaxation times were then coupled with the transport distribution function to probe the transport properties namely electrical resistivity and the Seebeck coefficient.

Chen et.al. [255] measured the electrical resistivity and Seebeck coefficient of polycrystalline Fe_3Sn. Because of an exceptional number of charge carriers in metals, outstandingly low electrical resistivity is a prominent feature of metals. Withal, electrical resistivity in metals increases versus temperature due to more collisions. Fig 6.5(a) exhibits the electrical resistivity of Fe_3Sn whose order of magnitude is impressively small ($\mu\Omega cm$) and grows with temperature. Electrical resistivity is more sensitive to carrier scattering than the Seebeck coefficient and since in a polycrystalline sample there are extra scattering mechanisms such as grain boundary and defects, the theoretical electrical resistivity is almost twice smaller than the experiments. The theoretical Seebeck coefficient, though, turned out to be favourably matching the experiments which is rooted in the weaker dependence of the Seebeck coefficient to relaxation time. Unlike semiconductors, in metals the Seebeck coefficient increases versus temperature and because of excessively high charge carrier concentration the Seebeck coefficient is smaller (6.5(b)).

Anomalous Nernst and Hall effects are ascribed to the non-zero Berry curvature in momentum space. Anomalous Hall effect renders the integral of the Berry curvature over all the

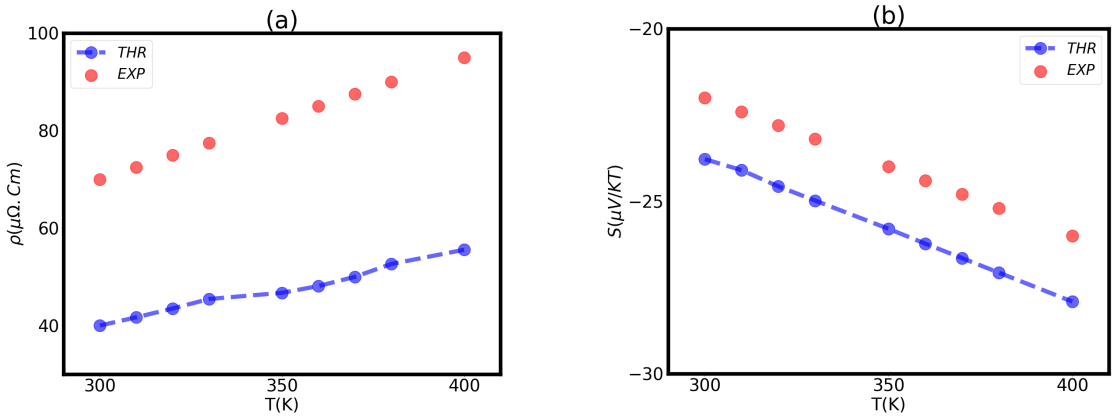

Figure 6.5: The average electrical resistivity (a) and Seebeck coefficient (b) of bulk Fe_3Sn. Red circles are the experiments [252] and dashed line is our theory.

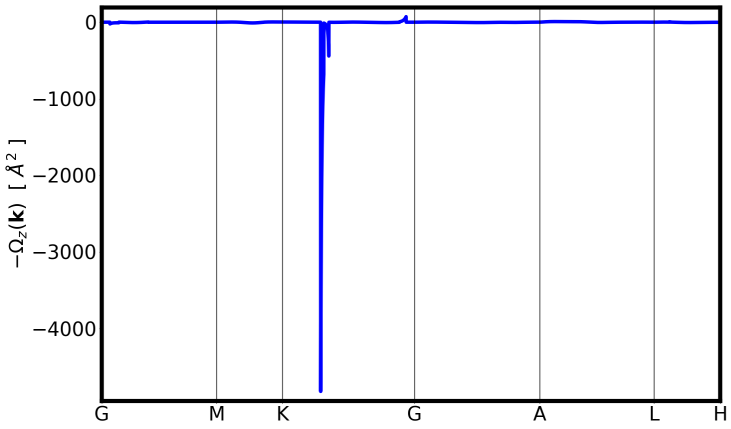

Figure 6.6: The total Berry curvature of bulk Fe_3Sn at the Fermi level in the units of ${}^0A^2$.

occupied bands (Eq. 6.12). Anomalous Nernst conductivity specifies changes of the anomalous Hall conductivity with respect to energy at the Fermi energy. It was found that band crossing enlarges Berry curvature [252]. If the spin orbit coupling is negligible, band degeneracy occurs when two bands with the same spin cross each other. Fig 6.6 shows the total Berry curvature of Fe_3Sn at the Fermi level along the high symmetry points. There is a clear band crossing at the Fermi level along K to G (Fig. 6.3) that triggers the Berry curvature to surge (Fig. 6.6). This behaviour was earlier reported in Iron-based compounds [256, 257].

Having the Berry curvature in reciprocal space I could attain ANC and AHC by Eq. 6.12, 6.13. On the other hand, with the relaxation time obtained for Fe_3Sn the ordinary Nernst transport was achieved. The the ordinary and anomalous parts were then summed according

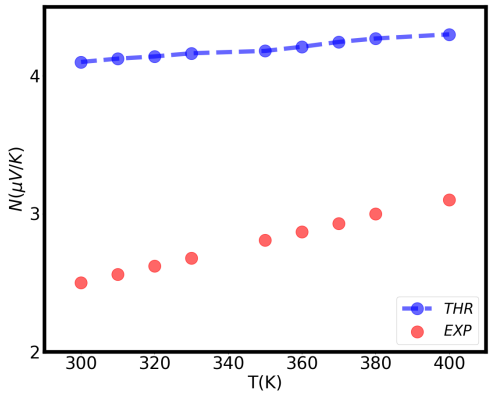

Figure 6.7: The anomalous Nernst coefficient of bulk Fe_3Sn. Red circles are the measurements for a polycrystalline sample [252] and dashed line is our theory carried out for a perfect single crystal.

to Eq. 6.11 to govern the anomalous Nernst coefficient. Our theoretical results appeared to agree with the measurements. Also, the anomalous Nernst coefficient increases as the temperature raises which is justified by Mott relations that expresses the anomalous Nernst coefficient in metals is linearly proportional to temperature [242]. The discrepancies between theory and experiments come from additional scattering mechanisms in the polycrystalline sample.

6.5 Conclusion

Fe_3Sn holds the second largest anomalous Nernst coefficient at room temperature by far. Such a conspicuous anomalous Nernst coefficient at room temperature is attributed to the non-zero Berry curvature improved because of band crossing at the Fermi level. An elevated Curie temperature (760 ^{0}K) enables this compound to function for the anomalous Nernst devices in a wide range of temperature. Iron and tin are non-toxic elements that are copious and economical. I have the LDA results corrected by employing Hubbard method. Furthermore, the electron-phonon and electron-electron scattering rates were analyzed to reproduce the experimental electrical resistivity and the Seebeck coefficient. Finally, the anomalous Nernst coefficient was calculated and compared to the experimental measurements. I adamantly declare that our approach is with the DFT framework, hence, our approach is not applicable to strongly correlated systems.

CHAPTER VII

Conclusions and future works

In this dissertation, continuing the work of Markov et al., I studied semimetals as an effective choice for thermoelectric modules. Not only is the intrinsic carrier concentration strikingly high in semimetals, but the Seebeck coefficient could also be significantly large in the case of the band asymmetry, e.g. heavy holes and light electrons.

Moreover, I developed an approach to calculate the thermomagnetic properties of materials using first-principles density functional theory calculations. In order to establish a thorough understanding of the Nernst effect I began with the constant relaxation time approximation and had our results compared to the analytical models. I then proceeded to go beyond the constant relaxation time approximation by computing the scattering rates. Our approach was then authenticated by comparing to the experimental data reported in the literature. Our code can pave the way for discovery of the promising candidate for the Nernst effect-based applications such as cryogenic cooling, radiation detector, and thermopiles.

Furthermore, I found that the mobility (effective mass) plays a key role to accomplish a high Nernst coefficient as it was observed in the topological Dirac semimetals. This is consistent with previously established theories. Therefore, materials with light effective mass values are good candidates to achieve a high thermomagnetic power factor.

Lastly, I studied bulk Fe_3Sn which holds the second largest anomalous Nernst coefficient at room temperature. The electron localization and on-site repulsion effects were tackled by the Hubbard method. Electron-phonon and electron-electron scattering rates in the Fe_3Sn metallic system were evaluated and the theoretical electrical resistivity and the Seebeck coefficient were in agreement with the experiments. Finally, I successfully reproduced the experimental data of the anomalous Nernst coefficient of Fe_3Sn in a range of temperature within the DFT framework.

For the future works, it is suggested to find the materials that poses a relatively small band gap and light effective mass values, e.g. topological Dirac semimetals, and apply the code to predict the possible applications for the Nernst effect-based devices.

CHAPTER VIII

Appendices

8.1 Analytical solution within CRTA

8.1.1 single isotropic parabolic band

For an isotropic parabolic band, energy-wave vector (k) relation is:

$$\varepsilon(k)=\frac{\hbar^2 k^2}{2m^*} \tag{8.1}$$

In such bands velocity and effective mass are identified as:

$$\begin{aligned} \nu(\overrightarrow{k})&=\hbar^{-1}\nabla_{\overrightarrow{k}}\varepsilon_n(\overrightarrow{k})=\frac{\hbar\overrightarrow{k}}{m^*} \\ \frac{\partial^2\varepsilon_n(\overrightarrow{k})}{\partial\overrightarrow{k}^{\,2}}&=\frac{\partial\nu(\overrightarrow{k})}{\partial\overrightarrow{k}}=\frac{\hbar}{m^*} \end{aligned} \tag{8.2}$$

Transformation to spherical coordinates makes integration easier. Additionally, velocities and derivative of velocities for an isotropic spherical energy dispersion are expressed as below:

$$\begin{aligned} \nu_x&=\sqrt{\frac{2\varepsilon}{m}}sin(\theta)cos(\varphi) \\ \nu_y&=\sqrt{\frac{2\varepsilon}{m}}sin(\theta)sin(\varphi) \\ \nu_z&=\sqrt{\frac{2\varepsilon}{m}}cos(\theta) \\ \frac{\partial\nu_i(k)}{\partial k_i}&=\frac{\hbar}{m}\delta_{ij} \end{aligned} \tag{8.3}$$

Where δ_{mj} is the Kronecker delta function. Moreover, The volume element $dV=\frac{dS_n}{|\nabla_k\varepsilon_n|}$ in which $dS_n=\frac{2m\varepsilon}{\hbar^2}sin(\theta)d\theta d\varphi$ and K are the surface element of the n_{th} band and wave vector,

respectively. Such that, Transport distribution function for an isotropic spherical dispersion may be analytically governed by:

$$\Xi_{ij}(\varepsilon)=\frac{q^2\tau(\varepsilon)}{4\pi^3}\int\frac{\nu_i\nu_j ds(\varepsilon)}{|\nabla_k\varepsilon|} \tag{8.4}$$

I analyze (8.4) for two cases, whether in-plane (i=j) or cross-plane ($i \neq j$). Keep in mind for an isotropic spherical band dispersion Ξ_{ij}=Ξ_{ji} and Ξ_{xx}=Ξ_{yy}=Ξ_{zz}

$$\begin{aligned}
\Xi_{ii}&=\frac{q^2\tau}{4\pi^3}\int\frac{\nu_i\nu_i ds}{|\nabla_k\varepsilon|}\\
&=\frac{q^2\tau}{4\pi^3}\int\frac{2\varepsilon}{m}sin^2(\theta)cos^2(\varphi)\frac{1}{\hbar\sqrt{2\varepsilon/m}}\frac{2m\varepsilon}{\hbar^2}sin\theta d\theta d\varphi\\
&=\frac{q^2\tau}{4\pi^3}\int_0^{2\pi}\int_0^{\pi}\frac{4\varepsilon^2 m\sqrt{m}}{\hbar^3 m\sqrt{2\varepsilon}}sin^3(\theta)cos^2(\varphi)d\theta d\varphi\\
&=\frac{q^2\tau\varepsilon\sqrt{m\varepsilon}}{\pi^3\hbar^3\sqrt{2}}\frac{4\pi}{3}=\frac{2\tau q^2\varepsilon\sqrt{2m\varepsilon}}{3\hbar^3\pi^2}
\end{aligned} \tag{8.5}$$

It is observed that the in-plane transport distribution function is proportional to $\varepsilon\sqrt{\varepsilon}$, therefore, in-plane transport coefficients are non-zero. In contrast, cross-plane transport coefficients are zero.

$$\begin{aligned}
\Xi_{ij}&=\frac{q^2\tau}{4\pi^3}\int\frac{\nu_i\nu_j ds}{|\nabla_k\varepsilon|}\\
&=\int_0^{2\pi}\int_0^{\pi}\sqrt{\frac{2\varepsilon}{m}}sin(\theta)cos(\varphi)\sqrt{\frac{2\varepsilon}{m}}sin(\theta)sin(\varphi)\sqrt{\frac{m}{2\varepsilon\hbar^2}}\frac{2m\varepsilon}{\hbar^2}sin(\theta)d\theta d\varphi\\
&=\int_0^{2\pi}\int_0^{\pi}\frac{2m\varepsilon\sqrt{2\varepsilon}sin^3(\theta)cos(\varphi)sin(\varphi)}{\hbar^3\sqrt{m}}d\theta d\varphi\\
&=\frac{m\varepsilon\sqrt{2\varepsilon}}{\hbar^3\sqrt{m}}\int_0^{2\pi}\int_0^{\pi}sin^3(\theta)sin(2\varphi)d\theta d\varphi\\
&=\frac{4m\varepsilon\sqrt{2\varepsilon}}{3\hbar^3\sqrt{m}}\int_0^{2\pi}sin(2\varphi)d\varphi\\
&=-\frac{2m\varepsilon\sqrt{2\varepsilon}}{3\hbar^3\sqrt{m}}[cos(2\varphi)]_0^{2\pi}=0
\end{aligned} \tag{8.6}$$

Adiabatic Nernst effect is governed by applying boundary conditions to electric and heat current density equations. For adiabatic Nernst effect, electric current density vector is assumed

to be zero in all directions and there would be no heat current in y and z directions either:

$$\begin{aligned} E_i &= \varphi_{ij}(H) J_j + \alpha_{ij}(H) \partial_j T \\ Q_i &= \pi_{ij}(H) J_j - \kappa_{ij}(H) \partial_j T \end{aligned} \tag{8.7}$$

Inserting conditions of zero electric current (J_y=0) and no temperature gradient in the y-direction ($\partial_y T$) into Eq.(8.7), the isothermal Nernst coefficient (N_T) is obtained by:

$$\begin{aligned} E_y &= \alpha_{yx}(H) \partial_x T \\ N_T &= \frac{E_y}{H_z \partial_x T} = \frac{-\alpha_{yx}(H)}{H_z} \end{aligned} \tag{8.8}$$

The second order transport function (Ξ_{ijk}) is a $3\times3\times3$ tensor corresponding to the directions of electric filed (electric potential filed), temperature gradient, and magnetic filed. Herein, I assume the magnetic field is applied only along c-crystal axis ($\overrightarrow{B}=(0,0,B_z)$) and regarding the fact that $\frac{\partial \nu_i}{\partial k_j}=\frac{\hbar}{m}\delta_{ij}$ then with the help of linear algebra it is cleared out xyz and yxz are the only non-zero components of second order transport function along z-axis. Additionally, mind that for an isotropic band $\frac{\partial \nu_x}{\partial k_x}=\frac{\partial \nu_y}{\partial k_y}$ and $\nu_x=\nu_y=\nu_z$, therefore $\Xi_{xyz}=-\Xi_{yxz}$. Similar to (8.5) and (8.6), herein, I analyze xyz component of the second order transport function.

$$\begin{aligned} \Xi_{xyz} &= \frac{q}{\hbar}\frac{-q^2}{4\pi^3}\int -\nu_x \tau^2 H_z \nu_x \frac{\partial \nu_y}{\partial k_y}\frac{dS_n}{|\nabla_k \varepsilon_n|} \\ &= \frac{q^3\tau^2}{4\pi^3\hbar}\int \frac{2\varepsilon}{m} H_z \frac{2m\varepsilon}{\hbar^2}\frac{\hbar}{m}\frac{\sqrt{m}}{\hbar\sqrt{2\varepsilon}} sin^2(\theta)cos^2(\varphi)sin(\theta)d\theta d\varphi \\ &= \frac{q^3 H_z \tau^2}{4\pi^3\hbar}\int_0^{2\pi}\int_0^{\pi}\frac{2\varepsilon\sqrt{2\varepsilon}}{\hbar^2\sqrt{m}} sin^3(\theta)cos^2(\varphi)d\theta d\varphi \\ &= \frac{q^3 H_z \tau^2}{4\pi^3\hbar}\int_0^{2\pi}\frac{2\varepsilon\sqrt{2\varepsilon}}{\hbar^2\sqrt{m}}\frac{4}{3}cos^2(\varphi)d\varphi \\ &= \frac{q^3 H_z \tau^2}{4\pi^3\hbar}\frac{4\varepsilon\sqrt{2\varepsilon}}{3\hbar^2\sqrt{m}}\int_0^{2\pi}(cos(2\varphi)+1)d\varphi \\ &= \frac{q^3 H_z \tau^2}{4\pi^3\hbar}\frac{4\varepsilon\sqrt{2\varepsilon}}{3\hbar^2\sqrt{m}}\left[\frac{cos(2\varphi)}{2}+\varphi\right]_0^{2\pi} \\ &= \frac{q^3 H_z \tau^2}{4\pi^3\hbar}\frac{4\varepsilon\sqrt{2\varepsilon}}{3\hbar^2\sqrt{m}}2\pi = \frac{2q^3 H_z \tau^2 \varepsilon\sqrt{2\varepsilon}}{3\hbar^3\pi^2\sqrt{m}} \end{aligned} \tag{8.9}$$

At this point, I are able to compute transport coefficients for an isotropic spherical dispersion. In the first step, I need to define the full tensor of transport distribution function under a

magnetic field.

$$
\begin{aligned}
[\Xi_{ij}(H)] &= [\Xi_{ij}] + [\Xi_{ijk}] \\
&= \begin{bmatrix} \Xi_{xx} & 0 & 0 \\ 0 & \Xi_{xx} & 0 \\ 0 & 0 & \Xi_{xx} \end{bmatrix} + \begin{bmatrix} 0 & \Xi_{xyz} & 0 \\ -\Xi_{xyz} & 0 & 0 \\ 0 & 0 & 0 \end{bmatrix}
\end{aligned} \tag{8.10}
$$

Accordingly, transport coefficients including $B_{ij}(H)$ and $\sigma_{ij}(H)$ will be defined. $\alpha_{ij}(H)$ depends on both first and second order transport coefficients as follows:

$$
\begin{aligned}
\alpha_{ij}(H) &= \left[\sigma_{ij}(H)\right]^{-1}\left[B_{ij}(H)\right] \\
\alpha_{ij}(H) &= \left(\begin{bmatrix} \sigma_{xx} & 0 & 0 \\ 0 & \sigma_{xx} & 0 \\ 0 & 0 & \sigma_{xx} \end{bmatrix} + \begin{bmatrix} 0 & \sigma_{xyz} & 0 \\ -\sigma_{xyz} & 0 & 0 \\ 0 & 0 & 0 \end{bmatrix} \right)^{-1} \left(\begin{bmatrix} B_{xx} & 0 & 0 \\ 0 & B_{xx} & 0 \\ 0 & 0 & B_{xx} \end{bmatrix} + \begin{bmatrix} 0 & B_{xyz} & 0 \\ -B_{xyz} & 0 & 0 \\ 0 & 0 & 0 \end{bmatrix} \right) \\
\alpha_{ij}(H) &= \begin{bmatrix} \sigma_{xx} & \sigma_{xyz} & 0 \\ -\sigma_{xyz} & \sigma_{xx} & 0 \\ 0 & 0 & \sigma_{xx} \end{bmatrix}^{-1} \begin{bmatrix} B_{xx} & B_{xyz} & 0 \\ -B_{xyz} & B_{xx} & 0 \\ 0 & 0 & B_{xx} \end{bmatrix} \\
\alpha_{ij}(H) &= \frac{1}{\sigma_{xx}(\sigma_{xx}^2 + \sigma_{xyz}^2)} \begin{bmatrix} \sigma_{xx}^2 & -\sigma_{xx}\sigma_{xyz} & 0 \\ \sigma_{xx}\sigma_{xyz} & \sigma_{xx}^2 & 0 \\ 0 & 0 & \sigma_{xx}^2 + \sigma_{xyz}^2 \end{bmatrix} \begin{bmatrix} B_{xx} & B_{xyz} & 0 \\ -B_{xyz} & B_{xx} & 0 \\ 0 & 0 & B_{xx} \end{bmatrix}
\end{aligned} \tag{8.11}
$$

The isothermal Nernst coefficient is defined as $N_T(H)$.

$$
N_T(H) = -\alpha_{yx}(H) = -\frac{\sigma_{xx}\sigma_{xyz}B_{xx} - \sigma_{xx}^2 B_{xyz}}{\sigma_{xx}(\sigma_{xx}^2 + \sigma_{xyz}^2)} = -\frac{\sigma_{xyz}B_{xx} - \sigma_{xx}B_{xyz}}{\sigma_{xx}^2 + \sigma_{yxz}^2} \tag{8.12}
$$

For a single isotropic spherical single band, $\sigma_{xyz}B_{xx} = \sigma_{xx}\frac{qH\tau}{m}B_{xx} = \sigma_{xx}B_{xyz}$ which causes a zero Nernst coefficient. For a multi-band system though, the Nernst coefficient largely depends on effective mass of each band and it is not necessarily zero. It is noteworthy to add that the transport distribution functions (8.10) are linearly summed over bands, so are the transport coefficients.

8.1.2 Ellipsoidal Bands

In contrast to spherical bands, ellipsoidal bands have various effective masses along each crystal axis. Band energies relate to wave vectors as:

$$\varepsilon(k_x, k_y, k_z)=\frac{\hbar^2}{2}(\frac{k_x^2}{m_x}+\frac{k_y^2}{m_y}+\frac{k_z^2}{m_z}) \tag{8.13}$$

Using the transformation mentioned in the main manuscript, Eq. 8.13 turns to $\varepsilon(k'_x, k'_y, k'_z)=\frac{\hbar^2}{2m'}(k_x'^2+k_y'^2+k_z'^2)$. In the first step, I drive the density of state for such energy dispersion.

$$\begin{aligned}
dk=dk_x dk_y dk_z&=(\sqrt{\frac{m_x}{m'}}dk'_x+\sqrt{\frac{m_y}{m'}}dk'_y+\sqrt{\frac{m_z}{m'}}dk'_z)\\
&=\sqrt{\frac{m_x m_y m_z}{m'^3}}dk'_x dk'_y dk'_z=\sqrt{\frac{m_x m_y m_z}{m'^3}}4\pi k'^2 dk'\\
N(k)dk&=\frac{2\times 4\pi k'^2}{(\frac{2\pi}{l})^3}\sqrt{\frac{m_x m_y m_z}{m'^3}}dk'\\
&=\frac{k'^2 l^3}{\pi^2}\sqrt{\frac{m_x m_y m_z}{m'^3}}dk'\\
g(\varepsilon)=\frac{N(k)}{V}\frac{dk}{d\varepsilon}&=\frac{k'^2}{\pi^2}\sqrt{\frac{m_x m_y m_z}{m'^3}}\frac{dk}{d\varepsilon}=\frac{k'^2}{\pi^2}\sqrt{\frac{m_x m_y m_z}{m'^3}}\frac{\sqrt{2m'}}{2\hbar\sqrt{\varepsilon}}\\
&=\frac{2m'\varepsilon}{\pi^2\hbar^2}\sqrt{\frac{m_x m_y m_z}{m'^3}}\frac{\sqrt{2m'}}{2\hbar\sqrt{\varepsilon}}=\frac{\sqrt{2m_x m_y m_z\varepsilon}}{\pi^2\hbar^3}
\end{aligned} \tag{8.14}$$

Transformation from ellipsoidal coordinates to spherical coordinates, accompanied with the definition of band velocity and effective mass, analogous to Eq. 8.3, lead to the transport distribution functions similar to the calculations in the main manuscript. The isothermal

Nernst coefficient is obtained as follows:

$$\alpha_{ij}(H)=\left[\sigma_{ij}(H)\right]^{-1}\left[B_{ij}(H)\right]$$

$$\alpha_{ij}(H)=\left(\begin{bmatrix}\sigma_{xx}&0&0\\0&\sigma_{yy}&0\\0&0&\sigma_{zz}\end{bmatrix}+\begin{bmatrix}0&\sigma_{xyz}&0\\\sigma_{yxz}&0&0\\0&0&0\end{bmatrix}\right)^{-1}\left(\begin{bmatrix}B_{xx}&0&0\\0&B_{yy}&0\\0&0&B_{zz}\end{bmatrix}+\begin{bmatrix}0&B_{xyz}&0\\B_{yxz}&0&0\\0&0&0\end{bmatrix}\right)$$

$$\alpha_{ij}(H)=\begin{bmatrix}\sigma_{xx}&\sigma_{xyz}&0\\\sigma_{yxz}&\sigma_{yy}&0\\0&0&\sigma_{zz}\end{bmatrix}^{-1}\begin{bmatrix}B_{xx}&B_{xyz}&0\\B_{yxz}&B_{yy}&0\\0&0&B_{zz}\end{bmatrix}$$

$$\alpha_{ij}(H)=\frac{1}{\sigma_{zz}(\sigma_{xx}\sigma_{yy}-\sigma_{xyz}\sigma_{yxz})}\begin{bmatrix}\sigma_{yy}\sigma_{zz}&-\sigma_{zz}\sigma_{xyz}&0\\-\sigma_{zz}\sigma_{yxz}&\sigma_{xx}\sigma_{zz}&0\\0&0&\sigma_{xx}\sigma_{yy}-\sigma_{xyz}\sigma_{yxz}\end{bmatrix}\begin{bmatrix}B_{xx}&B_{xyz}&0\\B_{yxz}&B_{yy}&0\\0&0&B_{zz}\end{bmatrix}$$

$$N_T(H)=-\alpha_{yx}(H)=-\frac{-\sigma_{zz}\sigma_{yxz}B_{xx}+\sigma_{xx}\sigma_{zz}B_{yxz}}{\sigma_{zz}(\sigma_{xx}\sigma_{yy}-\sigma_{xyz}\sigma_{yxz})}=-\frac{\sigma_{xx}B_{yxz}-\sigma_{yxz}B_{xx}}{\sigma_{xx}\sigma_{yy}-\sigma_{xyz}\sigma_{yxz}} \tag{8.15}$$

8.1.3 Non-parabolic bands

The dispersion of non-parabolic bands can be approximated as $\varepsilon(1+\lambda\varepsilon)=\frac{\hbar^2k^2}{2m}$. Similar to Eq. 8.14, the density of states is obtained as $g(\varepsilon)=\frac{\sqrt{m_xm_ym_z\varepsilon(1+\lambda\varepsilon)}}{\pi^2\hbar^3\sqrt{2}}(1+2E\lambda)$. Eq. 8.2 is used for group velocity.

$$\nu_i=\frac{1}{\hbar}\frac{\partial\varepsilon}{\partial k_i}=\frac{\hbar^2k_i}{(2\lambda\varepsilon+1)m_i}=\frac{\hbar^2}{(2\lambda\varepsilon+1)m_i}\frac{\sqrt{2m_i\varepsilon(1+\lambda\varepsilon)}}{\hbar}=\frac{\sqrt{2m_i\varepsilon(1+\lambda\varepsilon)}}{(2\lambda\varepsilon+1)m_i} \tag{8.16}$$

I continue to compute transport distribution function for such dispersion.

$$\begin{aligned}\Xi_{ii}(\varepsilon)&=\frac{\tau q^2}{3}\nu_{ii}^2g(\varepsilon)=\frac{\tau q^2}{3}\frac{2E(1+\lambda\varepsilon)}{m_i(1+2\lambda\varepsilon)^2}g(\varepsilon)\\&=\frac{\tau q^2}{3}\frac{\varepsilon(1+\lambda\varepsilon)}{m_i(1+2\lambda\varepsilon)}\frac{\sqrt{2m_xm_ym_z\varepsilon(1+\lambda\varepsilon)}}{\pi^2\hbar^3}\end{aligned} \tag{8.17}$$

For the 2nd Order transport distribution function Ξ_{ijk} I need to compute $\nu_i\tau^2(\frac{q\tau}{\hbar}\nu\times H)\cdot\nabla_k\nu_j$. Assume H is along z-axis. Similar to spherical dispersion, integration of $\nu_i\nu_j$ over the whole

Brillouin zone yields zero.

$$[\Xi]_{ijk}= \begin{bmatrix} 0 & -\frac{\tau^2 q^3 H_z}{3V}\frac{\varepsilon(1+\lambda\varepsilon)}{m_x m_y(1+2\lambda\varepsilon)^2}\frac{\sqrt{2m_x m_y m_z\varepsilon(1+\lambda\varepsilon)}}{\pi^2\hbar^3} & 0 \\ \frac{\tau^2 q^3 H_z}{3V}\frac{\varepsilon(1+\lambda\varepsilon)}{m_x m_y(1+2\lambda\varepsilon)^2}\frac{\sqrt{2m_x m_y m_z\varepsilon(1+\lambda\varepsilon)}}{\pi^2\hbar^3} & 0 & 0 \\ 0 & 0 & 0 \end{bmatrix} \tag{8.18}$$

8.2 Spherical bands

I imagine a two parabolic band model with a non-zero band gap. The two parts of the transport distribution function were derived in our previous work [130]:

$$\begin{aligned} \Xi_{xx} &= \frac{2\tau(\varepsilon)q^2\varepsilon\sqrt{2m\varepsilon}}{3\hbar^3\pi^2} \\ \Xi_{xyz} &= \frac{2q^3 H_z\tau(\varepsilon)^2\varepsilon\sqrt{2\varepsilon}}{3\hbar^3\pi^2\sqrt{m}} \end{aligned} \tag{8.19}$$

The response functions required for the Nernst coefficient are σ and B.

$$\begin{aligned} \sigma_{xx} &= \int \Xi_{xx}(\varepsilon)\left(-\frac{\partial f(\varepsilon,\mu,T)}{\partial\varepsilon}\right)d\varepsilon \\ B_{xx} &= \frac{1}{qT}\int \Xi_{xx}(\varepsilon)\left(-\frac{\partial f(\varepsilon,\mu,T)}{\partial\varepsilon}\right)(\varepsilon-\mu)d\varepsilon \\ \sigma_{xyz} &= \int \Xi_{xyz}(\varepsilon)\left(-\frac{\partial f(\varepsilon,\mu,T)}{\partial\varepsilon}\right)d\varepsilon \\ B_{xyz} &= \frac{1}{qT}\int \Xi_{xyz}(\varepsilon)\left(-\frac{\partial f(\varepsilon,\mu,T)}{\partial\varepsilon}\right)(\varepsilon-\mu)d\varepsilon \end{aligned} \tag{8.20}$$

For a non-degenerate semiconductor the relaxation time (τ) is stated as a power function of energy $\tau(\varepsilon) = \tau_0\varepsilon^r$, which is a reasonable estimation [114]. Besides, Fermi-Dirac ($\mathcal{F}$) and Γ integrals can simplify the integrals in Eq. 8.20.

$$\begin{aligned} \mathcal{F}_n(z) &= \int_0^\infty z^n f^0(z)dz \\ \Gamma(z) &= \int_0^\infty t^{z-1}\exp -t dt \end{aligned} \tag{8.21}$$

It can be proved that $\Gamma(z+1) = z\Gamma(z)$ and $\Gamma(1/2) = \sqrt{\pi}$. For a non-degenerate semiconductor the Fermi-Dirac distribution function is estimated as $\exp\left(\frac{\mu-\varepsilon}{k_B T}\right)$ and thus the Fermi-Dirac integral turns into $\mathcal{F}_n(z) = \exp(z)\Gamma(n+1)$. With the help of the above equations,

integrals in the form of Eq. 8.20 can be replaced by:

$$\int_0^\infty \varepsilon^u \left(-\frac{\partial f(\varepsilon,\mu,T)}{\partial \varepsilon}\right) d\varepsilon = u\int_0^\infty \varepsilon^{u-1} f(\varepsilon,\mu,T)d\varepsilon = u(k_BT)^u \exp(\frac{\mu}{k_BT})\Gamma(u) \quad (8.22)$$

Mind that the Eq. 8.22 has to be assessed for the valence band and conduction band, separately, and then summed. So that the integrals in Eq. 8.20 are unraveled.

$$\begin{aligned}
\sigma_{xx} &= \mathcal{A}\Big[\lambda_c exp\big(\frac{\mu-\varepsilon_c}{k_BT}\big) + \lambda_v exp\big(\frac{\varepsilon_v-\mu}{k_BT}\big)\Big] \\
B_{xx} &= \frac{\mathcal{A}}{qT}\Big[\big[(r+5/2)k_BT+\varepsilon_c-\mu\big]\lambda_c exp\big(\frac{\mu-\varepsilon_c}{k_BT}\big) + \big[(r+5/2)k_BT-\varepsilon_v+\mu\big]\lambda_v exp\big(\frac{\varepsilon_v-\mu}{k_BT}\big)\Big] \\
\sigma_{xyz} &= \mathcal{Q}\Big[\frac{\lambda_c}{m_c} exp\big(\frac{\mu-\varepsilon_c}{k_BT}\big) + \frac{\lambda_v}{m_v} exp\big(\frac{\varepsilon_v-\mu}{k_BT}\big)\Big] \\
B_{xyz} &= \frac{\mathcal{Q}}{qT}\Big[\big[(2r+5/2)k_BT+\varepsilon_c-\mu\big]\frac{\lambda_c}{m_c} exp\big(\frac{\mu-\varepsilon_c}{k_BT}\big) + \big[(2r+5/2)k_BT-\varepsilon_v+\mu\big]\frac{\lambda_v}{m_v} exp\big(\frac{\varepsilon_v-\mu}{k_BT}\big)\Big]
\end{aligned} \quad (8.23)$$

Where $\lambda_i = \frac{2q^2\sqrt{2m_i}}{3\hbar^3\pi^2}$, $\mathcal{A} = (r+3/2)(k_BT)^{r+3/2}\Gamma(r+3/2)$, and $\mathcal{Q} = qH(2r+3/2)(k_BT)^{2r+3/2}\Gamma(2r+3/2)$. On the other hand, electron (n) and hole (p) concentrations for a non-degenerate semiconductor are estimated as $n = \frac{m_c k_BT\sqrt{2m_c k_BT}}{\pi^2\hbar^3} exp(\frac{\mu-\varepsilon_c}{k_BT})\frac{\sqrt{\pi}}{2} = N_c exp(\frac{\mu-\varepsilon_c}{k_BT})$ and $p = \frac{m_v k_BT\sqrt{2m_v k_BT}}{\pi^2\hbar^3} exp(\frac{\varepsilon_v-\mu}{k_BT})\frac{\sqrt{\pi}}{2} = N_v exp(\frac{\varepsilon_v-\mu}{k_BT})$. So that the equations in 8.23 can be summarized in terms of carrier concentrations.

$$\begin{aligned}
\sigma_{xx} &= \mathcal{A}\Big[M_c n + M_v p\Big] \\
B_{xx} &= \frac{\mathcal{A}}{qT}\Big[[(r+5/2)k_BT+\varepsilon_c-\mu]M_c n + [(r+5/2)k_BT+\mu-\varepsilon_v]M_v p\Big] \\
\sigma_{xyz} &= \mathcal{Q}\Big[\frac{M_c}{m_c} n + \frac{M_v}{m_v} p\Big] \\
B_{xyz} &= \frac{\mathcal{Q}}{qT}\Big[[(2r+5/2)k_BT+\varepsilon_c-\mu]\frac{M_c n}{m_c} + [(2r+5/2)k_BT+\mu-\varepsilon_v]\frac{M_v p}{m_v}\Big]
\end{aligned} \quad (8.24)$$

Where $M_i = \frac{4q^2}{3m_i k_BT\sqrt{k_BT\pi}}$. For the sake of the simplicity, I assume acoustic phonon deformation is the dominant scattering mechanism, which was reported for Ge, and r=-1/2. The above response functions are inserted in the definition of the Nernst coefficient (Eq. 8.13)

and the Nernst coefficient for a two spherical band system is accomplished.

$$\frac{k_B\sqrt{k_BT\pi}}{2}\Big[\frac{nM_c(2M_vpk_BT-4pM_v\mu-k_BTnM_c)}{2m_c}-\frac{pM_v(nM_ck_bT-pM_vk_BT-4pM_v\mu)}{2m_v}$$
$$+nM_cpM_v(\frac{\varepsilon_v+\varepsilon_c}{m_c}-\frac{\varepsilon_c+\varepsilon_v}{m_v})\Big]\Big/\Big[(k_BT[nM_c+pM_v])^2+(\frac{q\sqrt{k_BT\pi}}{2}[\frac{nM_c}{m_c}]+\frac{pM_v}{m_v})^2\Big] \tag{8.25}$$

8.3 Code's flags

8.3.1 The Nernst calculation within CRTA

In this section I introduce the flags used for the calculation of the Nernst coefficient within CRTA. The code is written in fortran language

`logical :: nerwann`

Determines whether to compute the isothermal Hall conductivity, isothermal Nernst coefficient , and Ettingshausen coefficient.

The default value is `false`.

`integer :: ner_kmesh(:)`

It specifies the interpolation k mesh used to calculate the total transport distribution function.

`real(kind=dp) :: ner_kmesh_spacing`

Overrides the `kmesh_spacing` global variable (see the Wannier90 documentation).

`character(len=4) :: ner_2d_dir`

It is the direction along which the system is non-periodic in 2D systems.

The default value is `no`.

`real(kind=dp) :: ner_relax_time`

The value of the constant relaxation time in fs to be used in the total transport distribution function.

The default value is 10 fs.

`real(kind=dp) :: ner_mu_min`

Minimum value of the chemical potential μ for which thermomagnetic properties are calculated.

The units are eV. No default value.

`real(kind=dp) :: ner_mu_max`

Maximum value of the chemical potential μ for which thermomagnetic properties are calculated.

The units are eV. No default value.

`real(kind=dp) :: ner_mu_step`

Energy step for the grid of chemical potentials from ner_mu_min to ner_mu_max in eV.

No default value.

`real(kind=dp) :: ner_temp_min`

Minimum value of temperature for which thermomagnetic properties are calculated.

The units are K and there is no default value.

`real(kind=dp) :: ner_temp_max`

Maximum value of temperature for which thermomagnetic properties are calculated.

The units are K and there is no default value.

`real(kind=dp) :: ner_temp_step`

Energy step for the grid of temperatures from ner_temp_min to ner_temp_max.

The units are K and there is no default value.

`real(kind=dp) :: ner_tdf_energy_step`

Energy step for the grid of energies in the total transport distribution function.

The units are eV and the default value is 0.001 eV.

`character(len=120) :: ner_tdf_smr_type`

The type of smearing function to be used for the total transport distribution function. The

default value is the one given via the smr_type input flag (if defined).

real(kind=dp) :: ner_tdf_smr_fixed_en_width

Energy width for the smearing function in eV unit. For the total transport distribution function, a standard (non-adaptive) smearing scheme is used.

The default value is 0 eV. Note that if the width is smaller than twice the energy step ner_tdf_energy_step, the total transport distribution function will be unsmeared.

logical :: ner_bandshift

Shift all conduction bands by the value of ner_bandshift_energyshift. Such a shift is applied after interpolation and the index of the first band to shift is required.

The default value is false.

integer :: ner_bandshift_firstband

Index of the first conduction band to shift.

It means that this band and all the above bands all bands will be shifted by

ner_bandshift_energyshift.

The units are eV and it has to be specified if ner_bandshift is true.

real(kind=dp) :: ner_bandshift_energyshift

Energy shift of the conduction bands in the unit of eV. It has to be provided if ner_bandshift is true.

real(kind=dp) :: bext(3)

The external magnetic field vector in units of Tesla for the calculation of thermomagnetic properties. The default value is (0.0,0.0,0.0)

8.3.2 The Nernst calculation within RTA

In this section I introduce the input parameters in our code to compute the Nernst coefficient within RTA. The code is written in python language and mind that there are no default values

for the input parameters and all the flags have to be specified.

`real :: smrT`

The smearing temperature in the units of K.

`real :: Evwan`

The top of the valence band of the wannierized band structure in the units of eV.

`character :: prefix`

prefix of the DFT calculation. It has to be consistent in all steps: DFT, wannierization, and scattering rates.

`real :: Eg`

The experimental band gap in the units of eV.

`real :: Ev`

The top of the valence band from the nscf calculation for the scattering rate calculation in the units of eV.

`real :: muban`

The chemical potential span in both bands in the units of eV.

`real :: mustep`

The chemical potential step size in the units of eV.

`real :: Bext`

The external magnetic field along z-axis in the units of T.

`integer :: amesh`

The mesh grid printed in the output of scattering rate calculation.

`real :: eps0`

The tolerance value for the derivative of the Fermi–Dirac distribution function.

Bibliography

[1]A. Ettingshausen **and** W. W. Nernst, Ann **29**, 343 (1886).

[2]P. Fernández-Yáñez, V. Romero, O. Armas **and** G. Cerretti, 'Thermal management of thermoelectric generators for waste energy recovery', Applied Thermal Engineering **196**, 117291 (2021).

[3]T. Starner, 'Human-powered wearable computing', IBM systems Journal **35**, 618–629 (1996).

[4]T. Sugahara, Y. Ekubaru, N. V. Nong, N. Kagami, K. Ohata, L. T. Hung, M. Okajima, S. Nambu **and** K. Suganuma, 'Fabrication with semiconductor packaging technologies and characterization of a large-scale flexible thermoelectric module', Advanced Materials Technologies **4**, 1800556 (2019).

[5]K. Nan, S. D. Kang, K. Li, K. J. Yu, F. Zhu, J. Wang, A. C. Dunn, C. Zhou, Z. Xie **and** M. T. s. Agne, 'Compliant and stretchable thermoelectric coils for energy harvesting in miniature flexible devices', Science Advances **4**, eaau5849 (2018).

[6]T. Sun, B. Zhou, Q. Zheng, L. Wang, W. Jiang **and** G. J. Snyder, 'Stretchable fabric generates electric power from woven thermoelectric fibers', Nature communications **11**, 1–10 (2020).

[7]C. Zheng, L. Xiang, W. Jin, H. Shen, W. Zhao, F. Zhang, C.-a. Di **and** D. Zhu, 'A flexible self-powered sensing element with integrated organic thermoelectric generator', Advanced Materials Technologies **4**, 1900247 (2019).

[8]S. Jo, M. Kim, M. Kim **and** Y. Kim, 'Flexible thermoelectric generator for human body heat energy harvesting', Electronics letters **48**, 1015–1017 (2012).

[9]W. Ren, Y. Sun, D. Zhao, A. Aili, S. Zhang, C. Shi, J. Zhang, H. Geng, J. Zhang **and** L. s. Zhang, 'High-performance wearable thermoelectric generator with self-healing, recycling, and lego-like reconfiguring capabilities', Science advances **7**, eabe0586 (2021).

[10]A. W. Smith, 'The transverse thermomagnetic effect in nickel and cobalt', Physical Review (Series I) **33**, 295 (1911).

[11]A. W. Smith, 'The hall effect and allied phenomena in rare metals and alloys', Physical Review **8**, 79 (1916).

[12]A. W. Smith, 'The hall effect and the nernst effect in magnetic alloys', Physical Review **17**, 23 (1921).

[13]K. Ikeda, H. Nakamura, I. Yanenaga **and** S. Yamaguchi, 'Transport coefficients of ge in magnetic fields', **in**Seventeenth international conference on thermoelectrics. proceedings ict98 (cat. no. 98th8365) (IEEE, 1998), **pages** 277–279.

[14]H. Nakamura, K. Ikeda **and** S. Yamaguchi, 'Transport coefficients of insb in a strong magnetic field', **in**Xvi ict'97. proceedings ict'97. 16th international conference on thermoelectrics (cat. no. 97th8291) (IEEE, 1997), **pages** 142–146.

[15]M. El-Saden **and** F. Thomas, 'Nernst effect in indium antimonide', Journal of Applied Physics **36**, 181–183 (1965).

[16]G. Moreau, 'Sur les phénomènes thermomagnétiques', J. Phys. Theor. Appl. **9**, 497–506 (1900).

[17]M. S. Akhanda, S. E. Rezaei, K. Esfarjani, S. Krylyuk, A. V. Davydov **and** M. Zebarjadi, 'Thermomagnetic properties of bi 2 te 3 single crystal in the temperature range from 55 k to 380 k', Physical Review Materials **5**, 015403 (2021).

[18]R. Mansfield **and** W. Williams, 'The electrical properties of bismuth telluride', Proceedings of the Physical Society (1958-1967) **72**, 733 (1958).

[19]I. Heft, 'Beziehungen zwischen den koeffizienten der galvano-und thermomagnetischen transversaleffekte in ferromagneten',

[20]A. Sommerfeld **and** N. H. Frank, 'The statistical theory of thermoelectric, galvano-and thermomagnetic phenomena in metals', Reviews of Modern Physics **3**, 1 (1931).

[21]E. Sondheimer, 'The theory of the galvanomagnetic and thermomagnetic effects in metals', Proceedings of the Royal Society of London. Series A. Mathematical and Physical Sciences **193**, 484–512 (1948).

[22]H. B. Callen, 'The application of onsager's reciprocal relations to thermoelectric, thermomagnetic, and galvanomagnetic effects', Physical Review **73**, 1349 (1948).

[23]E. Putley, 'Thermoelectric and galvanomagnetic effects in lead selenide and telluride', Proceedings of the Physical Society. Section B **68**, 35 (1955).

[24]F. Seitz **and** R. Johnson, 'Modern theory of solids. i', Journal of Applied Physics **8**, 84–97 (1937).

[25]A. Sommerfeld, 'Zur elektronentheorie der metalle auf grund der fermischen statistik', Zeitschrift für Physik **47**, 1–32 (1928).

[26]H. A. Lorentz, *The theory of electrons and its applications to the phenomena of light and radiant heat*, **volume** 29 (GE Stechert & Company, 1916).

[27]P. Price, 'Theory of transport effects in semiconductors: the nernst coefficient, and its relation to thermoelectric power', Physical Review **102**, 1245 (1956).

[28]R. Delves, 'Thermomagnetic effects in semiconductors and semimetals', Reports on Progress in Physics **28**, 249 (1965).

[29]H. Nakamura, K. Ikeda **and** S. Yamaguchi, 'Physical model of nernst element', **in**Seventeenth international conference on thermoelectrics. proceedings ict98 (cat. no. 98th8365) (IEEE, 1998), **pages** 97–100.

[30]H. Okumura, Y. Hasegawa, H. Nakamura **and** S. Yamaguchi, 'A computational model of thermoelectric and thermomagnetic semiconductors', **in**Eighteenth international conference on thermoelectrics. proceedings, ict'99 (cat. no. 99th8407) (IEEE, 1999), **pages** 209–212.

[31]Y. Liu, H.-J. Zhang **and** Y. Yao, 'Ab initio investigation of magnetic transport properties by wannier interpolation', Physical Review B **79**, 245123 (2009).

[32]K. Ohno, K. Esfarjani **and** Y. Kawazoe, *Computational materials science: from ab initio to monte carlo methods* (Springer, 2018).

[33]G. K. Madsen **and** D. J. Singh, 'Boltztrap. a code for calculating band-structure dependent quantities', Computer Physics Communications **175**, 67–71 (2006).

[34]G. K. Madsen, J. Carrete **and** M. J. Verstraete, 'Boltztrap2, a program for interpolating band structures and calculating semi-classical transport coefficients', Computer Physics Communications **231**, 140–145 (2018).

[35]G. Pizzi, D. Volja, B. Kozinsky, M. Fornari **and** N. Marzari, 'Boltzwann: a code for the evaluation of thermoelectric and electronic transport properties with a maximally-localized wannier functions basis', Computer Physics Communications **185**, 422–429 (2014).

[36]F. Macheda **and** N. Bonini, 'Magnetotransport phenomena in p-doped diamond from first principles', Physical Review B **98**, 201201 (2018).

[37]S. Zhang, Q. Wu, Y. Liu **and** O. V. Yazyev, 'Magnetoresistance from fermi surface topology', Physical Review B **99**, 035142 (2019).

[38]D. C. Desai, B. Zviazhynski, J.-J. Zhou **and** M. Bernardi, 'Magnetotransport in semiconductors and two-dimensional materials from first principles', Physical Review B **103**, L161103 (2021).

[39]J.-J. Zhou, J. Park, I.-T. Lu, I. Maliyov, X. Tong **and** M. Bernardi, 'Perturbo: a software package for ab initio electron–phonon interactions, charge transport and ultrafast dynamics', Computer Physics Communications **264**, 107970 (2021).

[40]A. A. Mostofi, J. R. Yates, Y.-S. Lee, I. Souza, D. Vanderbilt **and** N. Marzari, 'Wannier90: a tool for obtaining maximally-localised wannier functions', Computer physics communications **178**, 685–699 (2008).

[41]H. Jones **and** C. Zener, 'The theory of the change in resistance in a magnetic field', Proceedings of the Royal Society of London. Series A, Containing Papers of a Mathematical and Physical Character **145**, 268–277 (1934).

[42]L. Bell, 'Cooling, heating, generating power, and recovering waste heat with thermoelectric systems', Science **321**, 1457–1461 (2008).

[43]H. Goldsmid, *Thermoelectric refrigeration* (Springer, 2013).

[44]A. F. Ioffe, L. Stil'bans, E. Iordanishvili, T. Stavitskaya, A. Gelbtuch **and** G. Vineyard, 'Semiconductor thermoelements and thermoelectric cooling', Physics Today **12**, 42–42 (1959).

[45]M. Zebarjadi, K. Esfarjani, M. S. Dresselhaus, Z. F. Ren **and** G. Chen, 'Perspectives on thermoelectrics: from fundamentals to device applications', Energy Environ. Sci. **5**, 5147–5162 (2012).

[46]G. Mahan, 'Good thermoelectrics', Solid state physics (New York. 1955) **51**, 81–157 (1997).

[47]M. Zebarjadi, 'Electronic cooling using thermoelectric devices', Applied Physics Letters **106**, 203506 (2015).

[48]M. Adams, M. Verosky, M. Zebarjadi **and** J. Heremans, 'Active peltier coolers based on correlated and magnon-drag metals', Physical Review Applied **11**, 054008 (2019).

[49]M. Zebarjadi, 'Solid-state thermionic power generators: an analytical analysis in the non-linear regime', Phys. Rev. Applied **8**, 014008 (2017).

[50]M. G. Rosul, D. Lee, D. H. Olson, N. Liu, X. Wang, P. E. Hopkins, K. Lee **and** M. Zebarjadi, 'Thermionic transport across gold-graphene-$W\mathrm{i}Se_2$ van der waals heterostructures', Science advances **5**, eaax7827 (2019).

[51]G. Mahan **and** J. O. Sofo, 'The best thermoelectric', Proceedings of the National Academy of Sciences **93**, 7436–7439 (1996).

[52]D. Rowe, 'Applications of nuclear-powered thermoelectric generators in space', Applied Energy **40**, 241–271 (1991).

[53]Z. Yuan, X. Tang, Z. Xu, J. Li, W. Chen, K. Liu, Y. Liu **and** Z. Zhang, 'Screen-printed radial structure micro radioisotope thermoelectric generator', Applied Energy **225**, 746–754 (2018).

[54]M. Thielen, L. Sigrist, M. Magno, C. Hierold **and** L. Benini, 'Human body heat for powering wearable devices: from thermal energy to application', Energy conversion and management **131**, 44–54 (2017).

[55]M. Guan, K. Wang, D. Xu **and** W.-H. Liao, 'Design and experimental investigation of a low-voltage thermoelectric energy harvesting system for wireless sensor nodes', Energy Conversion and Management **138**, 30–37 (2017).

[56]T. Torfs, V. Leonov, C. Van Hoof **and** B. Gyselinckx, 'Body-heat powered autonomous pulse oximeter', **in**Sensors, 2006 ieee (IEEE, 2006), **pages** 427–430.

[57]G. Pistoia, 'Chapter 6-batteries for medical and special applications', Batteries for Portable Devices. Elsevier Science BV, 147–162 (2005).

[58]N. Jaziri, A. Boughamoura, J. Müller, B. Mezghani, F. Tounsi **and** M. Ismail, 'A comprehensive review of thermoelectric generators: technologies and common applications', Energy Reports **6**, 264–287 (2020).

[59]B. Iezzi, K. Ankireddy, J. Twiddy, M. D. Losego **and** J. S. Jur, 'Printed, metallic thermoelectric generators integrated with pipe insulation for powering wireless sensors', Applied energy **208**, 758–765 (2017).

[60]W. Wang, V. Cionca, N. Wang, M. Hayes, B. O'Flynn **and** C. O'Mathuna, 'Thermoelectric energy harvesting for building energy management wireless sensor networks', International journal of distributed sensor networks **9**, 232438 (2013).

[61]M. Al Musleh, E. Topriska, L. Jack **and** D. Jenkins, 'Thermoelectric generator experimental performance testing for wireless sensor network application in smart buildings', **in**Matec web of conferences **volume** 120 (EDP Sciences, 2017), **page** 08003.

[62]J.-M. Dilhac, R. Monthéard, M. Bafleur, V. Boitier, P. Durand-Estèbe **and** P. Tounsi, 'Implementation of thermoelectric generators in airliners for powering battery-free wireless sensor networks', Journal of electronic materials **43**, 2444–2451 (2014).

[63]A. J. Streb, 'Radioisotope power systems for manned space stations', **in***Progress in astronautics and rocketry* **volume** 16 (Elsevier, 1966), **pages** 3–29.

[64]G. L. Bennett, C. Whitmore **and** W. Amos, 'On the development of the power sources for the ulysses and galileo missions', **in**Proceedings of the european space power conference (1989), **pages** 117–121.

[65]R. D. Lorenz **and** E. S. Clarke, 'Influence of the multi-mission radioisotope thermoelectric generator (mmrtg) on the local atmospheric environment', Planetary and Space Science **193**, 105075 (2020).

[66]J. O. Sofo **and** G. Mahan, 'Thermoelectric figure of merit of superlattices', Applied Physics Letters **65**, 2690–2692 (1994).

[67]Y. Guldner, C. Rigaux, M. Grynberg **and** A. Mycielski, 'Interband $\Gamma_6 \rightarrow \Gamma_8$ magnetoabsorption in HgTe', Phys. Rev. B **8**, 3875 (1973).

[68]S. L. Lehoczky, J. G. Broerman, D. A. Nelson **and** C. R. Whitsett, 'Temperature-dependent electrical properties of HgSe', Physical Review B **9**, 1598 (1974).

[69]J. P. Issi, 'Temperature transport properties of the group v semimetals', Aust. J. Phys. **32**, 585 (1979).

[70]L. Berger, *Semiconductor materials* (CRC Press, Boca Raton, Florida, 1997).

[71]E. Nikolskaya **and** A. R. Regel, Zhur. Tekh. Fiz **25**, 1352 (1955).

[72]T. C. Harman, *Physics and chemistry of ii-vi compounds* (North-Holland Publishing Company, Amsterdam, 1967).

[73]T. Dietl **and** W. Szymanska, 'Electron scattering in HgSe', J. Phys. Chem. Solids **39**, 1041 (1978).

[74]M. Baj **and** S. Porowski, High Temperatures-High Pressures **6**, 95 (1974).

[75]R. J. Dinger **and** A. W. Lawson, 'Cyclotron resonance and the cohen nonellipsoidal nonparabolic model for bismuth.III. experimental results', Phys. Rev. B **7**, 5215 (1973).

[76]G. A. Slack, 'Thermal conductivity of II-VI compounds and phonon scattering by $Fe2^{+}$ impurities', Phys. Rev. B **6**, 3791 (1972).

[77]M. Markov, X. Hu, H.-C. Liu, N. Liu, J. Poon, K. Esfarjani **and** M. Zebarjadi, 'Semimetals as potential thermoelectric materials: case of HgTe', Scientific Reports **8**, 9876 (2018).

[78]C. F. Gallo, B. S. Chandrasekhar **and** P. H. Sutter, 'Transport properties of bismuth single crystals', J. Appl. Phys. **34**, 144 (1963).

[79]S. Lee, K. Esfarjani, J. Mendoza, M. S. Dresselhaus **and** G. Chen, 'Lattice thermal conductivity of bi, sb, and bi-sb alloy from first principles', Phys. Rev. B **89**, 085206 (2014).

[80]M. Markov, J. Sjakste, G. Fugallo, L. Paulatto, M. Lazzeri, F. Mauri **and** N. Vast, 'Nanoscale mechanisms for the reduction of heat transport in bismuth', Phys. Rev. B **93**, 064301 (2016).

[81]V. D. Kagan **and** N. A. Red'ko, 'Phonon thermal conductivity of bismuth alloys', Sov. Phys. JETP **73(4)** (1991).

[82]. S. Singh, Q. S. Wu, C. Yue, A. H. Romero **and** A. A. Soluyanov, 'Topological phonons and thermoelectricity in triple-point metals', Phys. Rev. Mat. **2**, 114204 (2018).

[83]M. Z. Hasan **and** C. L. Kane, 'Colloquium: topological insulators', Rev. Mod. Phys. **82**, 3045 (2010).

[84]J. W. Nicklas **and**. J. W. Wilkins, 'Accurate electronic properties for (hg,cd)te systems using hybrid density functional theory', Phys. Rev. B **84**, 121308(R) (2011).

[85]M. Zebarjadi, G. Chen, Z. Ren, R. Shin S. Chen, J. P. Heremans, B. Wiendlocha, H. Jin, B. Wang **and** Q. Zhang, *Advanced thermoelectrics: matrials, contacts, devices and systems, edited by Z. Ren, Y. Lan, Q. Zhang* (CRC Press, 2018).

[86]Z. Ren, Y. Lan **and** Q. Zhang, *Advanced thermoelectrics: materials, contacts, devices, and systems* (CRC Press, 2017).

[87]G. Samsonidze **and** B. Kozinsky, 'Accelerated screening of thermoelectric materials by first-principles computations of electron–phonon scattering', Adv. Energy Mater. **8**, 1800246 (2018).

[88]S. Ahmad **and** S. D. Mahanti, 'Energy and temperature dependence of relaxation time and wiedemann-franz law on pbte', Phys. Rev. B **81**, 165203 (2010).

[89]D. A. Pshenay-Severin, Y. Ivanov **and** A. T. Burkov, 'The effect of energy-dependent electron scattering on thermoelectric transport in novel topological semimetal CoSi', J. Phys.: Condens. Matter **30**, 475501 (2018).

[90]H. Lin, T. Das, Y.-J. Wang, L. Wray, S.-Y. Xu, M. Hasan **and** A. Bansil, 'Adiabatic transformation as a search tool for new topological insulators: distorted ternary Li_2AgSb-class semiconductors and related compounds', Physical Review B **87**, 121202(R) (2013).

[91]N. Li, K. L. Yao **and** X.-J. Zhao, 'Ab initio of structural and electronic properties of ternary alkali-metal-based semimetal compounds', Comp. Mat. Sci, **91**, 231 (2014).

[92]Y.-S. Kim, K. Hummer **and** G. Kresse, 'Accurate band structures and effective masses for inp, inas, and insb using hybrid functionals', Phys. Rev. B **80**, 035203 (2009).

[93]Y. Saeed, N. Singh, D. Parker **and** U. Schwingenschlogl, 'Thermoelectric performance of electron and hole doped $PtSb_2$', J. Appl. Phys. **113**, 163706 (2013).

[94]W. Gao, N. Hao, F.-W. Zheng, W. Ning, M. Wu, X. Zhu, G. Zheng, J. Zhang, J. Lu, H. Zhang, C. Xi, J. Yang, H. Du, P. Zhang, Y. Zhang **and** M. Tian, 'Extremely large magnetoresistance in a topological semimetal candidate pyrite $PtBi_2$', Phys. Rev. Let. **118**, 256601 (2017).

[95]M. Sondergaard, M. Christensen, L. Bjerg, K. A. Borup, P. Sun, F. Steglich **and** B. B. Iversen, 'Investigation of the correlation between stoichiometry and thermoelectric properties in a $PtSb_2$ single crystals', Dalton Trans. **41**, 1278 (2012).

[96]C.-W. T. Lo, B. R. Ortiz, E. S. Toberer, A. He, V. Svitlyk, D. Chernyshov, T. Kolodiazhnyi, S. Lidin **and** Y. Mozharivskyj, 'Synthesis, structure and thermoelectric properties of α-Zn_3Sb_2 and comparison to β-$Zn_{13}Sb_{10}$', Chem Mater. **29**, 5249 (2017).

[97]S. Nayeb Sadeghi, M. Zebarjadi **and** K. Esfarjani, 'Biaxial tensile strain-induced enhancement of thermoelectric performance of tise2 monolayer based on first-principles calculation', J. Mater. Chem. C, DOI:10.1039/C9TC00183B (2019) DOI:10.1039/C9TC00183B.

[98]G. Kresse **and** J. Furthmüller, 'Efficiency of ab-initio total energy calculations for metals and semiconductors using a plane-wave basis set', Computational materials science **6**, 15–50 (1996).

[99]G. Kresse **and** J. Furthmüller, 'Efficient iterative schemes for ab initio total-energy calculations using a plane-wave basis set', Physical review B **54**, 11169 (1996).

[100]P. E. Blöchl, 'Projector augmented-wave method', Physical review B **50**, 17953 (1994).

[101]J. Heyd, G. E. Scuseria **and** M. Ernzerhof, 'Hybrid functionals based on a screened coulomb potential', The Journal of chemical physics **118**, 8207–8215 (2003).

[102]G. D. Mahan, 'Good thermoelectrics', Solid State Physics **51**, 81–157 (1998).

[103]D. M. Rowe, *Thermoelectrics handbook: macro to nano, edited by d. m.rowe* (CRC Press, 2006).

[104]G. A. Saunders, C. Miziimski, G. S. Cooper **and** A. W. Lawson, 'The seebeck coefficients of antimony and arsenic single crystals', J. Hys. Chetn. Solids **26**, 1299 (1965).

[105]A. N. Goland **and** A. W. Ewald, 'Thermoelectric power of gray tin', Phys. Rev. **104**, 948 (1956).

[106]C. R. Whitsett **and** D. A. Nelson, 'Lattice thermal conductivity of p-type mercury telluride', Phys. Rev. B **5**, 3125 (1972).

[107]S. Waldrop **and** D. Morelli, 'Low-temperature thermoelectric properties of $ptsb_2 - xte_x$ for cryogenic peltier cooling applications', J. Electron. Mater. **44**, 1562 (2015).

[108]Y. Wang, C. Pan L.and Li, R. Tian, R. Huang, X. Hu, C. Chen, N. Bao, K. Koumoto **and** C. Lu, 'Doubling the zt record of tis_2-based thermoelectrics by incorporation of ionized impurity scattering', J. Mater. Chem. C **6**, 9345 (2018).

[109]B. Saparov, J. E. Mitchell **and** A. S. Sefat, 'Properties of binary transition-metal arsenides (tas)', Supercond. Sci. Technol **25**, 084016 (2012).

[110]V. V. Shchennikov **and** S. V. Ovsyannikov, 'Thermoelectric properties and phase transitions of ii–vi semiconductors at high pressure', phys. stat. sol. (b) **244**, 437 (2007).

[111]T. G. Ramesh **and** V. Shubha, 'Transport properties under pressure in hgse', J. Phys. C: Solid State Phys **15**, 6193 (1982).

[112]A. C. Smith, J. F. Janak **and** R. B. Adler, *Electronic conduction in solids*, techreport (McGraw-Hill, 1967).

[113]A. Raney, I. Maghami, Y. Feng, K. Mandli, S. Cohen **and** J. Goodall, 'An open-source python library for varying model parameters and automating concurrent simulations of the national water model', JAWRA Journal of the American Water Resources Association (2021).

[114]M. Lundstrom, *Fundamentals of carrier transport* (Cambridge university press, 2009).

[115]P. Giannozzi, S. Baroni, N. Bonini, M. Calandra, R. Car, C. Cavazzoni, D. Ceresoli, G. L. Chiarotti, M. Cococcioni **and** I. s. Dabo, 'Quantum espresso: a modular and open-source software project for quantum simulations of materials', Journal of physics: Condensed matter **21**, 395502 (2009).

[116]M. Zebarjadi, E. Rezaei, S. Akhanda **and** K. Esfarjani, 'Nernst coefficient within relaxation time approximation', Physical Review B **103**, 144404 (2021).

[117]S. Tang **and** M. S. Dresselhaus, 'Anisotropic transport for parabolic, non-parabolic, and linear bands of different dimensions', Applied Physics Letters **105**, 033907 (2014).

[118]A. Miura, H. Sepehri-Amin, K. Masuda, H. Tsuchiura, Y. Miura, R. Iguchi, Y. Sakuraba, J. Shiomi, K. Hono **and** K.-i. Uchida, 'Observation of anomalous ettingshausen effect and large transverse thermoelectric conductivity in permanent magnets', Applied Physics Letters **115**, 222403 (2019).

[119]A. v. Ettingshausen **and** W. Nernst, 'Ueber das auftreten electromotorischer kräfte in metallplatten, welche von einem wärmestrome durchflossen werden und sich im magnetischen felde befinden', Annalen der Physik **265**, 343–347 (1886).

[120]H. Mette, W. W. Gärtner **and** C. Loscoe, 'Nernst and ettingshausen effects in germanium between 300 and 750 k', Physical Review **115**, 537 (1959).

[121]K. Ikeda, H. Nakamura, I. Yanenaga **and** S. Yamaguchi, 'Transport coefficients of ge in magnetic fields', **in**Seventeenth international conference on thermoelectrics. proceedings ict98 (cat. no. 98th8365) (IEEE, 1998), **pages** 277–279.

[122]H. N. H. Nakamura, K. I. K. Ikeda **and** S. Y. S. Yamaguchi, 'Transport coefficients of indium antimonide in a magnetic field', Japanese journal of applied physics **38**, 5745 (1999).

[123]S. Bogason, 'Cryogenic cooling with a single crystal bismuth nernst-ettingshausen cooler', phdthesis (The Ohio State University, 2018).

[124]H. Goldsmid **and** K. Sydney, 'A thermal radiation detector employing the nernst effect in cd3as2-nias', Journal of Physics D: Applied Physics **4**, 869 (1971).

[125]M. Mizuguchi **and** S. Nakatsuji, 'Energy-harvesting materials based on the anomalous nernst effect', Science and technology of advanced materials **20**, 262–275 (2019).

[126]M. Cutler **and** N. F. Mott, 'Observation of anderson localization in an electron gas', Physical Review **181**, 1336 (1969).

[127]A. Avery, M. Pufall **and** B. L. Zink, 'Determining the planar nernst effect from magnetic-field-dependent thermopower and resistance in nickel and permalloy thin films', Physical Review B **86**, 184408 (2012).

[128]M. Matusiak, M. Babij **and** T. Wolf, 'Anisotropy of the seebeck and nernst coefficients in parent compounds of the iron-based superconductors', Physical Review B **97**, 100506 (2018).

[129]S. J. Watzman, T. M. McCormick, C. Shekhar, S.-C. Wu, Y. Sun, A. Prakash, C. Felser, N. Trivedi **and** J. P. Heremans, 'Dirac dispersion generates unusually large nernst effect in weyl semimetals', Physical Review B **97**, 161404 (2018).

[130]S. E. Rezaei, M. Zebarjadi **and** K. Esfarjani, 'Calculation of thermomagnetic properties using first-principles density functional theory', Computational Materials Science **210**, 111412 (2022).

[131]J. Noffsinger, F. Giustino, B. D. Malone, C.-H. Park, S. G. Louie **and** M. L. Cohen, 'Epw: a program for calculating the electron–phonon coupling using maximally localized wannier functions', Computer Physics Communications **181**, 2140–2148 (2010).

[132]P. Graziosi, C. Kumarasinghe **and** N. Neophytou, 'Impact of the scattering physics on the power factor of complex thermoelectric materials', Journal of Applied Physics **126**, 155701 (2019).

[133]P. Graziosi, Z. Li **and** N. Neophytou, 'Electra code: full-band electronic transport properties of materials', arXiv preprint arXiv:2208.00745 (2022).

[134]A. M. Ganose, J. Park, A. Faghaninia, R. Woods-Robinson, K. A. Persson **and** A. Jain, 'Efficient calculation of carrier scattering rates from first principles', Nature communications **12**, 1–9 (2021).

[135]G. Kresse **and** D. Joubert, 'From ultrasoft pseudopotentials to the projector augmented-wave method', Physical review b **59**, 1758 (1999).

[136]J. P. Perdew, K. Burke **and** Y. Wang, 'Generalized gradient approximation for the exchange-correlation hole of a many-electron system', Physical review B **54**, 16533 (1996).

[137]A. Matthiessen, 'Xx. on the electric conducting power of the metals', Philosophical transactions of the royal society of London, 383–387 (1858).

[138]M. V. Fischetti **and** S. E. Laux, 'Band structure, deformation potentials, and carrier mobility in strained si, ge, and sige alloys', Journal of Applied Physics **80**, 2234–2252 (1996).

[139]A. Arnaud **and** G. Quentin, 'Measurement of the piezoelectric constant of insb by electromechanical resonance', Physics Letters A **32**, 16–17 (1970).

[140]T. Soma, 'The electronic theory of iii-v and ii-vi tetrahedral compounds. i. crystal energy and bulk modulus', Journal of Physics C: Solid State Physics **11**, 2669 (1978).

[141]S. Baroni **and** R. Resta, 'Ab initio calculation of the macroscopic dielectric constant in silicon', Physical Review B **33**, 7017 (1986).

[142]S. Adachi, 'Model dielectric constants of si and ge', Physical Review B **38**, 12966 (1988).

[143]R. K. Ram **and** S. S. Kushwaha, 'Phonon dispersion relations for gaas and insb', Journal of the Physical Society of Japan **54**, 617–624 (1985).

[144]O. Restrepo, K. Varga **and** S. Pantelides, 'First-principles calculations of electron mobilities in silicon: phonon and coulomb scattering', Applied Physics Letters **94**, 212103 (2009).

[145]O. Golikova, B. Y. Moizhes **and** L. Stilbans, 'Hole mobility of germanium as a function of concentration and temperature', Soviet Physics-Solid State **3**, 2259–2265 (1962).

[146]T. C. Gomez, 'Investigation of electrical and optical properties of bulk iii-v ternary semiconductors', (2009).

[147]M. Weiler, 'Semiconductors and semimetals', Academic Press, New York, 1981) vol **16**, 119 (1981).

[148]R. Lieten, J. McCallum **and** B. Johnson, 'Single crystalline sige layers on si by solid phase epitaxy', Journal of Crystal Growth **416**, 34–40 (2015).

[149]C. Jacoboni, C. Canali, G. Ottaviani **and** A. A. Quaranta, 'A review of some charge transport properties of silicon', Solid-State Electronics **20**, 77–89 (1977).

[150]V. Aubry-Fortuna **and** P. Dollfus, 'Electron transport properties in high-purity ge down to cryogenic temperatures', Journal of Applied Physics **108**, 123706 (2010).

[151]H. Mette, W. W. Gärtner **and** C. Loscoe, 'Nernst and ettingshausen effects in silicon between 300° k and 800° k', Physical Review **117**, 1491 (1960).

[152]T. Ashley, A. Dean, C. T. Elliott, R. Jefferies, F. Khaleque **and** T. Phillips, 'High-speed, low-power insb transistors', **in**International electron devices meeting. iedm technical digest (IEEE, 1997), **pages** 751–754.

[153]J. L. Pipher, W. J. Forrest, W. J. Glaccum, R. G. Benson, D. J. Krebs, M. D. Jhabvala, J. P. Rosbeck, N. A. Lum, W. Lum **and** J. D. s. Garnett, 'Insb arrays for irac (infrared array camera) on sirtf (space infrared telescope facility)', **in**Infrared spaceborne remote sensing viii **volume** 4131 (SPIE, 2000), **pages** 7–12.

[154]I. Shibasaki, 'Properties of insb thin films grown by molecular beam epitaxy and their applications to magnetic field sensors', IEEJ Transactions on Sensors and Micromachines **123**, 69–78 (2003).

[155]M. El-Saden **and** F. Thomas, 'Nernst effect in indium antimonide', Journal of Applied Physics **36**, 181–183 (1965).

[156]O. Lindberg, 'Hall effect', Proceedings of the IRE **40**, 1414–1419 (1952).

[157]H. Nakamura, K. Ikeda **and** S. Yamaguchi, 'Physical model of nernst element', **in**Seventeenth international conference on thermoelectrics. proceedings ict98 (cat. no. 98th8365) (IEEE, 1998), **pages** 97–100.

[158]K. Behnia, M.-A. Méasson **and** Y. Kopelevich, 'Oscillating nernst-ettingshausen effect in bismuth across the quantum limit', Physical review letters **98**, 166602 (2007).

[159]A. Abrikosov, 'Quantum linear magnetoresistance; solution of an old mystery', Journal of Physics A: Mathematical and General **36**, 9119 (2003).

[160]A. Pippard **and** R. Chambers, 'The mean free path of conduction electrons in bismuth', Proceedings of the Physical Society. Section A **65**, 955 (1952).

[161]I. Y. Korenblit, M. Kuznetsov **and** S. Shalyt, 'Thermal emf and thermomagnetic properties of bismuth at low temperatures', Sov Phys JETP **29**, 4–10 (1969).

[162]T. Arisaka, M. Otsuka **and** Y. Hasegawa, 'Investigation of carrier scattering process in polycrystalline bulk bismuth at 300 k', Journal of Applied Physics **123**, 235107 (2018).

[163]T. Arisaka, M. Otsuka, M. Tokitani **and** Y. Hasegawa, 'Temperature dependence of carrier scattering in polycrystalline bismuth', Journal of Applied Physics **126**, 085101 (2019).

[164]C. Jacoboni, **editor**, *Theory of electron transport in semiconductors: a pathway from elementary physics to nonequilibrium green functions* (Springer Science & Business Media, New York, 2010).

[165]F. Caglieris, C. Wuttke, S. Sykora, V. Süss, C. Shekhar, C. Felser, B. Büchner **and** C. Hess, 'Anomalous nernst effect and field-induced lifshitz transition in the weyl semimetals tap and taas', Physical Review B **98**, 201107 (2018).

[166]C. Fu, S. N. Guin, S. J. Watzman, G. Li, E. Liu, N. Kumar, V. Süβ, W. Schnelle, G. Auffermann **and** C. s. Shekhar, 'Large nernst power factor over a broad temperature range in polycrystalline weyl semimetal nbp', Energy & Environmental Science **11**, 2813–2820 (2018).

[167]F. Han, N. Andrejevic, T. Nguyen, V. Kozii, Q. T. Nguyen, T. Hogan, Z. Ding, R. Pablo-Pedro, S. Parjan **and** B. s. Skinner, 'Quantized thermoelectric hall effect induces giant power factor in a topological semimetal', Nature communications **11**, 1–7 (2020).

[168]K. Behnia, 'The nernst effect and the boundaries of the fermi liquid picture', Journal of Physics: Condensed Matter **21**, 113101 (2009).

[169]Y. Sakuraba, K. Hasegawa, M. Mizuguchi, T. Kubota, S. Mizukami, T. Miyazaki **and** K. Takanashi, 'Anomalous nernst effect in l10-fept/mnga thermopiles for new thermoelectric applications', Applied physics express **6**, 033003 (2013).

[170]Y. Sakuraba, 'Potential of thermoelectric power generation using anomalous nernst effect in magnetic materials', Scripta Materialia **111**, 29–32 (2016).

[171]J. Li, Y. Zhao, H. S. Tan, Y. Guo, C.-A. Di, G. Yu, Y. Liu, M. Lin, S. H. Lim **and** Y. s. Zhou, 'A stable solution-processed polymer semiconductor with record high-mobility for printed transistors', Scientific reports **2**, 1–9 (2012).

[172]M. Chhowalla, D. Jena **and** H. Zhang, 'Two-dimensional semiconductors for transistors', Nature Reviews Materials **1**, 1–15 (2016).

[173]B. R. Sutherland **and** E. H. Sargent, 'Perovskite photonic sources', Nature Photonics **10**, 295–302 (2016).

[174]F. Bonaccorso, Z. Sun, T. Hasan **and** A. Ferrari, 'Graphene photonics and optoelectronics', Nature photonics **4**, 611–622 (2010).

[175]Y. Gu, Y. Katsura, T. Yoshino, H. Takagi **and** K. Taniguchi, 'Rechargeable magnesium-ion battery based on a tise2-cathode with dp orbital hybridized electronic structure', Scientific reports **5**, 1–9 (2015).

[176]C. K. Chan, H. Peng, G. Liu, K. McIlwrath, X. F. Zhang, R. A. Huggins **and** Y. Cui, 'High-performance lithium battery anodes using silicon nanowires', Nature nanotechnology **3**, 31–35 (2008).

[177]Y. Orikasa, Y. Gogyo, H. Yamashige, M. Katayama, K. Chen, T. Mori, K. Yamamoto, T. Masese, Y. Inada **and** T. s. Ohta, 'Ionic conduction in lithium ion battery composite electrode governs cross-sectional reaction distribution', Scientific reports **6**, 1–6 (2016).

[178]M. Ibánez, Z. Luo, A. Genc, L. Piveteau, S. Ortega, D. Cadavid, O. Dobrozhan, Y. Liu, M. Nachtegaal **and** M. s. Zebarjadi, 'High-performance thermoelectric nanocomposites from nanocrystal building blocks', Nature communications **7**, 1–7 (2016).

[179]M. Zebarjadi, K. Esfarjani, M. Dresselhaus, Z. Ren **and** G. Chen, 'Perspectives on thermoelectrics: from fundamentals to device applications', Energy & Environmental Science **5**, 5147–5162 (2012).

[180]P. Graziosi, C. Kumarasinghe **and** N. Neophytou, 'Material descriptors for the discovery of efficient thermoelectrics', ACS Applied Energy Materials **3**, 5913–5926 (2020).

[181]A. Aspuru-Guzik **and** P. Walther, 'Photonic quantum simulators', Nature physics **8**, 285–291 (2012).

[182]Y. Zhang, Y.-W. Tan, H. L. Stormer **and** P. Kim, 'Experimental observation of the quantum hall effect and berry's phase in graphene', nature **438**, 201–204 (2005).

[183]M. Buscema, D. J. Groenendijk, G. A. Steele, H. S. Van Der Zant **and** A. Castellanos-Gomez, 'Photovoltaic effect in few-layer black phosphorus pn junctions defined by local electrostatic gating', Nature communications **5**, 1–6 (2014).

[184]S. Goossens, G. Navickaite, C. Monasterio, S. Gupta, J. J. Piqueras, R. Pérez, G. Burwell, I. Nikitskiy, T. Lasanta **and** T. s. Galán, 'Broadband image sensor array based on graphene–cmos integration', Nature Photonics **11**, 366–371 (2017).

[185]S. Lee, A. Reuveny, J. Reeder, S. Lee, H. Jin, Q. Liu, T. Yokota, T. Sekitani, T. Isoyama **and** Y. s. Abe, 'A transparent bending-insensitive pressure sensor', Nature nanotechnology **11**, 472–478 (2016).

[186]F. Patolsky, G. Zheng **and** C. M. Lieber, 'Fabrication of silicon nanowire devices for ultrasensitive, label-free, real-time detection of biological and chemical species', Nature protocols **1**, 1711–1724 (2006).

[187]A. D. Chowdhury, K. Takemura, T.-C. Li, T. Suzuki **and** E. Y. Park, 'Electrical pulse-induced electrochemical biosensor for hepatitis e virus detection', Nature communications **10**, 1–12 (2019).

[188]J. M. Ziman, *Electrons and phonons: the theory of transport phenomena in solids* (Oxford university press, 2001).

[189]M. Markov, S. Rezaei, S. N. Sadeghi, K. Esfarjani **and** M. Zebarjadi, 'Thermoelectric properties of semimetals', Phys. Rev. M **3**, 095401 (2019).

[190]S. E. Rezaei, M. Zebarjadi **and** K. Esfarjani, 'Effect of exchange-correlation functional type and spin-orbit coupling on thermoelectric properties of zrte2', Journal of Solid State Chemistry **302**, 122414 (2021).

[191]W. Van Roosbroeck, 'Theory of the flow of electrons and holes in germanium semiconductors', The Bell System Technical Journal **29**, 560–607 (1950).

[192]J. Bardeen **and** W. Shockley, 'Deformation potentials and mobilities in non-polar crystals', Physical review **80**, 72 (1950).

[193]D. Vasileska, S. M. Goodnick **and** G. Klimeck, *Computational electronics: semiclassical and quantum device modeling and simulation* (CRC press, 2017).

[194]A. Minnich, H. Lee, X. Wang, G. Joshi, M. Dresselhaus, Z. Ren, G. Chen **and** D. Vashaee, 'Modeling study of thermoelectric sige nanocomposites', Physical Review B **80**, 155327 (2009).

[195]K. Hippalgaonkar, Y. Wang, Y. Ye, D. Y. Qiu, H. Zhu, Y. Wang, J. Moore, S. G. Louie **and** X. Zhang, 'High thermoelectric power factor in two-dimensional crystals of mo s 2', Physical Review B **95**, 115407 (2017).

[196]A. F. May, E. S. Toberer, A. Saramat **and** G. J. Snyder, 'Characterization and analysis of thermoelectric transport in n-type ba 8 ga 16- x ge 30+ x', Physical Review B **80**, 125205 (2009).

[197]H. Xie, H. Wang, Y. Pei, C. Fu, X. Liu, G. J. Snyder, X. Zhao **and** T. Zhu, 'Beneficial contribution of alloy disorder to electron and phonon transport in half-heusler thermoelectric materials', Advanced Functional Materials **23**, 5123–5130 (2013).

[198]G. Samsonidze **and** B. Kozinsky, 'Accelerated screening of thermoelectric materials by first-principles computations of electron–phonon scattering', Advanced Energy Materials **8**, 1800246 (2018).

[199]J.-J. Zhou, J. Park, I.-T. Lu, I. Maliyov, X. Tong **and** M. Bernardi, 'Perturbo: a software package for ab initio electron–phonon interactions, charge transport and ultrafast dynamics', Computer Physics Communications **264**, 107970 (2021).

[200]B. K. Ridley, *Quantum processes in semiconductors* (Oxford university press, 2013).

[201]D. K. Ferry, *Semiconductors* (IoP Publishing, 2019).

[202]H. B. Callen, 'Electric breakdown in ionic crystals', Physical Review **76**, 1394 (1949).

[203]H. Ehrenreich, 'Electron scattering in insb', Journal of Physics and Chemistry of Solids **2**, 131–149 (1957).

[204]H. Brooks, 'Scattering by ionized impurities in semiconductors', **in**Physical review **volume** 83, 4 (AMERICAN PHYSICAL SOC ONE PHYSICS ELLIPSE, COLLEGE PK, MD 20740-3844 USA, 1951), **pages** 879–879.

[205]B.-C. Lye, P. Houston, H.-K. Yow **and** C. Button, 'Gainp/algaas/gainp double heterojunction bipolar transistors with zero conduction band spike at the collector', IEEE Transactions on Electron Devices **45**, 2417–2421 (1998).

[206]M. Hanna, A. Majerfeld **and** D. Szmyd, 'Strain relaxation and compensation due to annealing in heavily carbon-doped gaas', Applied physics letters **59**, 2001–2003 (1991).

[207]M. Wenzel, G. Irmer, J. Monecke **and** W. Siegel, 'Determination of the effective hall factor in p-type semiconductors', Semiconductor science and technology **13**, 505 (1998).

[208]P. Enquist, 'P-type doping limit of carbon in organometallic vapor phase epitaxial growth of gaas using carbon tetrachloride', Applied physics letters **57**, 2348–2350 (1990).

[209]M. K. Hudait, P. Modak, S. Hardikar **and** S. Krupanidhi, 'Zn incorporation and band gap shrinkage in p-type gaas', Journal of applied physics **82**, 4931–4937 (1997).

[210]J. Ma, A. S. Nissimagoudar **and** W. Li, 'First-principles study of electron and hole mobilities of si and gaas', Physical Review B **97**, 045201 (2018).

[211]T.-H. Liu, J. Zhou, B. Liao, D. J. Singh **and** G. Chen, 'First-principles mode-by-mode analysis for electron-phonon scattering channels and mean free path spectra in gaas', Physical Review B **95**, 075206 (2017).

[212]M. Bernardi, D. Vigil-Fowler, C. S. Ong, J. B. Neaton **and** S. G. Louie, 'Ab initio study of hot electrons in gaas', Proceedings of the National Academy of Sciences **112**, 5291–5296 (2015).

[213]C. Wolfe, G. Stillman **and** J. Dimmock, 'Ionized impurity density in n-type gaas', Journal of Applied Physics **41**, 504–507 (1970).

[214]S. Majdi, V. Djurberg, N. Suntornwipat, M. Gabrysch **and** J. Isberg, 'Carrier scattering mechanisms: identification via the scaling properties of the boltzmann transport equation', Advanced Theory and Simulations **4**, 2000103 (2021).

[215]D. Rode **and** S. Knight, 'Electron transport in gaas', Physical Review B **3**, 2534 (1971).

[216]A. Jayaraj, I. Siloi, M. Fornari **and** M. B. Nardelli, 'Relaxation time approximations in paoflow 2.0', Scientific reports **12**, 1–12 (2022).

[217]J. Blakemore, 'Semiconducting major properties of gallium arsenide', Journal of Applied Physics **53**, R123–R181 (1982).

[218]M. Razeghi, *The mocvd challenge: volume 2: a survey of gainasp-gaas for photonic and electronic device applications* (CRC Press, 1995).

[219]M. Sotoodeh, A. Khalid **and** A. Rezazadeh, 'Empirical low-field mobility model for iii–v compounds applicable in device simulation codes', Journal of applied physics **87**, 2890–2900 (2000).

[220]V. Chin, T. Tansley **and** T. Osotchan, 'Electron mobilities in gallium, indium, and aluminum nitrides', Journal of Applied Physics **75**, 7365–7372 (1994).

[221]M. Ilegems **and** H. Montgomery, 'Electrical properties of n-type vapor-grown gallium nitride', Journal of Physics and Chemistry of Solids **34**, 885–895 (1973).

[222]M. Ilegems **and** H. Montgomery, 'Electrical properties of n-type vapor-grown gallium nitride', Journal of Physics and Chemistry of Solids **34**, 885–895 (1973).

[223]T. T. Mnatsakanov, M. E. Levinshtein, L. I. Pomortseva, S. N. Yurkov, G. S. Simin **and** M. A. Khan, 'Carrier mobility model for gan', Solid-State Electronics **47**, 111–115 (2003).

[224]V. Galavanov **and** N. Siukaev, 'On mechanism of electron scattering in inp', physica status solidi (b) **38**, 523–530 (1970).

[225]Y. Takeda **and** A. Sasaki, 'Re-assessment of electron mobility and conduction-band deformation potential in indium phosphide', Solid-state electronics **27**, 1127–1129 (1984).

[226]M. Bhatnagar **and** B. J. Baliga, 'Comparison of 6h-sic, 3c-sic, and si for power devices', IEEE Transactions on electron devices **40**, 645–655 (1993).

[227]J. Wozny, A. Kovalchuk, Z. Lisik, J. Podgorski, P. Bugalski, A. Kubiak **and** Ł. Ruta, 'Monte carlo simulations of electron transport in 4h-sic using the dft-calculated density of states', Journal of Computational Electronics **20**, 791–797 (2021).

[228]F. Meng, J. Ma, J. He **and** W. Li, 'Phonon-limited carrier mobility and temperature-dependent scattering mechanism of 3 c-sic from first principles', Physical Review B **99**, 045201 (2019).

[229]S. N. Guin, K. Manna, J. Noky, S. J. Watzman, C. Fu, N. Kumar, W. Schnelle, C. Shekhar, Y. Sun **and** J. s. Gooth, 'Anomalous nernst effect beyond the magnetization scaling relation in the ferromagnetic heusler compound co2mnga', NPG Asia Materials **11**, 1–9 (2019).

[230]O. Entin-Wohlman, Y. Imry **and** A. Aharony, 'Three-terminal thermoelectric transport through a molecular junction', Physical Review B **82**, 115314 (2010).

[231]Y. Pu, D. Chiba, F. Matsukura, H. Ohno **and** J. Shi, 'Mott relation for anomalous hall and nernst effects in ga 1- x mn x as ferromagnetic semiconductors', Physical review letters **101**, 117208 (2008).

[232]D. Vanderbilt, *Berry phases in electronic structure theory: electric polarization, orbital magnetization and topological insulators* (Cambridge University Press, 2018).

[233]D. Xiao, Y. Yao, Z. Fang **and** Q. Niu, 'Berry-phase effect in anomalous thermoelectric transport', Physical review letters **97**, 026603 (2006).

[234]I. Samathrakis **and** H. Zhang, 'Tailoring the anomalous hall effect in the noncollinear antiperovskite mn 3 gan', Physical Review B **101**, 214423 (2020).

[235]G. Guo, Q. Niu **and** N. Nagaosa, 'Anomalous nernst and hall effects in magnetized platinum and palladium', Physical Review B **89**, 214406 (2014).

[236]Y. Kozuka, S. Isogami, K. Masuda, Y. Miura, S. Das, J. Fujioka, T. Ohkubo **and** S. Kasai, 'Observation of nonlinear spin-charge conversion in the thin film of nominally centrosymmetric dirac semimetal sriro 3 at room temperature', Physical Review Letters **126**, 236801 (2021).

[237]H. Zhang, H. Feng, X. Xu, W. Hao **and** Y. Du, 'Recent progress on 2d kagome magnets: binary tmsnn (t= fe, co, mn)', Advanced Quantum Technologies **4**, 2100073 (2021).

[238]A. Sakai, S. Minami, T. Koretsune, T. Chen, T. Higo, Y. Wang, T. Nomoto, M. Hirayama, S. Miwa **and** D. s. Nishio-Hamane, 'Iron-based binary ferromagnets for transverse thermoelectric conversion', Nature **581**, 53–57 (2020).

[239]A. Sakai, Y. P. Mizuta, A. A. Nugroho, R. Sihombing, T. Koretsune, M.-T. Suzuki, N. Takemori, R. Ishii, D. Nishio-Hamane **and** R. s. Arita, 'Giant anomalous nernst effect and quantum-critical scaling in a ferromagnetic semimetal', Nature Physics **14**, 1119–1124 (2018).

[240]Y. Li, J. Li, M. Ye, F. Zheng, Z. Zhang, J. Fu, W. Duan **and** Y. Xu, 'High-temperature quantum anomalous hall insulators in lithium-decorated iron-based superconductor materials', Physical Review Letters **125**, 086401 (2020).

[241]M. Kang, L. Ye, S. Fang, J.-S. You, A. Levitan, M. Han, J. I. Facio, C. Jozwiak, A. Bostwick **and** E. s. Rotenberg, 'Dirac fermions and flat bands in the ideal kagome metal fesn', Nature materials **19**, 163–169 (2020).

[242]M. P. Marder, *Condensed matter physics* (John Wiley & Sons, 2010).

[243]G. Baym **and** C. Pethick, 'Landau fermi-liquid theory: concepts and applications', (2008).

[244]M. S. Suzuki, 'Fermi liquid theory masatsugu sei suzuki department of physics, suny at binghamton (date: january 13, 2019)', (2019).

[245]V. V. Kabanov **and** A. Alexandrov, 'Electron relaxation in metals: theory and exact analytical solutions', Physical Review B **78**, 174514 (2008).

[246]G. Eliashberg, 'Interactions between electrons and lattice vibrations in a superconductor', Sov. Phys. JETP **11**, 696–702 (1960).

[247]G. Eliashberg, 'Temperature green's function for electrons in a superconductor', Sov. Phys. JETP **12**, 1000–1002 (1961).

[248]J. Hubbard, 'Electron correlations in narrow energy bands', Proceedings of the Royal Society of London. Series A. Mathematical and Physical Sciences **276**, 238–257 (1963).

[249]M. Cococcioni, 'The lda+ u approach: a simple hubbard correction for correlated ground states', Correlated Electrons: From Models to Materials Modeling and Simulation **2** (2012).

[250]W. Xie, W. Xiong, C. A. Marianetti **and** D. s. Morgan, 'Correlation and relativistic effects in u metal and u-zr alloy: validation of ab initio approaches', Physical Review B **88**, 235128 (2013).

[251]M. Cococcioni **and** S. De Gironcoli, 'Linear response approach to the calculation of the effective interaction parameters in the lda+ u method', Physical Review B **71**, 035105 (2005).

[252]T. Chen, S. Minami, A. Sakai, Y. Wang, Z. Feng, T. Nomoto, M. Hirayama, R. Ishii, T. Koretsune **and** R. s. Arita, 'Large anomalous nernst effect and nodal plane in an iron-based kagome ferromagnet', Science advances **8**, eabk1480 (2022).

[253]B. C. Sales, B. Saparov, M. A. McGuire, D. J. Singh **and** D. S. Parker, 'Ferromagnetism of fe3sn and alloys', Scientific reports **4**, 1–6 (2014).

[254]K. L. Krewer, W. Zhang, J. Arabski, G. Schmerber, E. Beaurepaire, M. Bonn **and** D. Turchinovich, 'Thickness-dependent electron momentum relaxation times in iron films', Applied Physics Letters **116**, 102406 (2020).

[255]T. Chen, S. Minami, A. Sakai, Y. Wang, Z. Feng, T. Nomoto, M. Hirayama, R. Ishii, T. Koretsune **and** R. s. Arita, 'Large anomalous nernst effect and nodal plane in an iron-based kagome ferromagnet', Science advances **8**, eabk1480 (2022).

[256]X. Wang, J. R. Yates, I. Souza **and** D. Vanderbilt, 'Ab initio calculation of the anomalous hall conductivity by wannier interpolation', Physical Review B **74**, 195118 (2006).

[257]Y. Yao, L. Kleinman, A. MacDonald, J. Sinova, T. Jungwirth, D.-s. Wang, E. Wang **and** Q. Niu, 'First principles calculation of anomalous hall conductivity in ferromagnetic bcc fe', Physical review letters **92**, 037204 (2004).